PHYSICS BULLETIN

2025

...SHARING SCIENCE WITH SOCIETY

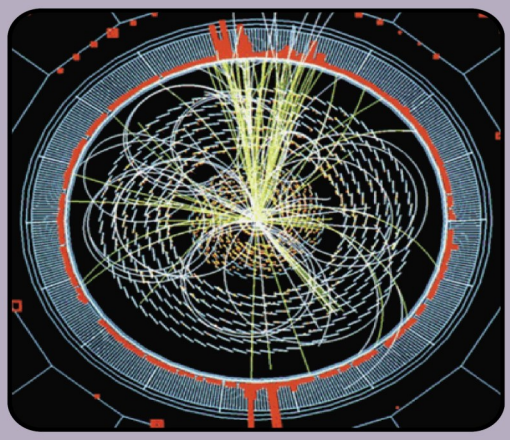

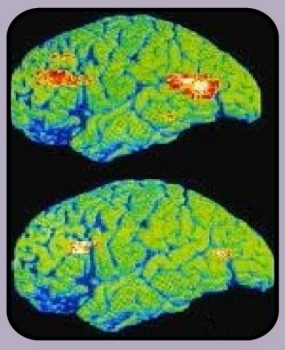

Department of Physics
Aligarh Muslim University

Department of Physics

Estd. 1912

Ortho Mosaic Aerial Image of the Department of Physics

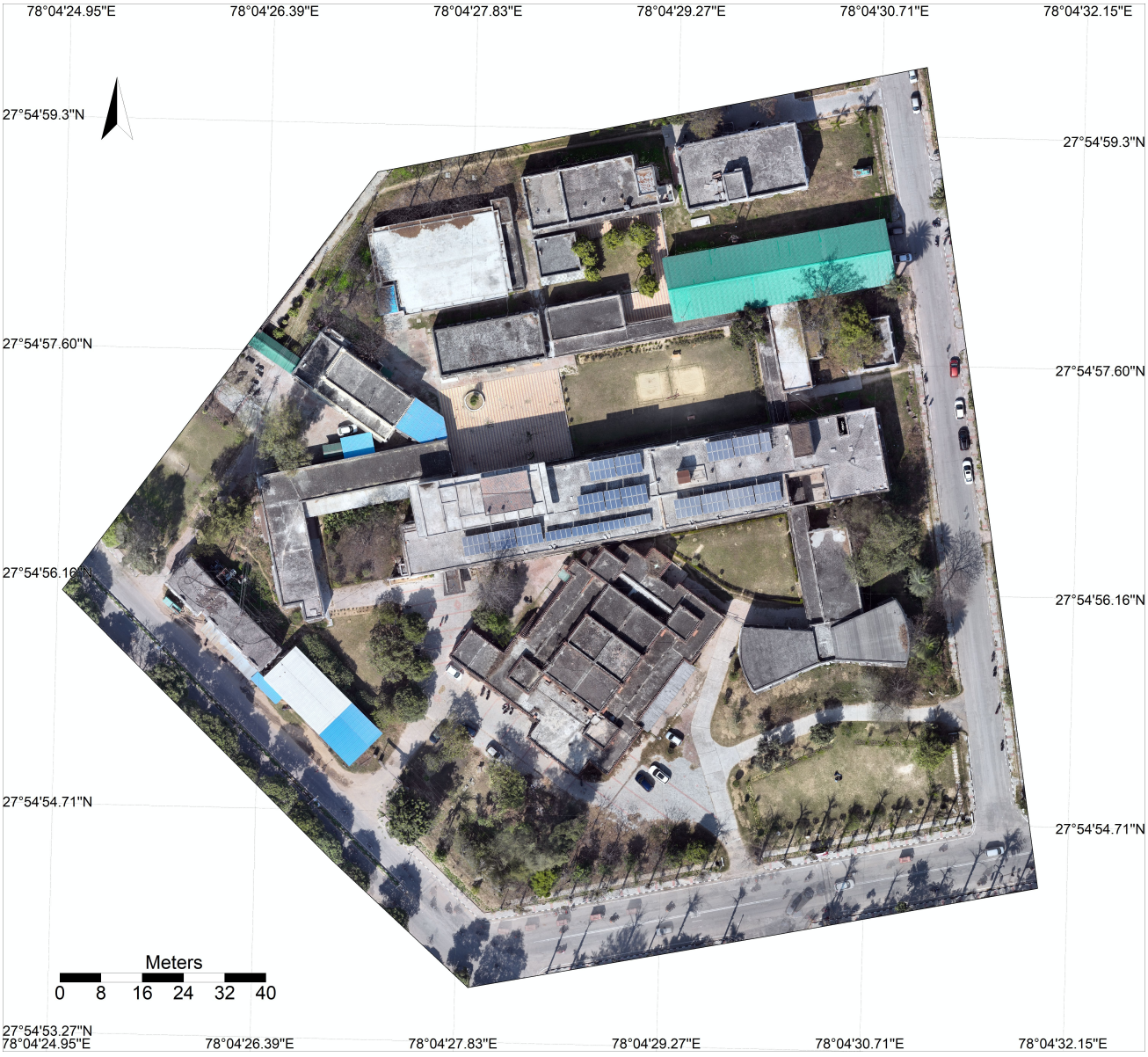

Courtesy of the Interdisciplinary Department of Remote Sensing and GIS Applications

ALIGARH MUSLIM UNIVERSITY

Aligarh - 202 002, UP., India.

A Central University (NAAC ACCREDITED "A+" GRADE)

PROF. NAIMA KHATOON

M.Phil, Ph.D. (Psychology)

Vice-Chancellor

Phone: (Off) +91-571-2700994/2702167
(Res) +91-571-2700443
Fax: (Off) +91-571-2702607
Email: vcamu@amu.ac.in

28th January 2025

Message

I am happy to learn that the Department of Physics at Aligarh Muslim University is publishing the annual "Physics Bulletin" volume, a significant initiative for over two decades. This resonates deeply with Sir Syed's ideals. It is a dynamic platform where students, scholars, and faculty engage in discussions and share insights that enrich scientific discourse. By encouraging curiosity and collaboration, the bulletin embodies the spirit of inquiry Sir Syed envisioned as the cornerstone of modern education.

The Department of Physics is significant in advancing scientific knowledge and education at AMU. Founded on the visionary ideals of Sir Syed Ahmad Khan, who promoted the blend of modern scientific inquiry with traditional educational frameworks, the department exemplifies his profound foresight and steadfast commitment to intellectual development.

Established in 1912, the Department of Physics has played a crucial role in upholding Sir Syed's vision of creating a culture of critical thinking and scientific inquiry. Through its extensive research in areas such as condensed matter physics, materials science, spectroscopy, and theoretical physics, the department has not only contributed to the global scientific community but has also empowered generations of students to think creatively and address contemporary challenges.

On National Science Day 2025, I appreciate the department's sustained dedication to nurturing a scientific temperament and contributing to the university's rich academic heritage. I urge young scientists to imagine and innovate more rigorously to take the University's research output to greater heights. Your efforts continue to bring Sir Syed's vision to life, ensuring that AMU remains a beacon of progress and innovation.

With best wishes,

Naima Khatoon

Prof. Naima Khatoon

DEAN

FACULTY OF SCIENCE
Aligarh Muslim University
Aligarh - 202002 (INDIA)
Tel:(Ext.) 0571-2700920 (Int.) 3631, 3632
Email: deanfacultyofscience@gmail.com

विज्ञान संकाय
ए.एम.यू. अलीगढ़
سائنس فیکلٹی
علی گڑھ مسلم یونیورسٹی علی گڑھ

"MESSAGE"

I extend my warm congratulations to the Department of Physics on the publication of the latest issue of the Physics Bulletin." The Department of Physics has consistently been a vibrant and dynamic hub for academic and research excellence. Its initiatives, like the "Physics Bulletin," reflect a progressive academic spirit. Such publications encourage students, research scholars, and faculty members to explore, innovate, and contribute valuable insights into the field of physics.

The regular publication of the Physics Bulletin is testament to the department's unwavering commitment to fostering scientific temper and cultivating a deeper appreciation for the concepts of physics.

I congratulate the contributors and the department for upholding the legacy of Aligarh Muslim University in promoting excellence. I am confident that this publication will continue to inspire curiosity and enrich the knowledge of its readers.

Best wishes for continued success.

(Prof. Sartaj Tabassum)
Dean,
Faculty of Science, AMU

Prof. Anisul Ain Usmani
Chairman

Department of Physics
Aligarh Muslim University
Aligarh - 202002, U.P., India
+91-9412275671
anisul.usmani@gmail.com

January 30, 2025

As our National Science Day 2025 on February 28 approaches, there is a flurry of activities and great excitement in the Department of Physics. Commemorative events are being planned, lectures are being organised, night sky watching of Planet Parade-2025 and other public outreach programmes are underway. The Department is bustling with scientific activities. The newly created *Heritage Science Museum* in the Department has become a cynosure of all eyes. It does not only preserve laboratory equipment of historical significance for posterity but traces a timeline through the Department's history. To top it all, The Physics Bulletin-2025 —an academic accomplishment— is a real feather in our cap.

The erudite article by our revered teacher and former Chairman, Professor R. Prasad, on *Positron Emission Tomography* is of essence in cancer diagnosis. Besides being rich in information, it illuminates the issues at stake. The thought-provoking essay of Professor Afsar Abbas on *Two Independent Geometries and Two Independent Quantum Mechanics* calls forth an effulgent blaze of original and diverse ideas. These articles will have an indelible impression on all of us. The legacy of Professor Harnam Singh Hans is well recorded by Professor B. P. Singh, in his elaborate and interesting article. Professor Hans built a Cockcroft-Walton Neutron Generator in our department in 1958 by dint of his hard work, tenacity and support of Professor Piara Singh Gill, Dr. D. C. Sarkar and Dr. C. S. Khurana. The accelerator was first of its kind in any Indian University. Professor Zafar Ali Khan interestingly elucidates the life and legacy of Professor Israr Ahmad. Leading a life of great simplicity, Professor Ahmad was a man of many distinctions. The theory group flourished and excelled under his able leadership. It seems we can't hold a candle to our great teachers though we are doing our bit. We value deep respect for their lasting legacy and immense contributions. It is our duty to add to that legacy, not just live off it.

I am lost in admiration of fresh and scholarly essays on variety of miscellaneous topics of modern Physics written by my students in rigorous detail. I am grateful to my colleagues, alumni and my teachers for their profoundly insightful contributions, which reflect their ability and dedication to their research and teaching. They have always been playing a pivotal role in intellectual development as well as in fostering scientific enquiry in young minds.

I am indebted to the editors and reviewers, who pulled out all the stops in completing the Bulletin with diligence, insight, and meticulous preparation. Besides being carefully edited, it is attractively presented. I am thankful to Mr. Maaz Moonis for the beautiful artwork and skilful typesetting.

My heartfelt appreciation is due to the Interdisciplinary Department of Remote Sensing and GIS Applications for conducting high performance drone-based aerial survey and

providing a high-resolution Ortho-Mosaic imagery of the Department of Physics on a complementary basis. Their team's proficiency in employing the DJI Movic 3E photogrammetric system and Pix4D software has resulted in an outstanding dataset that will significantly aid infrastructure planning in our department.

This erudite Physics Bulletin deserves a wide reading.

With best wishes,

Prof. Anisul Ain Usmani

(Left to Right) ***Prof. Naima Khatoon*** *(Vice Chancellor, Aligarh Muslim University),* ***Prof. Sartaj Tabassum*** *(Dean, F/o Science, Aligarh Muslim University) and* ***Prof. Anisul Ain Usmani*** *(Chairman, D/o Physics, Aligarh Muslim University)*

Editors' Note

The *Physics Bulletin 2025* presents a diverse collection of articles showcasing groundbreaking research, innovative technologies, and the transformative impact of physics on science and society. This issue celebrates both the past and future of physics, honoring the contributions of pioneers within our academic community and the global scientific landscape, while presenting the latest advancements across various disciplines.

We have categorized the articles into distinct themes, including Physics Nobel Prize (2024) & Theoretical Physics Advancements, Particle Physics and Cosmology, Applied Nuclear Physics & Imaging Techniques, Material Science & Emerging Technologies, Liquid Crystals & Machine Learning, and Legacy and Historical Perspectives. While other thematic groupings are also possible, we believe this arrangement best captures the scope and diversity of the content.

The issue begins with groundbreaking **Physics Nobel Prize (2024) & Theoretical Physics Advancement**. Abdul Quadir and Haider Hasan Jafri explore the remarkable journey of the 2024 Nobel Laureates in Physics, John J. Hopfield and Geoffrey E. Hinton, who bridged physics and artificial intelligence. Next, Syed Afsar Abbas presents pioneering work that proposes a paradigm uniting physics and biology, addressing fundamental mysteries like dark energy and quantum nonlocality. *The editors adopt a neutral stance, encouraging readers to engage with the author's perspective and draw their own conclusions.*

Particle Physics and Cosmology follow, featuring thought-provoking discussions on supersymmetry, the fate of the universe, and the monumental scientific achievements from LEP to the LHC, and finally to The Alpha Magnetic Spectrometer. Sudhir Kumar Gupta and Surabhi Gupta highlight the cutting-edge research on supersymmetry, Najimuddin Khan, in *"Will the Universe End? A Particle Physics Perspective"* discusses the Universe's stability based on the Standard Model (SM) and Higgs potential, Mohsin Khan pens the discoveries made possible by the LHC and Meeran Zuberi writes on AMS-02. The final article in this section "Exploring Unusual Measurements of Neutron Stars: HESS J1731-347, XTE J1814-338, and Beyond" by Ishfaq Ahmad Rather and Anisul Ain Usmani focus on extreme astrophysical objects and their implications for dense matter physics aligns closely with the section's exploration of fundamental physics and cosmic mysteries. These articles offer insights into the monumental efforts and discoveries that continue to reshape our understanding of the cosmos.

In **Applied Nuclear Physics and Imaging Techniques**, we explore advancements in nuclear imaging, such as positron emission tomography (PET), as well as the vital work done in radiation exposure assessment. Articles here connect fundamental physics with real-world applications, particularly in medical and environmental health. R. Prasad elucidates the significance of positron emission tomography (PET) in cancer diagnosis, while B. P. Singh and R. Prasad examine the health implications of natural radiation exposure.

Material Science and Emerging Technologies showcases the intersection of fundamental science and emerging technological fields. In the article "Notes on Fundamentals of Lasers, Mubashshara Fatma and Haris Kunari, endeavor to illuminate the foundational principles and intricate processes underpinning the fascinating realm of lasers. Mohammad Adnan highlights the significant strides in inorganic-organic hybrid perovskites, Adiba and Tufail Ahmad talk about green energy solutions like hydrogen as a sustainable energy source, and Lalit Bhardwaj traces Trace Element Analysis, exemplify physics' transformative potential in addressing societal challenges and its potential to transform industries.

The **Liquid Crystals and Machine Learning** section connects cutting-edge research in liquid crystal technologies with the future of machine learning, while also featuring an article on software tools for tensor operations - a nod to the growing importance of computational physics in research and application. Shubham Gupta, Arbaz Khan, and Shikha Chauhan illuminate the fascinating world of liquid crystal thermometers. Asif Ali and Jai Prakash, in their exploration of liquid crystals within the realm of Machine Learning, reveal how ML enhances the study of these remarkable substances. The article by SSZ Ashraf discusses several software tools for tensor operations, essential in fields like physics, engineering, and machine learning.

In addition to scientific breakthroughs, this issue honors legacies. Articles like Zafar Ali Khan's tribute to Professor Israr Ahmad and B. P. Singh's exploration of Prof. Harnam Singh Hans' contributions illuminate the enduring impact of educators and pioneers. The final piece, *Superannuated Faculty Roll of Honour (1912–2024)*, chronicles the Physics Department's luminaries who have shaped our journey over a century, preserving their legacy for future generations.

This bulletin reflects our commitment to fostering curiosity, innovation, and collaboration. Each article encapsulates the spirit of scientific exploration, inspiring future generations to expand the frontiers of knowledge.

The editorial team extends heartfelt gratitude to **Mr. Maaz Moonis** for his diligent efforts in composing and preparing the articles, as well as managing the technical aspects. We also express our sincere appreciation to the **Reviewers** for their generous time and thoughtful reviews. Our warm applause goes to the **Authors** who have submitted original contributions for this issue. Finally, the editorial committee deeply values the **Chair, Prof. Anisul Ain Usmani**, for his unwavering support and dedication in ensuring the timely and successful publication of this Bulletin.

We hope this Bulletin inspires readers to appreciate the profound influence of physics across disciplines and its promise for a brighter, more innovative future. Let this collection serve as a beacon of inspiration and a testament to the boundless possibilities of physics.

Below this Editor's Note, you will find a concise summary of the articles featured in this issue, providing an overview of their key insights and contributions.

1. Abdul Quadir and Haider Hasan Jafri highlight the 2024 Nobel Prize in Physics, awarded to John J. Hopfield and Geoffrey E. Hinton for pioneering artificial neural networks (ANNs) and machine learning. Hopfield's network, inspired by spin glass systems, models associative memory and minimizes an energy function akin to the Ising model. Hinton's Boltzmann Machines, based on statistical mechanics, utilize thermal noise to overcome local minima, enabling advanced pattern recognition. These breakthroughs, rooted in physics, bridge biological and artificial neural networks, revolutionizing AI. Their work underpins modern AI applications, from image recognition to healthcare, showcasing the transformative power of interdisciplinary science.
2. Syed Afsar Abbas proposes a new paradigm that unifies physical and biological sciences by introducing independent geometries and quantum mechanics. This paradigm addresses key conundrums in modern physics: quantum nonlocality, dark energy, and dark matter. Using topology, Abbas proposes a hidden geometry, derived from Euclidean geometric constructions, and presents a new approach to quantum mechanics. This framework not only provides

solutions to the solar system's description and quantum gravity issues but also extends to biological sciences, offering insights into consciousness and neurological phenomena. Abbas suggests this new paradigm is a consistent language bridging physics and biology. The editors maintain a neutral stance, inviting readers to explore the author's ideas and form their own interpretations.

3. Sudhir Kumar Gupta and Surabhi Gupta explore the potential of supersymmetry (SUSY) as an extension of the Standard Model (SM) of particle physics. While SM explains fundamental particles and forces, it faces issues like the hierarchy problem and lacks solutions for dark matter, gravity, and neutrino masses. SUSY introduces symmetry between fermions and bosons, solving the hierarchy problem by canceling divergences in Higgs boson mass calculations. SUSY predicts supersymmetric particle counterparts, with the lightest neutralino as a dark matter candidate. Despite no direct evidence yet, experiments like the LHC aim to confirm SUSY, addressing critical gaps in our understanding of the universe.

4. Najimuddin Khan, in *"Will the Universe End? A Particle Physics Perspective"*, discusses the Universe's stability based on the Standard Model (SM) and Higgs potential. He explains that the electroweak vacuum, where the Universe resides, is metastable and could transition to a true vacuum due to quantum tunneling or thermal fluctuations, leading to catastrophic consequences. The discovery of the Higgs boson confirmed key SM parameters, but phenomena like neutrino masses, dark matter, and cosmic inflation suggest the need for physics beyond the SM. New particles can either destabilize or enhance vacuum stability, influencing the Universe's predicted lifetime.

5. The article, authored by Ishfaq Ahmad Rather and Anisul Ain Usmani, titled "Exploring Unusual Measurements of Neutron Stars: HESS J1731-347, XTE J1814-338, and Beyond" discusses unusual neutron star measurements, focusing on HESS J1731-347 and XTE J1814-338. These stars challenge current models of the equation of state (EoS) for dense matter due to their extreme properties. HESS J1731-347's low mass and compact structure suggest exotic internal states, while XTE J1814-338's small radius and high compactness defy standard stiffness constraints. Both cases highlight the need for flexible models accommodating soft and stiff EoS behaviors across density ranges. Observations like GW170817 provide constraints but struggle to reconcile such extremes. Future studies are crucial for unified insights.

6. In *"Largest Scientific Endeavour on Earth: From LEP to LHC"*, Mohammed Mohsin Khan highlights the transition from the Large Electron Positron (LEP) Collider to the Large Hadron Collider (LHC) at CERN. The LHC, housed in a 27 km tunnel, is the world's largest and most powerful particle accelerator, enabling high-energy proton and lead ion collisions. These experiments unravel fundamental cosmic mysteries, including the Big Bang's aftermath and particle physics phenomena. Khan underscores the massive international collaboration, advanced technology, and critical role of detectors like ATLAS, CMS, LHCb, and ALICE in achieving groundbreaking discoveries, exemplifying humanity's quest for knowledge.

7. Exploring the Universe with AMS-02: A Window to Cosmic Mysteries by Meeran Zuberi - The Alpha Magnetic Spectrometer-02 (AMS-02), installed on the ISS in 2011, is a cutting-edge detector studying cosmic rays to explore the universe's fundamental nature. Proposed by Nobel laureate Samuel Ting, AMS-02 aims to detect dark matter, antimatter, and study cosmic ray propagation. Its advanced systems, including magnets, trackers, and calorimeters, enable precise particle identification and measurement. Key findings include unexpected positron excesses and precise measurements of cosmic ray nuclei, antimatter, and deuterons. AMS-02 continues to shape astrophysics, providing unprecedented insights into cosmic phenomena and paving the way for refined cosmic ray theories through planned upgrades.

8. R. Prasad in this write up explains positron emission tomography (PET), a noninvasive imaging technique that identifies abnormal metabolic activity in the body, often signaling early-stage cancer. PET scans use radioactive tracers like fluorodeoxyglucose (FDG), injected into the bloodstream. These tracers accumulate in abnormal cells due to higher glucose consumption, emitting positrons that annihilate with electrons, producing gamma rays. Specialized detectors capture these rays to create detailed 3D images of the affected areas. The technology is safe, with tracers quickly decaying without residual effects. PET scans are invaluable for early diagnosis and treatment planning, exemplifying the crucial role of nuclear physics in healthcare.

9. "Assessing Exposure to Natural Radiation and Health Implications" by B. P. Singh and R. Prasad explores the origins of natural radiation, its health and environmental impacts, and the necessity of evaluating and regulating these sources. The article covers cosmic, terrestrial, and internal radiation from sources such as outer space, uranium, and bodily absorption. It discusses the importance of exposure regulation through units like Roentgen, Gray, and Sievert, with tools like Thermo-Luminescent Dosimeters and gamma spectrometry aiding assessment. Health risks such as lung cancer and genetic mutations are emphasized, along with the need for further research and safety measures to manage these risks effectively.

10. Mohd Shuaib, Aquib Siddique, M Shariq Asnain and B P Singh describe the beta energy spectrum of a ^{90}Sr source using magnetic deflection and a Geiger-Müller counter. Beta particles from ^{90}Sr decay travel through a magnetic field, curving based on their energy. The experiment calibrated a spectrometer using a fixed radius of curvature and varying magnetic fields, correlating field strength to particle energy using relativistic equations. Data revealed a continuous energy spectrum, validating relativistic kinematics and Fermi's beta decay theory. This analysis confirms the precision of the magnetic deflection method for beta spectroscopy, offering insights into nuclear decay and potential applications in nuclear physics and medicine.

11. Aquib Siddique, M. Shariq Asnain, Mohd Shuaib, and B.P. Singh utilized Rutherford Backscattering Spectrometry (RBS) and the α-transmission method provides quick estimates of foil thickness by analyzing energy loss of alpha particles, while RBS offers precise, depth-resolved data, including compositional information. Both techniques yielded consistent results, with RBS proving especially effective for layered materials. The study highlights the complementary strengths of these methods, essential for high-precision material characterization in nuclear physics and material science experiments, ensuring reliable data for studying reaction dynamics and material properties.

12. In this article, the authors, Mubashshara Fatma and Haris Kunari, endeavor to illuminate the foundational principles and intricate processes underpinning the fascinating realm of lasers. Their discourse gracefully narrows its focus to the quintessential three-level (ruby) and four-level (He-Ne) laser systems, both cornerstone topics in undergraduate and master's studies. Despite their academic ubiquity, the authors have discerned a persistent haze of confusion among students, whose understanding of these luminous marvels often remains tethered to oversimplified energy-level diagrams. To dispel these misconceptions, the article unveils an enriched depiction of the He-Ne laser (see Section 5) while weaving together the elegant tapestry of atomic and molecular physics to reveal the profound mechanisms that breathe life into laser technology.

13. Mohammad Adnan highlights the potential of inorganic-organic hybrid perovskites, which merge the complementary properties of organic and inorganic components. These materials exhibit unique structural, optical, electrical, and thermal characteristics, making them suitable for applications in LEDs, photodetectors, lasers, and solar cells. Research in India, initiated by pioneers like Profs. Ram Seshadri and C.N. Rao, has advanced through contribu-

tions from IITs and IISc. Globally, perovskite solar cells have achieved remarkable efficiency but face challenges like thermal instability. Recent studies focus on 2D structures with stable excitons and tunable properties, offering significant potential in optoelectronics and renewable energy solutions.

14. *From Molecules to Megawatts: Let Us Talk About Green Hydrogen* by Adiba and Tufail Ahmad highlights green hydrogen as a sustainable energy solution. It explores its production via electrolysis, applications in power, transport, and industry, and India's proactive role through its National Green Hydrogen Mission. Challenges include costs and infrastructure, but initiatives drive progress.

15. *Trace Element Analysis* by Lalit Bhardwaj discusses trace elements, their impact on material properties, and analytical methods. It categorizes techniques into destructive and non-destructive types, focusing on Neutron Activation Analysis (NAA) and Particle-Induced X-ray Emission (PIXE). These methods identify trace elements with high sensitivity, addressing contamination in various scientific fields.

16. Shubham Gupta, Arbaz Khan, and Shikha Chauhan explore liquid crystal (LC) thermometers, which utilize the unique thermochromic properties of cholesteric liquid crystals to measure temperature. These thermometers display temperature as color changes due to temperature-dependent variations in the helical pitch of LC molecules. LC thermometers are safe, reusable, and customizable, offering advantages over traditional mercury and digital thermometers. Widely used in medical applications like fever strips and industrial monitoring of machinery, they also find use in consumer products such as aquarium thermometers. Their applications extend to cold chain logistics, ensuring safe transport of temperature-sensitive goods like vaccines and perishables.

17. This is the second article on liquid crystals (LCs) that explores their unique characteristics within the highly sought-after field of Machine Learning. Authors Asif Ali and Jai Prakash detail the discovery of LCs, their thermotropic and lyotropic phases, and properties such as birefringence and phase transitions. Machine learning (ML) is highlighted as a transformative tool in LC research, facilitating efficient classification, phase prediction, structural analysis, and responses to external stimuli. Future applications, including reinforcement learning and generative adversarial networks (GANs), are proposed to design LCs with specific properties and optimize their use across various domains.

18. This article by SSZ Ashraf discusses several software tools for tensor operations, essential in fields like physics, engineering, and machine learning. Key tools include Mathematica, which offers both symbolic and numerical tensor manipulation; TensorFlow and PyTorch, widely used for deep learning and general tensor computation; NumPy, a foundational tool for numerical tensor operations; and SymPy, ideal for symbolic tensor algebra. These tools simplify complex tensor computations, enabling efficient problem-solving in multi-dimensional data analysis, optimization, and tensor algebra. Their use is crucial for researchers and engineers working with large datasets, theoretical research, and machine learning applications.

19. The document, authored by Zafar Ali Khan, is a tribute to Professor Israr Ahmad, celebrating his remarkable contributions to theoretical nuclear physics and education. It highlights his pioneering work in quantum scattering theory, nuclear reaction dynamics, and the Coulomb-modified Glauber model. The article emphasizes his role in advancing modern education through initiatives like the Centre for Promotion of Science at Aligarh Muslim University, where he bridged the gap between traditional and modern educational systems. Prof. Ahmad's collaborations with leading scientists worldwide, including Nobel Laureate Prof. Abdus Salam, and his mentorship of numerous scholars, have left a lasting impact on the scientific

community. Beyond his academic achievements, his dedication to Sir Syed Ahmad Khan's vision of promoting scientific education among religious seminaries is also acknowledged. Prof. Zafar Ali Khan reflects on how Prof. Ahmad's work continues to inspire future generations

20. The Physics Department at Aligarh Muslim University (AMU), founded in 1908, has a rich history in nuclear physics, significantly influenced by pioneers like Prof. Harnam Singh Hans. In this article, *The Visionary Legacy of Prof. Harnam Singh Hans in Accelerator-Based Nuclear Physics*, B. P. Singh honors Prof. Hans's transformative role in establishing AMU as a hub for experimental nuclear physics. Prof. Hans, often called the "Father of Accelerator-Based Nuclear Physics in Indian Universities", constructed India's first Cockcroft-Walton neutron generator in 1958, laying the foundation for nuclear research. Later, he brought a cyclotron to Panjab University, further advancing nuclear research in India. His legacy continues to inspire future generations of scientists and researchers.

21. The last document in this Bulletin, titled *Superannuated Faculty Roll of Honour (1912–2024)*, chronicles the retired faculty of the Physics Department at Aligarh Muslim University. It highlights the department's legacy, listing 103 members, their tenures, and leadership roles, preserving this history for future generations through detailed documentation.

EDITORS

SSZ Ashraf
Jai Prakash

PHYSICS BULLETIN

Editors:

S.S.Z. Ashraf
Jai Prakash

Reviewers:

Bhanu Prakash Singh
Anisul Ain Usmani
Shakeel Ahmad
M. Wasi Khan
Haider Hasan Jafri
Sudhir Kumar Gupta
Raktim Abir
Arif Mohd

CONTENTS

From Physics to AI: The Nobel Prize in Physics 2024

Abdul Quadir and Haider Hasan Jafri
Department of Physics, Aligarh Muslim University, Aligarh, UP, India-202002

Abstract

The Nobel Prize in Physics 2024 was jointly awarded to John J. Hopfield and Geoffrey E. Hinton "for foundational discoveries and inventions that enable machine learning with artificial neural networks" [1]. The two Nobel Laureates have used tools from physics to develop methods that are the foundation of today's powerful machine learning. John Hopfield created an associative memory that can store and reconstruct images and other types of patterns in data [2]. Geoffrey Hinton invented a method that can autonomously find properties in data, and perform tasks such as identifying specific elements in pictures [3]. Their pioneering work has significantly advanced the field of artificial intelligence (AI), leading to technologies that are now integral to various aspects of modern life, from scientific research to everyday applications.

1 Introduction

A fundamental property of intelligent biological systems, such as the human brain, is their ability to assimilate new knowledge, thereby enhancing their capabilities. This is a signature of interrelatedness between memory and learning. Thus, in neuroscience, it is of fundamental importance to understand how a human brain learns. The organic brain consists of neurons that are organized in a hierarchy forming a biological neural network. These neurons are the nerve cells that show activation and interconnectivity to perform a given task.

With the advent of modern computers, there has been a renewed interest in developing artificial systems that can be trained using inputs to produce desired outputs, such as classification and regression. J. Hopfield, inspired by the studies in neurobiology and molecular physics, proposed that such a task can be accomplished with the help of a network of nodes (or neurons). These networks, known as Hopfield networks, were among the earliest artificial neural networks (ANNs). ANNs comprise nodes with coded values that serve as fundamental computational units. These nodes are organized into layers, receiving inputs, processing them, and passing their outputs to subsequent layers. The connections between active nodes strengthen, whereas the connections between inactive nodes remain weak. Although the networks proposed by Hopfield would demonstrate modest practical benefit, they were able to store and retrieve data. The idea of Hopfield networks was further extended by Hinton, who introduced the concept of *Boltzmann Machines* (BM). BMs are energy-based models that utilize an energy function to learn a probability distribution over their inputs. This approach allows them to model complex, high-dimensional data.

Connecting to physics: Hopfield's paper draws inspiration from systems comprising numerous interacting elements, exhibiting collective behavior [2]. He argued that this behavior is akin to that of a "spin glass", consisting of disordered magnetic particles. Hopfield networks share a Hamiltonian identical to the Ising model [4, 5], leading to stable magnetic orientations and domains. Hinton and his colleagues drew from statistical mechanics—a field describing the statistics of particle ensembles—to introduce Boltzmann Machines. Named in honor of Ludwig Boltzmann, whose work laid the foundation for statistical mechanics, the BM is a spin glass model with an external field, also known as the Sherrington–Kirkpatrick model [6].

In this article, we will explore two foundational models in machine learning and artificial intelligence: Hopfield Networks and Boltzmann Machines. These models have played crucial roles in the evolution of neural networks. We will begin by outlining the basic principles and fundamental ideas that laid the groundwork for contemporary advances in unsupervised learning, optimization, and pattern recognition, which are central to many modern AI applications.

1.1 Biological Neural Network

A biological neural network consists of a population of neurons that are interconnected. These networks are helpful in understanding the details of nervous system. A neuron (nerve cell) is capable of firing electrical signals called action potential. The potential difference between the interior and the exterior of the cell is called membrane potential. This potential continously changes, and the stimulating

neuron thus produces action potential that propagates with the help of axon. The axon divides into a large number of branches through which the signal is transferred to other neurons. These connecting sites are called as synapses. Through these synapses, other neurons of the network are activated releasing neurotransmitters. Schematic representation of a biological neuron is shown in Fig. 1.

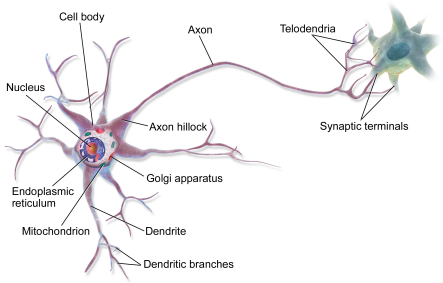

Fig. 1: *Schematic diagram of a biological neuron. Adapted from Ref. [14].*

1.2 Artificial Neural Networks (ANN)

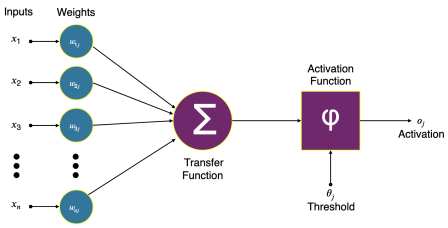

Fig. 2: *Schematic diagram of an artificial neural network. Adapted from Ref. [15].*

A network (or a graph) is a structure that consists of a set of vertices (nodes or points) that are connected through edges or links. These edges may be directed if they have a sense of direction, otherwise they are undirected. If one assigns a number (the weight) to each edge, these are called weighted graphs. An artificial neural network is a directed graph where nodes are described by state variables n_i for each node i having a bias ϑ_i. A node i may be connected to the other node k such that the weight corresponding to the link ik is given by w_{ik}. Further, a transfer function $f_i(n_i, w_{i,k}, \vartheta_i)(k \neq i)$ decides the activation of a neuron. To describe the relation with the biological neuron, the links are called as the synapse, ϑ_i is the activation threshold and f_i corresponds to the activation function. An example of an artificial neural network is shown in Fig. 2.

The neurons can be hidden if they do not communicate with the external environment. Hidden neurons receive signals from other neurons in a network. Another set of neurons may be visible in the sense that they receive signals from the external environment. A visible neuron acts as both the input device and the output device.

Initial contributions to the neural network research was made by McCulloch and Pitt who proposed the calculus for developing a nonlinear model for neural behaviour [7]. Based on these ideas, Rosenblatt (1958) proposed perceptron, that is a commonly used artifical neuron in neural networks. Further, Amari's proposal to consider the modified Ising model as an ANN was an initial model of associative memory and was further popularized by J. Hopfield [2, 4, 5, 8, 9].

2 The Hopfield Network

John J. Hopfield is a renowned physicist and biophysicist whose work has profoundly influenced the fields of neuroscience, artificial intelligence, and computational physics. His most notable contribution is the introduction of the Hopfield Network, a type of recurrent neural network that models associative memory and computation in a biologically inspired manner [2, 9, 8]. The Hopfield network bridges the gap between physics and cognitive sciences, making Hopfield a pivotal figure in interdisciplinary research.

2.1 Overview

The Hopfield Network, introduced in 1982, is a form of artificial neural network designed to simulate memory retrieval processes. It consists of a fully connected network of binary or continuous neurons, where each neuron influences every other neuron symmetrically. It is primarily used for associative memory and pattern recognition. Hopfield networks have connections that form a feedback loop, where the output of neurons is fed back into the network. This feedback is the key to the network's ability to store and retrieve patterns. Hopfield's network is a recurrent artificial neural network which means that it operates in a cycle constantly feeding information back into itself. The network is designed to store patterns. If the input is fed in the form of partial pattern, it will attempt to complete it based on the patterns that are stored. This process is known as associative memory.

2.2 Key Features

- **Binary Neurons** The original Hopfield Network used binary neurons. Later, continuous versions were introduced, extending its applicability to a wider range of problems.
- **Fully Connected Networks** It is a fully connected network, where a given node is connected

to all other nodes.

- **Energy Function** The Hopfield Network is deterministic and the Hamiltonian is similar to that of the Ising model [4, 5]. It operates on the principle of minimizing an energy function, similar to how physical systems move toward minimum energy states. The energy function is defined as:

$$E(S) = -\frac{1}{2}\left[\sum_{ij}^{i\neq j} w_{ij}s_i s_j\right] + \sum_i \vartheta_i s_i. \quad (1)$$

- **Associative Memory** The network can store patterns as stable states or attractors. When presented with a partial or noisy version of a stored pattern, the network converges to the closest stored pattern, mimicking how human memory retrieval works.

2.3 Hopfield Networks: Mathematical Architecture

The nodes in the Hopfield network are simplifications of real neurons, they can only exist in one of two possible input patterns- (a) binary input vector $s_i \in \{0, 1\}$ [2] or (b) bipolar input vector $s_i \in \{-1, +1\}$ [9]. The Hopfield network at any time t can be described by considering a state vector $S(t) = [s_1(t), s_2(t), \ldots s_n(t)]^T$, where T represents the transpose. Here, s_i represents the state of the i^{th} neuron, where $s_i(t) \in [-1, 1]$. The strength of connection between two neurons is described by the weight matrix w_{ij}. The synaptic (or weight) matrix W, for the binary input, can be written as

$$w_{ij} = \sum_p (2s_i(p) - 1)(2s_j(p) - 1), \quad (2)$$

which gives the synaptic matrix

$$W = \begin{bmatrix} w_{11} & w_{12} & \ldots & w_{1n} \\ \vdots & \ddots & & \\ w_{n1} & & & w_{nn} \end{bmatrix},$$

that satisfies the conditions, $w_{ij} \in \mathbb{R}$, $w_{ij} = w_{ji}$ and $w_{ii} = 0$. Further, there is an activation threshold ϑ_i for neuron i. Thus, we define an activation threshold vector $\vartheta = [\vartheta_1, \vartheta_2, \ldots, \vartheta_n]^T$ with $\vartheta_i \in \mathbb{R}$. In Fig. 3, we show a schematic diagram of a Hopfield network having three nodes $N_i (i = 1, 2, 3)$ with synaptic weights $w_{ij} (i, j = 1 \ldots 3, i \neq j)$.

In the Hopfield network, each node acts as an input and output device. The network is trained (learning) by introducing the environmental pattern through the state vector $S(t)$. The network thus computes a suitable weight matrix. When an incomplete or noisy version of $S(t)$ appears, the network evolves dynamically to complete (correct) the pattern. The evolution of Hopfield network involves calculating the synaptic potential given by

$$h_i(t) = \sum_{j=1}^{n} w_{ij}s_j(t). \quad (3)$$

The update rule for each neuron is given by

$$s_i(t+1) = \Theta[h_i(t) - \vartheta_i] = \Theta\left[\sum_{j=1}^{n} w_{ij}s_j(t) - \vartheta_i\right], \quad (4)$$

where Θ is the Heaviside function.

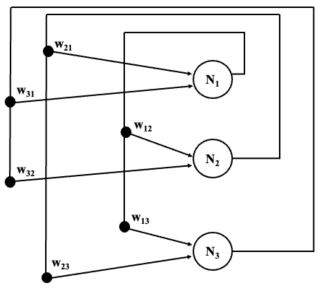

Fig. 3: *Hopfield neural network structure.*

The dynamical behaviour of the Hopfield network is modelled by an *energy* or *Lyapunov* function associated with a state vector $S(t)$ given by Eq. 1. It was shown that the energy $E(S)$ decreases continuously with time i.e., $E_i(t+1) \leq E_i(t)$. This allows the network to find the stable state defined by the synaptic matrix. This relaxation process is related to the operation of human memory. The Hopfield network has a very low capacity owing to the fact that the network often reaches a local minima instead of a global one. These locally stable minima may not conform to the actual solution.

3 Geoffrey E. Hinton's Contributions and Boltzmann Machines

Geoffrey Hinton, often referred to as the "godfather of AI", made significant contribution in developing deep learning techniques. He introduced the idea namely back-propagation that allows neural networks to adjust their parameters and improve performance through learning. Hinton's work has been useful in enabling machines to recognize patterns, understand speech, and interpret images, that has resulted in many AI applications today.

3.1 Boltzmann Machines: An overview

Recall that in case of Hopfield networks an important requirement is finding the minimum energy state. However, due to the presence of metastable states, the system does not reach global minima rather the resulting state may be a local minima. As a result the network may behave incorrectly because these locally stable states do not conform to any intended solution. Boltzmann Machines (BMs), introduced in 1985 by Hinton and Terry J. Sejnowski, are stochastic neural networks inspired by statistical mechanics. They consist of a network of interconnected neurons (or units) that use energy-based models to learn and represent probability distributions over datasets. Cragg and Temperley [10] compared system of fully connected neurons with system of atoms on a lattice (Ising model) and concluded that

1. The emergent behaviour in a neural network may show patches of excited or quiescent neurons similar to the ones formed in ferromagnet that consists of patches containing up $(+1)$ or down (-1) spins.
2. The formation of neural domain patterns, as a result of an external stimuli, are stable and constitutes a memory of the stimuli.

Based on this analogy, Sherrington and Kirkpatrick in 1975, described a new magnetic material *the spin glass* [6]. The spin glass consists of spins that interacts ferromagnetically and antiferromagnetically has no net magnetism. With the help of this property, it is possible to store many different disordered spin patterns [11].

The architecture of a Boltzmann machine is identical to that of the Hopfield network. The neurons are represented as binary $[0, 1]$ or bipolar [-1,+1] units. The neurons in a Boltzmann machine are divided into two categories [cf. Fig. 5],

1. Visible neurons that are used as input or output device denoted by $N_i (i = 1, \ldots 3)$ as shown in Fig. 5.
2. Hidden neurons that interact only with other neurons denoted as $M_i (i = 1, \ldots 4)$ in Fig. 5.

In this case, the Lyapunov function is the same as described for the Hopfield network (Eq. 1) where the summation now runs over both the visible and hidden neurons. However, the activation function is now defined as

$$f(h_i) = \left[\frac{1}{1 + e^{\frac{-h_i(t)}{T}}} \right] \tag{5}$$

where T gives the thermal noise (randomness) in the system. A unique characteristic of the Boltzmann machine is that the probability with which a given neuron changes its state is independent of its previous state. The thermal or stochastic noise helps the network to reach the global minima without getting trapped into the locally stable states. If the temperature is fixed, the BM reaches an equilibrium. In this situation, it is convenient to express the probability of two globally stable states with the help of Boltzmann distribution given by

$$\frac{P_\alpha}{P_\beta} = e^{-\left(\frac{E_\alpha - E_\beta}{T}\right)} \tag{6}$$

where $P_\alpha (P_\beta)$ is the probability of being in the global state $\alpha(\beta)$ having energy $E_\alpha (E_\beta)$. Boltzmann learning is done by first operating the network at high temperature and then gradually lowering it until the equilibrium is reached.

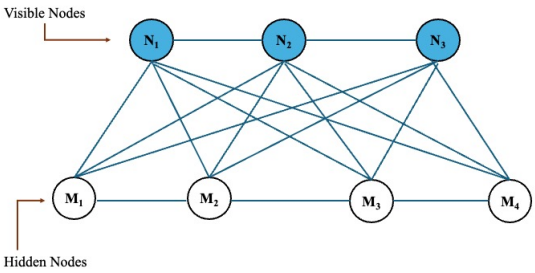

Fig. 5: *A general architecture of the Boltzmann Machines.*

4 Machine Learning and Artificial Intelligence

Artificial Neural Networks (ANN), Machine Learning (ML), and Artificial Intelligence (AI) are all interrelated fields, with each building upon the other.

1. *Artificial Intelligence (AI):* AI is a broad concept, referring to the development of machines and computers that can perform tasks that would require human intelligence. These tasks can include reasoning, learning, problem-solving, perception, language understanding, and decision-making. AI can be classified into many subfields namely robotics, natural language processing, computer vision, and more.
2. *Machine Learning (ML)* ML is a subfield of AI where the focus is to create algorithms that enables the system to "learn" from data, identify patterns, and make predictions without any manual coding. ML models are trained on large datasets to make inferences. ML is a core method

through which AI is achieved, as it empowers machines to improve over time through experience.

Recall that the ANNs are the basic building blocks and are considered as class of algorithms in machine learning that are inspired by the structure and functioning of the human brain. They consist of layers of interconnected "neurons" (nodes) that process information and learn patterns from data. ANN models are particularly effective for tasks like image recognition, speech processing, and complex pattern recognition. ANN is one of the many approaches used in machine learning. While ML includes a wide range of other algorithms, ANNs are a powerful and flexible tool, especially for complex, unstructured tasks. Machine learning is one of the primary technique of implementing AI. In this sense, ML serves as a tool for creating intelligent behavior in machines. AI systems that use ML models (including ANNs) can perform tasks namely recognizing objects in images, understanding spoken language, or predicting trends in large datasets. Thus, AI systems that use machine learning, including ANN models, are able to perform "intelligent" tasks autonomously. The ultimate aim of AI is to replicate human-like intelligence in certain domains, and ML has proven to be one of the most useful approaches to achieve this. Thus, ANN is an important tool within machine learning, which in turn is a critical component of AI. Together, they enable machines to learn, adapt, and make decisions based on data, with the goal of creating AI systems that are able to mimic human-level capabilities.

5 Conclusion

The work of John Hopfield and Geoffrey Hinton has been instrumental in shaping the modern landscape of AI and machine learning. Hopfield's early contributions to neural network architecture and associative memory laid critical groundwork, while Hinton's pioneering work on Boltzmann machine resulted in further advancement. The Hopfield network and the Boltzmann machine share close connection with the the Ising model which is one of the most thoroughly studied models in statistical mechanics. Thus, over several decades, research at the intersection of statistical mechanics, neuroscience, and computer science has played a pivotal role in the information processing in both living systems and machines. With the advent of modern computers, numerous learning algorithms have been proposed that have found widespread application in tasks such as image classification, natural language processing, and anomaly detection. As a result, AI has transformed from a theoretical field into one of the most transformative technologies of the modern world, influencing everything from healthcare to transportation, entertainment, and beyond.

References

[1] `https://www.nobelprize.org/prizes/physics/2024/summary/?utm-source=chatgpt.com`

[2] J. J. Hopfield, Neural networks and physical systems with emergent collective computational abilities. *Proceedings of the national academy of sciences*, **79**(8), 2554 (1982).

[3] D. H. Ackley, G. E. Hinton, and T. J. Sejnowski, "A learning algorithm for Boltzmann machines," *Cognitive Science* **9**, 147 (1985).

[4] D. J. Amit, H. Gutfreund, and H. Sompolinsky, "Spin-glass models of neural networks," *Physical Review A*, **32**(2), 1007 (1985).

[5] T. Ising, R. Folk, R. Kenna, B. Berche, and Y. Holovatch, "The fate of Ernst Ising and the fate of his model," *Journal of Physical Studies*, **21**, 3002 (2017).

[6] D. Sherrington and S. Kirkpatrick, "Solvable Model of a Spin-Glass," *Physical Review Letters* **35**(26), 1792 (1975).

[7] W. S. McCulloch and W. Pitts, "A logical calculus of the ideas immanent in nervous activity," *The Bulletin of Mathematical Biophysics* **5**, 115 (1943).

[8] S.-I. Amari, "Learning patterns and pattern sequences by self-organizing nets of threshold elements," *IEEE Transactions on Computers* **100**(11), 1197 (1972).

[9] J. J. Hopfield, "Neurons with graded response have collective computational properties like those of two-state neurons," *Proceedings of the national academy of sciences*, **81**(10), 3088 (1984).

[10] B. G. Cragg and N. V. Temperley, "The Organization of Neurones: A Cooperative Analogy," *EEG Clinical Neurophysiology*, **6**, 85 (1954).

[11] J.D. Cowan and D.H. Sharp, "Neural Nets," *Quaterly Reviews in Biophysics* **21**, 365 (1988).

[12] https://en.wikipedia.org/wiki/Neuron#/media/File:Blausen_0657_MultipolarNeuron.png

[13] https://commons.m.wikimedia.org/wiki/File:Artificial_neuron_structure.svg

Two independent geometries with two independent quantum mechanics - a new paradigm for unification of the physical and the biosciences

Syed Afsar Abbas
Centre for Theoretical Physics, JMI University, New Delhi, India-110025
Centre for Cosmology and Science Popularization, SGT University, Delhi-NCR, Gurugram, India-122505

Abstract

This article is specially addressed to the undergraduate and graduate students. Present physics is faced with three most puzzling conundrums due to the recent empirical discoverires of non-locality in quantum mechanics, dark energy and dark matter in cosmology. The situation is no less serious than the crisis faced at the end of the 19th Century, which ultimately culminated into the present revolutinary mathematics and theories of relativity and quantum mechanics. Cleary now appropriate new mathematics and new physical structures, in terms of relevant and consistent new paradigm is needed. In this paper, we do this within the field of tologlgy. This allows us to take circle and line as the lowest two one-dimensional entities within topology (quite unlike in geometry where a circle is treated as two-dimensional). Usisng Euclid's Geometric Constructions, we discosver a new hidden geometry with its own new hidden quantum mechanics. This success finds immediate application in terms of providing a better and complete description of our solar system. Not only that it also provides a solution of the present crisis of the quantum gravity problem. Most amazingly, this new paradigm works well in biological scienecs too. It leads to giving a consistet geometrical description within the neuroscienes and issues relating to the mysterious consciousness. So this new paradigm seems to be providig a consistent language of both the physical and the biological sciences.

Keywords: Nonlocality, dark energy, dark matter, new geometry, new quantum mechanics, solar system, quantum gravity, topolgy. new paradigm, biosciences, consciousness.

1 Introduction

Flushed with great successes of the contemporary structures of physics and mathematicis along with the base of ether, Lord Rayleigh at the end of 19th Century announced that physics had achieved its pinnacle and only minor corrections is all future is left with. With our hindsight, we can see how wrong he was. This was the beginnimg of the amazing theory of relativivty and soon the birth of quantum mecahnics which shook up classical physics at its roots.

These two together changed the whole paradigm of the exsisting phyics. All this has culminated today into a very successful Stadard Model of Particle Physics an the Standard Model of Cosmology. First starting with the unified theory of the electromagnetic and the weak interaction in giving Nobel Prize to Salam, Weinberg and Glashow in 1979 for their model of $SU(2)_L XU(1)_Y$ [1]. Same spirit of unfication led to uniifying the strong force with it in terms of group structure $SU(3)_C XSU(2)_L XU(1)_Y$.

But the above Standard Model had a shortcoming that it displayed no charge quantization in it. Charge quananization was howeve basic to Grand Unified Theories like the $SU(5)$ *and* $SO(10)$ [1]. It took a little while before it was shown by Abbas [2,3], on fully consistent and complete basis, that the electric charge is actually quantized in the Standard Model, and that too with colour dependence in it [1,2,3]. Thus the Standard Model is a unified theory of the the three- strong, electromanetic and weak forces. Gravity lies outside its purview. That is defined well by a semi-classical General Theory of Relativity.

These successes of present theories in physisc and mathematics have continued unabated. This has led many like Stepehen Hawking and others, to claim that at present again we have reached the pinnacle of our acievenemt in terms of having achieved a Theory of Evereything (TOE). Again nothing left to discover!

But, like a thunder, the history is repeating itself.

2 Three Empirical Conundrums for Modern Physics

The first cononundrim is the discovery of the nonlocality problem in qunatum mecahnics, for which Aspect, Zeilinger, and Clauser were awarded the 2022 Nobel Prize for the empirical discovery of this extremely puzzling phenomenon. The next one has to do with the empirical discovery of the Dark Energy problem for which Saul Perlmutter, Brian Schmidt and Adam Riess were awarded the Nobel Prize in 2011. The third one is called the Dark Matter problem which has to do with the empirical reality that for eaxample, in our own galaxy, the amount of matter which relates to or Standard model and our gravity model is only miniscule apprx. 5 percent. Amazingly the rest of apprx 95 percent is invisible to us and is called the mysterious Dark Matter.

All these are anathema to all our best understanding of nature as of now. Clearly our we are missing something in our mathematical and physicsal picture. Who knows what mysterious realities are lying hidden fron us. Some new paradigm may be waiting to reveal itself. One has to be open to new and promising ideas.

In the wake of the discovery of the Dark Matter, we expect huge expansion of knowledge, and ofcourse several Nobel Prizes too. Already, new conclusions that the extinction of dinosaur was actually caused by dark matter [4], which actually led to creation of gigantic flood basalt volcanism which led to this catastrople. Not only this, it also explained all the Five Major Mass Exticnctions in the history of Earth [4]. Zioutas [5] has come up with the interesting idea that the dark matter when interacting with living tissue could cause irreparable cancer in cells. This may be attributed to the large number of unknown causes of cancer in human. Abbas and Abbas [6], then showed that this could also cause mass extinctions through cancer too. Hence clearly the dark matter is having impact in biological scienes too.

3 Mathematics and Physics

Mathematics, because of the fact that it is the language of nature, it is essntial to make any progress in the sciences [1,7,8]. All our success have been through judicious application of this powerful language. But we appaer to have reached a saturation point of our understanding at present.

All the above was based on some basic paradigm. Clearly we need some new paradigm which we will allow us to proceed further. Let us adopt an historical approach to seek out the hidden reality. As we struggled to get to the bottom of things, could be that when at a particular instance we chose to go along a path, the path we left, may have had some unique secret of its own. Let us try along this line.

4 Democritus' atom versus our modern atom

Democritus (460-370 BC) proposed a model of "atom" for various elements. The word atom in Greek means "indestructible". Thus in late 19th century Rydberg proposed a picture of indestructible atoms. One example of the same is given in Fig. 1. Here hydrogen, oxygen and sodium are all of rigid shapes. But later Rydberg's model was discarded and models proposed by Thomson, Rutherford, Bohr and others, with atoms, made up of several pointlike electons and protons, forming complex molecules and which were also destructible, were found to give a good description of the physical reality, and hence form the basis of our present successful models.

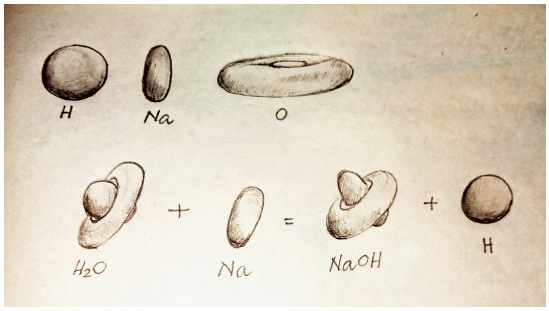

Fig. 1: *Rydberg's model for a chemical reaction using Democratus kind of unbreakable elements*

Note that model like Rydberg's used indestructible "shapes" in three dimensional space $\mathbb{R}^3$. Perhaps this idea did not work because we looked at the whole three dimensional space. Perhaps in the smallest dimensional space, i.e. the one-dimensioanl space $\mathbb{R}$, there may exist simpler shapes which may be more useful as models of indestructible atoms.

A straight line, looks like the simplest shape in the lowest dinesionaol space. Could this be the shape that we are looking for?

5 Circle versus Ellips

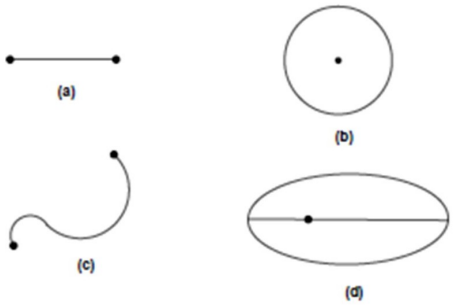

Fig. 1: *Line, Circle, Curve and Ellipse*

Newton could not derive the Kepler's laws of planetary motion using the geometry of circles and straight lines [9]. He was compelled to develop the new language of differential calculus to be able to deal with the ellipses, and thus derive Kepler's laws of motion using his law of gravitation.

So what Newton rejected, may be the new geometric freedom that we are seeking here. Thus a circle may be the missing/hidden indestructible shape.

Thus the indestructible shape as per Democritus - a straight line, and a circle as per Newton-Kepler problem, may be the right shapes to build suitable new geometrical models!

6 Geometry versus Topology

But we have a deep problem. The circle in two dimentional geometric space $\mathbb{R}^2$, can be deformed into an ellipse; and a straight line into curved line in one-dimetional space $\mathbb{R}$ (Fig. 2).

Geometrically, a straight line is a one-dimensional entity existing in $\mathbb{R}$ space, a circle is a two-dimensional space entity in $\mathbb{R}^2$ space.

However in topology, one classifies objects in terms of "shape" in the most general sense [1]. There are just two one-dimensional shapes: a line, which is a curve with two open ends, and a circle, which is a closed curve with no ends. Thus as per topology, there are only these two (line and circle) fundamental and independent shapes [10,11]. Note that thus the "geometry" related to these two independent one-dimensional shapes should be in some new hidden one-dimensional geometric space $\mathbf{R}$.

To belabour the point, note that in topology we are talking about shapes. Hence if we associate a shape with an entity or some distinguishable physical reality, then whatever changes that may occur, the shape of that entity or the distinguishable reality shall not change. It is indeed indestructible as per Democritus, albeit in its new avatar.

Amazingly geometry of pure-circle-line, is what was being done by the ancient Egyptian-Greek geometers, in Alexandria in Egypt. Hence it is to them, that we turn to, for further directions to develop our topological line-circle model.

7 Euclid's Geometric Constructions

To pursue this line of thinking, let us look at Euclid's geometry with emphasis on geometric constructions [12-17].

Euclid's Geometric Constructions are structures which can be built or constructed by using the Euclidean tools of a "straightedge" and a "compass". The straightedge, with no marks etched on it, is used to draw straight lines through any two given points, and which can be extended. With the Euclidean compass, we can draw a circle that passes through a given point and a given centre. This Euclidean compass, unlike our modern school compass, is "collapsible", i.e. once a circle is built, on lifting, the compass will fold up and another circle of the same size could not be drawn reliably. Thus one can draw only one circle at a time.

A construction is a method of demonstrating the existence of a geometric object. Since a construction is a direct means of showing that an object actually exists, Euclid posited much faith in such geometric constructions to provide an understanding of the physical reality.

Very often the modern geometers feels that, though Euclid's work was a useful starting point, we are far ahead of this ancient work [13]. However, we should be alert of the inherent danger of "throwing away the baby with the bathwater".

However, unfortunately the above discussion misses an essential aspect of the ancient Egyptian and Greek style of doing geometry through constructions. Basically everyone implicitly assumes that all geometric constructions, and hence the only geometric constructions that they did, was done on a piece of paper (or papyrus sheets made from weeds abundantly grown in Nile). But Euclid never advocated that. Klein states [13,p.190], "How little thought Euclid gave to applications, ... appears clearly from the fact that he does not once mention even the simplest drawing instruments - the ruler and compasses. He merely postulates. in the abstract that one can draw a line through two points, or a circle

about a point, without devoting a single word to how one does it." He further explains, "Here Euclid is doubtless under the influence of the notion which prevailed in certain schools of philosophy, that practical application of a science was something inferior, artisan-like."

However, I surmise that Euclid did not think of mentioning the straightedge or the compass or the papyrus in the framewrork of his discussion, as it was probably not needed, or was an obvious or a trivial fact. Important is to understand the whole process of how these constructions were actually done by the ancient Egyptian or Greek geometers?

Papyrus would be limited in number and very expensive. Thus before putting a particular geometric construction onto papyrus, they would have liked to experiment on a cheap and a more easily accessible plane surface. And where would such a cheap surface be available to them? Naturally they would go to a flat sandy area (e.g. near a beach or near Nile). Only after playing around with a large number of figures through geometric constructions on sand, would they also record it on papyrus. That would sanctify their initial work done on sand. So experimental and initial work done on sand, and the final work/result put on papyrus, was apparently the modus operandi of the Egyptian and Greek astronomers.

To support the above assertions of geoemtric work on sand, and the significance of this to the papyrus constructions, we give these examples. First, may I remind the reader of the story of how Archimedes was killed by an enraged Roman soldier, when he scolded the soldier, "Stand away from my diagrams!". The second example, may be gleaned from the Brittanica Junior Encyclopaedia entry about Euclid [18], "Surrounded by his followers and pupils, he would spread a layer of sand on the floor. With the point of a stick,he would draw geometrical figures, explaining as he did so his theorems and proofs."

This view is in resonance with that of Heath [12,Vol.1 p.259], who states, "The reason why Euclid allowed himself to use, in this enumeration, language apparently so obscure is no doubt that the phraseology was traditional, and therefore, vague as it was, had a conventional meaning which the contemporary geometer well understood."

Thus Euclid did not think it worth his while to talk about these "obvious facts", and which were an implicitly "understood" aspects of the culture of geometry in Egypt and Greece at that time.

Note that only an asymmetric compass (with the centre nail being different from the other point as a pencil or a chalk) is needed to draw circles on a paper or a papyrus sheet. Thus a collapsible compass would necessarily be an asymmetric compasss and could draw only one circle at a time on papyrus.

However to draw circles on sand, while one has access to an asymmetric compass, there exists an additional freedom to use a fully "symmetric" compass, which may have physically identical appearing nails to use as the centre point or the circle point. This new feature allows us to exchange the centre point and the circle point without lifting the compass, i.e. without collapsing the compass when a circle is completed. This new feature which brings in a new symmetry in our constructions shall prove to a very powerful new degree of freedom available to us.

8 Use of the new topological paradigm

With the above kmowledge of Euclidean Gometric Construction in the new geoemtric framework of the circle-line within the one diemnsional reality has allowed us to apply this new topological paradigm to many successes:

- Apply it to our solar system to overcome two basic shortcomings of the Newton's laws and the Keplers laws. The reader is referred to read this paper - https://www.researchgate.net/publication/385694220; Exoplanets, Titius-Bode-Like Law in Astronomy, Limitimg Form of Special Theory of Relativitty, and a New Quantum Mechanics.

- Apply it to solving the outstanding quantum gravity problem in a recent paper - https://www.researchgate.net/publication/386556070; A consistent quantum gravity model enforced through a new geometry with explicit space and time quantization.

This shows that the potential of this new new geometry with its own quantum mechnaics is turning out to be a good and consistent paradigm.

9 New paradigm and biological sciences and consciousness

One amazing thing that we have discovered is that this new paradigm is not only useful for the physical scienes, it is all encompassing enough to find interesting applications in the understanding of mysteries of the consciousness and the biological sciences.

The following three recent papers of ours attest to this fact:

- https://www.researchgate.net/publication/37950 9287; Human Brain, Hemispatial Neglect, Consciousness, and Topology
- https://www.researchgate.net/publication/38043 2630; Neanderthal had the same consciousness as that of the present left-spatial-neglect human!
- https://www.researchgate.net/publication/38110 9975; Why did Homo sapiens evolve in Africa and not some where else?

Given these successes, the author feels that this new paradigm should be reflecting new fundamental realitiess of our Nature. Thus this idea should be taken forward.

References

[1] S. A. Abbas, "Group Theory in Particle, Nuclear, and Hadron Physics", CRC Press, Taylor and Francis, USA, 2016

[2] A. Abbas, "Anomalies and charge quantizationin the Standard Modelwith arbitrary number of colours", Phys. Lett. B 238 (1990) 344

[3] A. Abbas, "Spontaneous symmetry breaking, quanntization of the electric charge and the anomalies", J. Phys. G 16 (1990) L 163

[4] Samar Abbas and Afsar Abbas, "Volcanogenic dark matter and mass extinctions", Astroprticle Physics 8 (1990) 317

[5] K. Zioutas, "Evidence of Dark Matter from biologicak observations", Phys. Lett. B 242 (1990) 257

[6] Samar Abbas, Afsar Abbas and Shukadev Mohanty, "Anoxia during the Late Permian binary mass extinction and dark matter", Current Science 78 (2000) 1290

[7] A. Abbas, "Philosophy of Science - a new perspective", Indian Institute of Advanced Study, Simla, India, 2006.

[8] A. Abbas, "Mathematics as an exact and precise languagee of natute", cogprints.org/4616.2006

[9] G. Gamow, "Gravity", Dover Pub., 2002 (First pub. 1962)

[10] S. Mukhi and N. Mukunda, "Introduction to Topology, Differential Geometry and Group Theory for Physicists", Wiley Eastern Limited, New Delhi,1980

[11] Shing-Tung Yau and S Nadis "The Shape of Inner Space",Basic Books, 2010,

[12] T. L. Heath, "The Thirteen Books of Euclid's Elements" 1925, Cambridge Univ. Press (reprinted Dover 1956)

[13] F. Klein. "Geometry-Elementary Mathematics from an Advanced Standpoint", Dover (German 1908) 1959

[14] H. Eves, "Fundamentals of Modern Elementary Geometry", Jones Bartlett Pub., 1992

[15] G. E. Martin, "Geometric Constructions", Sprnger, 1998

[16] M. O'Leary, "Revolutions of Geometry", Wiley, 2010

[17] E. E. Moise, "Elementary Geometry from an Advanced Standpoint", Addison Wesley, 1990

[18] Britannica Junior Encyclopaedia, Vol. 5, p. 375, (Encylopaedia Britannica Inc., Chicago, 1980)

Is the World Supersymmetric?

Sudhir Kumar Gupta and Surabhi Gupta
Department of Physics, Aligarh Muslim University, Aligarh, UP, India-202002

1 Introduction

According to our current understanding, the observed matter is made up of a set of elementary particles known as quarks and leptons. These interact with each other by means of the four fundamental forces of the nature, namely the electromagnetic, weak, strong, and gravitational force via the force carrier particles known as gauge bosons *e.g.* the electromagnetism is mediated by quanta known as photons. A unified framework analogous to electromagnetic which describes the matter and their mutual interactions (except gravitational) is known as the Standard Model (SM) of particle physics. As the SM is a highly symmetric theory involving symmetries associated with each of the fundamental interactions as well as the space-time symmetry, it forbids masses for any particle unless a spin-0 particle known as Higgs boson is introduced within the SM. Thus the elementary particles acquire their masses through interactions with the Higgs-boson by means of spontaneous breakdown of the electro-weak symmetry which is commonly referred to as the 'Brout-Englert-Higgs mechanism'. The SM contains quarks, namely the up (u), down (d), strange (s), charm (c), bottom (b), and top (t) and leptons, namely electron (e^-), muon (μ^-), tau (τ^-), neutrinos corresponding to each leptons, and their antiparticles in addition to photons (γ), three gauge bosons $W^\pm$ and Z^0, eight gluons g_a, corresponding to the electromagnetic, weak and strong interactions, respectively, and the Higgs field. The SM has been extensively tested in high energy experiments and until the end of the previous century all the particles predicted by the SM except the Higgs bosons were successfully discovered in addition to accurately measuring the strengths of each of the fundamental interactions involved in it. The Higgs boson was ultimately discovered in the year 2012 at the Large Hadron Collider [1] having a mass of about 125 GeV. The discovery of the Higgs boson having a finite mass has opened an interesting challenge of thinking further about the SM – the reason lies in expecting an arbitrarily large Higgs mass which could weigh as high as the Planck mass, $M_P \simeq 10^{19}$ GeV due to quantum corrections. This means one needs to fine-tune the Higgs mass by a factor of m_h/M_P upto 17 decimal places or so in order to obtain the experimentally measured value of the Higgs mass which is quite unnatural. This problem is known as the Naturalness or Hierarchy problem of the SM. This outstanding issue together with other shortcomings of the SM, for instance, the ability of explaining masses of neutrinos, the existence of (cold) dark matter of the Universe, incorporation of gravity, the grand unification of the interactions and matter-antimatter asymmetry of the Universe therefore seem to need a theory that extends beyond the SM.

2 Supersymmetry

One of the SM extensions is supersymmetry (SUSY), which introduces symmetry among bosons and fermions.

$$Fermions \Longleftrightarrow Bosons \tag{1}$$

The charge transforms as spinor and can able to modify spin by half a unit, denoting a supersymmetry charge by Q_α as

$$Q_\alpha|J\rangle = |J \pm 1/2\rangle. \tag{2}$$

This connects bosons of integer spin with fermions of half-integer spin and vice-versa. Here, Q_α is a symmetry operator hence commutes with the Hamiltonian of the system, hence

$$[Q_\alpha, H] = 0, \tag{3}$$

and therefore their anticommutator of two different components has to commute with the Hamiltonian of the system *i.e.* the time translations generator as

$$[\{Q_\alpha, Q_\beta\}, H] = 0. \tag{4}$$

As pointed out above, due to its symmetry, the anticommutator has three independent components, it must transform as a spin-1 object, (analogous to symmetrical combinations of two 1/2 spin wave functions). But in a relativistic theory, this spin-1 object should be expressed with a 4-vector and have conserved from the above anti-commutation relation. So, there would be one such conserved 4-vector operator *i.e.* P_μ. Then the Q_α's satisfy the below relation as

$$\{Q_\alpha, Q_\beta\} \sim P_\mu. \tag{5}$$

Eq. 5 maintained the essence of the matter while the two SUSY transformations generated by the Q's one

after the other, achieve the energy-momentum operator or the space-time translation operator, *i.e.* a derivative. The space-time coordinates are expanded to contain other degrees of freedom and these degrees of freedom are fermionic. Thus, one can say that SUSY invites us to consider the 'fermionic dimensions' to extend space-time to 'superspace' [3].

In its minimal version of SUSY, each SM particle has its supersymmetric partner. This means that each fermionic SM particle has its supersymmetric partner *i.e.* boson or each bosonic SM particle has its fermionic supersymmetric partner. SM particle and its counterpart constitute a 'supermultiplet' and each 'supermultiplet' has an equal number of bosonic and fermionic degrees of freedom. Supersymmetric partners and their SM counterparts both contain the same internal quantum numbers but differ in spin by a half-integer. The model represents the minimal supersymmetric extension of the SM, the Minimal Supersymmetric Standard Model (MSSM), which contains 100 free parameters. The scalar or boson superpartners of the quarks and leptons are named scalar quarks (squarks) and scalar leptons (sleptons), respectively. Generally, "s" is prepended for the superpartner of fermion, *e.g.* selectron ($\tilde{e}$) is the bosonic superpartner of electron (e) whereas "ino" is added for the fermionic superpartner of the gauge bosons, *e.g.* Higgsino is the fermionic superpartner of Higgs. For example, each gauge supermultiplet consists of a gauge boson and its superpartner. Superpartners for gluons (g), W, and B bosons are the gluinos ($\tilde{g}$), winos ($\tilde{W}$), and binos ($\tilde{B}$), respectively. While chiral supermultiplet consists of fermion and its bosonic superpartner. If SUSY is exact then masses of supersymmetric partners and their SM counterparts would be the same. But till now no supersymmetric partners have been discovered, so they should be heavier than their SM counterparts. This implies that SUSY must be broken. Thus SUSY breaking cannot happen within the MSSM itself, but needs an extra "hidden sector" which interacts with the visible sector (MSSM) solely through the exchange of particles called "messengers". The most general superpotential related to MSSM can be written as

$$W = \sum_{i,j=gen} -Y^u_{ij}\,\hat{u}_{Ri}\hat{H}_2\cdot\hat{Q}_j + Y^d_{ij}\,\hat{d}_{Ri}\hat{H}_1\cdot\hat{Q}_j + Y^\ell_{ij}\,\hat{\ell}_{Ri}\hat{H}_1\cdot\hat{L}_j + \mu\hat{H}_2\cdot\hat{H}_1 \quad (6)$$

where the product reads $H\cdot Q \equiv \epsilon_{ab}H^aQ^b$ while $\epsilon_{12} = 1 = -\epsilon_{21}$, and $Y^{u,d,\ell}_{ij}$ denote the Yukawa couplings among generations. The first three terms are the Yukawa interaction related to quarks and charged leptons in the SM, whereas the last term is the only dimensionful term and for the mass of the supersymmetric partner of Higgs boson *i.e.* Higgsino where H_1 and H_2 are two Higgs doublets instead of one Higgs doublet in SM for providing masses to the up and down type fermions, respectively. The Higgs sector consists of five Higgses, namely two CP-even, one CP-odd, and two charged Higgs bosons. The CP-even lightest Higgs boson which is SM-like is bounded to be less than the mass of the Z-boson at the tree level. But it can achieve a 125 GeV Higgs mass due to radiative corrections. Moreover, the two neutral higgsinos mix with the two neutral gauginos to form four neutralinos while the charged higgsinos mix with the charged gauginos to form two charginos. The lightest neutralino is generally assumed as the lightest supersymmetric particle and is considered a candidate for dark matter. Till now no direct evidence for supersymmetric particles has been found, but the ATLAS and CMS experiments [1] have imposed a lower limit on the masses of scalar top and gluinos to be about a TeV scale [2, 3].

3 Supersymmetry breaking

The three most extensively studied mechanisms for soft supersymmetry breaking are

- **Gravity-mediated supersymmetry breaking**
  Gravity-mediated supersymmetry breaking is a way of transmitting supersymmetry breaking to the supersymmetric SM via gravitational interactions. Supersymmetry breaks in this hidden sector and the gravitino which is a supersymmetric version of the graviton obtain a mass through the Higgs mechanism. mSUGRA denotes minimal supergravity and considers the practical model. This mSUGRA model needs four free parameters with a sign to describe the low energy scale from the GUT scale [3].

- **Gauge-mediated supersymmetry breaking (GMSB)**
  It is a way of communicating supersymmetry breaking via the SM's gauge interactions where a hidden sector breaks supersymmetry and interacts with massive messenger fields which are charged according to SM. This produces a gaugino mass at one loop and is then transmitted to its scalar superpartners at two loops [3].

- **Anomaly-mediated supersymmetry breaking (AMSB)**
  Anomaly-mediated supersymmetry breaking is a special kind of gravity-mediated supersymmetry breaking which leads to supersymmetry breaking being passed on to the supersymmetric SM via a conformal anomaly. The maximum Higgs boson that can be acquired is upto 121.0 GeV for the top squarks below 2 TeV. It needs above 2 TeV

top squarks mass for the Higgs boson of mass 125 GeV [3].

4 Features of SUSY

- **Hierarchy problem**
  The radiative corrections to the Higgs boson mass particularly the top quark loop become so huge upto the Plank scale. In order to have a light Higgs boson of 125 GeV for which the SM needs fine-tuning of 30 orders of magnitude. This problem is known as the Naturalness problem. In SUSY, the radiative correction to the Higgs boson includes fermion and its superpartner contributing with opposite signs canceling the quadratic divergence (30 orders of magnitude) and leaving with logarithmic dependence [2, 3].

  Following the radiative correction to the mass of the SM Higgs boson, one gets the quadratic divergences in the cut-off scale on which the theory ceases to be valid and a new physics should come to light. To summarise the issue, let's look at the one-loop correction to the Higgs mass, Higgs particle interact with a loop containing fermion f of mass m_f with Yukawa coupling $\lambda_f = \sqrt{2}m_f/v$. Fig.1 shows the Feynman diagram in which the external incoming and outgoing lines represent Higgs particle that interacts at the vertex with fermionic loop having interaction term λ_f while the internal lines connected to the vertices representing the virtual intermediate particles *i.e.* fermions. For the sake of simplicity, the fermion is very heavy so one can ignore the Higgs momentum and one can attain the quadratically divergent Higgs mass squared ΔM_H^2 proportional to Λ^2,

$$\Delta M_H^2 \sim N_f \frac{\lambda_f^2}{8\pi^2}\Big[-\Lambda^2 + 6m_f^2 \log\frac{\Lambda}{m_f}\Big] \quad (7)$$

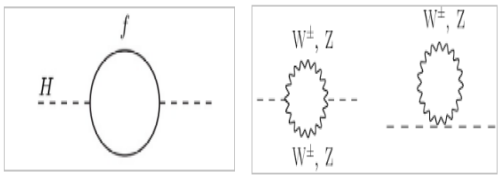

Fig. 1: *Feynman diagrams for fermion and scalar contributions to the mass of the Higgs boson.*

If the cut-off scale Λ is to be 10^{16} GeV (GUT scale) then the Higgs boson mass lies at a very high scale but is supposed to have around the electroweak symmetry breaking scale (∼250 GeV). We require a counterpart to cancel the quadratic divergence of squared Higgs mass in order to have a relatively light Higgs mass. This is termed a Hierarchy or Naturalness problem, where $\Lambda \gg M_Z$. Now we consider the N_S scalar particles (*i.e.* gauge bosons W and Z) with mass m_S in a loop interacting at the vertex with Higgs particle. Fig.1 shows the Feynman diagrams of Higgs boson in which the external incoming and outgoing lines represent the Higgs particle and the internal line of the virtual boson particle. These diagrams lead to the contribution of Higgs boson mass squared which is given as

$$\Delta M_H^2 \sim \frac{\lambda_S N_S}{16\pi^2}\Big[-\Lambda^2 + 2m_S^2 \log\Big(\frac{\Lambda}{m_S}\Big)\Big] \quad (8)$$

We can see in the above Eq. 8, that quadratic divergences exist in it. Under the assumption that the coupling of Higgs with scalars and fermions are related in such a manner that $\lambda_f^2 = 2m_f^2/v^2 = -\lambda_S$ and the multiplication factor of the scalars is twice that of the fermions, $N_S = 2N_f$. Thus we obtain the corrections to the Higgs boson mass squared from the two diagrams of two scalars and one fermion as

$$\Delta M_H^2 \sim \frac{\lambda_f^2 N_f}{4\pi^2}\Big[(m_f^2 - m_S^2) \log\Big(\frac{\Lambda}{m_S}\Big)\Big] \quad (9)$$

As we can see that the quadratic divergences have vanished from the sum, while the logarithmic divergence remains in it. Hence its contribution is small even when the $\Lambda \sim M_P$ and this logarithmic divergence will also disappear when the two scalars and the fermion have the same mass *i.e.* $m_S = m_f$. In this way, the total Higgs mass squared correction will disappear. This implies that the exact "supersymmetry" enforces no divergences even no logarithm divergences and this supersymmetry helps in protecting the Higgs boson mass. Now the Hierarchy or Naturalness problem has been solved. The overall argument may be to incorporate contributions from other SM particles in radiative corrections to Higgs boson mass by including fermionic partners to the W/Z bosons and Higgs boson and by fitting their couplings to the Higgs boson. In this way, the quadratically divergent corrections to the Higgs boson mass are found to have vanished. When the symmetry is badly broken then the scalar particles acquire higher masses than the masses of fermion and Higgs boson, and the Naturalness problem will recur again as the radiative corrections to the Higgs mass, $\propto (m_f^2 - m_S^2)\log(\Lambda/m_S)$, will grow to a large value. In order to have the Higgs mass of the order of the electroweak symmetry breaking scale, then one should have the mass difference between scalar and fermionic particles to be small.

This would suggest that the scalar particles should have mass no more than the TeV scale [2, 3].

- **Unification of couplings**
  One might predict the unification of the strong force with the electroweak force, where the electromagnetic (EM) and weak forces are the components corresponding to the electroweak force. Thus SUSY contributes additional particles that help in altering the running of the coupling strengths in such a way that strong, EM and weak forces unify in a single point at the high energy scale (GUT scale $\sim 10^{16}$ GeV) [2, 3] as shown in Fig. 2.

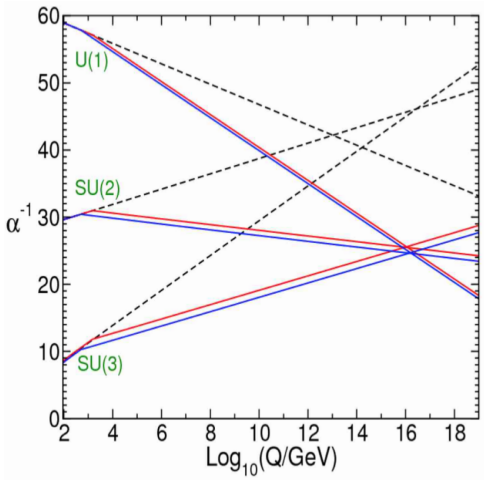

Fig. 2: *Evolution of the inverse gauge couplings for the case of Standard Model (dashed lines) and the Minimal Supersymmetric Standard Model (solid lines) [3].*

- **Gravitation**
  Gravitation is not incorporated in the SM, while it is a fundamental force. If SUSY is applied as a local symmetry then a graviton spin-2 particle will get into it and helps in the mediation of gravitational interaction. The resulting gauge theory from local SUSY is referred to as supergravity. Supergravity is also considered to be the low energy limit for superstring theories, which indicates that it plays a vital role within the context of string theories [3].

- **Neutrino masses**
  The SUSY phenomenon may allow new scales in addition to that of the GUT and these scales open case for the neutrino sector. It can be useful in observing mass hierarchies as well as interesting features like the ultra-small Yukawa couplings. The violation of the low-energy lepton number embedded in SUSY theories can produce the Majorana masses. SUSY can able to explain the light sterile neutrino as well [3].

- **Flavour Changing Neutral Current**
  Flavour Changing Neutral Current (FCNC) processes can serve as a useful signature of SUSY physics at the LHC. There have also been explored the impact of scharm-stop flavour mixing in the top-quark FCNC processes, charged Higgs processes, etc. It is useful in generating radiative corrections on the Higgs mass [4].

- **R-Parity**
  The following superpotential [3] contains terms that violate either lepton (L) or baryon (B) number by odd units. Specifically, the second and the third terms violate the lepton number by one unit while the fourth term violates the baryon number by one unit.

$$W^{extra} = \epsilon_{ab}(-\varepsilon^i \hat{L}_i^a \hat{H}_u^b + \tfrac{1}{2}\lambda_{ijk}\hat{L}_i^a \hat{L}_j^b \hat{e}_k^c + \lambda'_{ijk}\hat{L}_i^a \hat{Q}_j^b \hat{d}_k^c + \tfrac{1}{2}\lambda''_{ijk}\hat{u}_i^c \hat{d}_j^c \hat{d}_k^c).$$

  Due to the terms present in the above superpotential, there exists a new contribution to the proton decay process ($p \to \ell^+\pi^0$ with $\ell^+ = e^+, \mu^+$). Such an approach would allow some unobserved interactions. Some of the SUSY models would allow the B-L violating process and produce a proton of the lifetime $\approx 10^{-9}$ sec considering $\lambda', \lambda'' \sim \mathcal{O}(10^{-1})$ and squark masses of TeV scale. As the experimental limit for the proton decay is greater than 10^{32} years. In order to avoid the proton instability or very fast proton decay, these couplings $(\lambda, \lambda', \lambda'')$ should be extremely small or forbidden from the MSSM superpotential. This process would show the proton instability, so a new symmetry *i.e.* R-parity has been added to restrict this violating process. The R-parity operator would be specified for each particle in the interaction as

$$P_R = (-1)^{L+3B+2s}$$

  where s denotes the spin of the particle. The value of P_R is 1 for SM particles while -1 is for the supersymmetric partners. The combined P_R should be positive for the conservation of R-parity. The consequence of this conservation of R-parity in the SUSY models would be to obtain the most stable and lightest supersymmetric particle (LSP). Consequently, the decay of heavier SUSY particles results in LSP. If the LSP is electrically neutral too then it would contribute as a candidate for dark matter. Several searches for LSP have been conducted, but, no evidence of its existence has been found to date.

- **Dark Matter**
  Since the 1930s, there has been a lot of evidence of dark matter (DM) *i.e.* a non-luminous substance,

that accounts for 25% of the overall energy density of the Universe. The first proof was observed by Fritz Zwicky [5], who examined the movement of galaxies in the Coma cluster where clusters are linked systems of galaxies. Their masses may be computed by means of the Virial theorem which has been able to prove the existence of invisible mass. In 1969, V. Rubin [6] observed the rotation curves of galaxies in which the flatness of rotation curves at a greater distance could not be evident only by the luminous matter. Further, they required a huge amount of non-luminous matter to describe it. Afterward, this non-luminous matter was considered "Dark matter". Other strong hint [8] for the existence of DM is the monitoring of a galaxy cluster known as Bullet cluster (1E0657-558), going into another cluster. Findings in the X-ray range discovered that the hot gas, which forms the majority of the baryonic matter in the two clusters, slows down during the collision. In addition, it was also feasible to map the gravitational potential of clusters following the collision using the gravitational lensing technique. This shows that most of the invisible mass in two clusters passed with no interaction. The accurate measurement of the anisotropies of the cosmic microwave background (CMB) radiation supports the presence of DM. DM interacts via a gravitational force and there are new particles that have weakly interacted with known particles indicating the solution for this DM puzzle. Using CMB anisotropies, the Planck collaboration has precisely observed the relic density of the DM, $\Omega h^2 = 0.120 \pm 0.001$ at 68% C.L. [7]. The most efficient candidate for DM is Weakly Interacting Massive Particle (WIMP), which is consistent with the measured relic abundance of DM [8]. There are three main means of detecting DM which are given as

- **Indirect detection**
  Indirect searches based on the annihilation and the decay of the DM are performed using various satellites and telescopes, namely Fermi-LAT, Planck, PAMELA, AMS, and H.E.S.S. [8].
- **Direct detection**
  Direct searches based on the detection of the scattered DM from the halo on nuclei target on Earth for evaluating mass and coupling of DM with SM. The underground detectors are strongly shielded and estimate the amount of energy deposited by the DM while scattering with the target nuclei (DAMA, LUX, CDMS, CoGeNT, CRESST, PandaX, and XENON1T) [8].
- **Searches in colliders**
  The DM limits are derived from the investigations of monojet, dijet resonances, dileptons, and single photons with missing transverse energy, at LEP and LHC [8].

Neutralinos are potential candidates for DM and are considered to be non-relativistic (Cold DM) during the freeze-out time. They are formed from the superpartner of the mixture of the photon, Z-boson, and neutral Higgs and are electromagnetically neutral so that they will not radiate. Hence it has survived a long time from freeze-out to the present moment. Its annihilation cross section is well consistent with the relic density measured in WMAP [8].

5 LHC Production of SUSY Particles

The energy of the LHC beams turns into mass, producing pairs of heavy SUSY particles. Generally, in the proton-proton collision, highly energetic constituents *i.e.* quarks and gluons collide. The produced sparticles undergo decay into a quark in the form of hadronic jets and a DM particle *i.e.* the lightest neutralino under the assumption of R-Parity to be conserved. The lightest neutralino is stable as well as weakly interacting particle that escapes through the detectors without any interactions carrying the momentum from the collision. At each stage of cascade decay, there is a production of lighter sparticle and SM particle follows the R-Parity conservation rule. The R-Parity conserved lightest SUSY particle is considered a DM candidate and indirectly couples to the protons produced in the collisions [1].

6 Summary

In the current article, with a brief introduction to the SM, we have also explored the need of a Higgs boson in providing masses to the SM fermions and the quanta responsible for their mutual interactions. We have also discussed the Naturalness problem in greater detail at the leading order level associated with the Higgs boson mass. SUSY is one of the most important and attractive concepts for building BSM models since it can solve many of the SM shortcomings as mentioned above. Before concluding the article, we would like to indicate that, since in nature we see no counterparts of SM particles, the supersymmetry must therefore be broken, if it exists. Though by doing a careful analysis, it could be seen that the radiative corrections in the case of broken supersymmetry turn out to be logarithmic, which enables us to explain the recently observed values of the Higgs boson mass at the Large Hadron

Collider. The MSSM provided additional symmetry, known as R-parity, under the conservation of R-parity the stable LSP is considered a DM candidate *i.e.* neutralino. Even with an R-parity violation, a decaying gravitino with a lifetime longer than the age of the Universe is considered a DM candidate. Local SUSY considers the supergravity theory since it also includes gravitational interaction.

References

[1] P. A. Zyla *et al.* [Particle Data Group], Prog. Theor. Exp. Phys. **2020**, no.8, 083C01 (2020).

[2] A. Djouadi, Phys. Rept. **459**, 1-241 (2008), [arXiv:hep-ph/0503173 [hep-ph]].

[3] S. P. Martin, Adv. Ser. Direct. High Energy Phys. **21**, 1-153 (2010), [arXiv:hep-ph/9709356 [hep-ph]].

[4] J. Cao, G. Eilam, K. i. Hikasa and J. M. Yang, Phys. Rev. D **74**, 031701 (2006) [arXiv:hep-ph/0604163 [hep-ph]].

[5] F. Zwicky, Astrophys. J. **86**, 217-246 (1937)

[6] Rubin, V. C., Ford, W. K., Jr, Astrophys. J. **159**, 379 (1970)

[7] N. Aghanim *et al.* [Planck], Astron. Astrophys. **641**, A6 (2020) [erratum: Astron. Astrophys. **652**, C4 (2021)] [arXiv:1807.06209 [astro-ph.CO]].

[8] F. A. Gomes Ferreira, [arXiv:1910.07515 [hep-th]].

Will the Universe End? A Particle Physics Perspective

Najimuddin Khan
Department of Physics, Aligarh Muslim University, Aligarh, UP, India-202002

Abstract

The Universe's fate is a central question in high-energy physics and cosmology, with scalar potentials playing a key role in determining its long-term stability. In the Standard Model, the Higgs potential suggests that the Universe may exist in a metastable minima state. If this is the case, quantum tunneling or thermal fluctuations could trigger a transition to a true minimum state with lower energy, potentially destroying the current Universe. Depending on the presence of new physics, the tunneling time, i.e., the Universe's lifetime, could range from a *few years* to *Infinity*.

1 Introduction

The Standard Model (SM) describes the fundamental forces, excluding gravity, and their interactions with particles through local gauge symmetries: $SU(3)_C$ for the strong force and $SU(2)_L \times U(1)_Y$ for electroweak interactions. The strong force governs quark-gluon interactions, while $W^{\pm}$ and Z bosons and the electromagnetic force by the photon mediate the weak force. The SM comprises six quarks, six leptons, and their corresponding antiparticles. Each quark again has three color charges: red, green, and blue. The SM also includes gauge bosons-$W^{\pm}$ and Z, photon, and gluons-as well as a neutral Higgs field (see Fig. 1). The Higgs boson is unique in the SM, as it is the sole particle responsible for generating the masses of all (except neutrinos) particles.

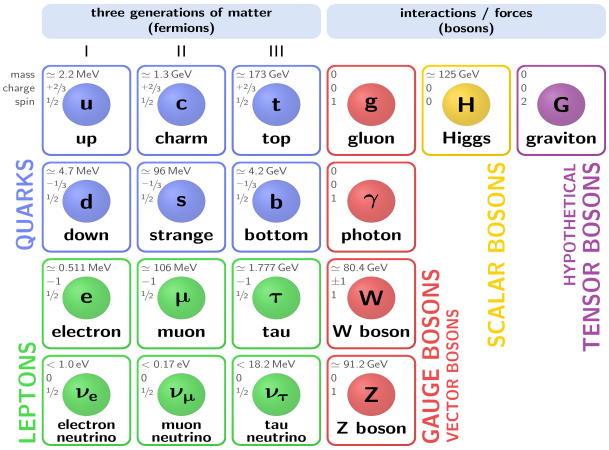

Fig. 1: *Elementary particles of the Standard Model.*

The Massive gauge bosons acquire their masses through their gauge couplings to the Higgs field and the vacuum expectation value (VEV) of the Higgs potential. This interaction part comes from the kinetic part of the scalar Lagrangian. Fermions gain their masses via Yukawa couplings to the Higgs field, combined with the Higgs VEV. We assume that the Higgs boson obtains its mass through its self-quartic coupling. The values of these couplings are critical in shaping the Higgs potential, which determines the stability at the minimum electroweak (low energy) scale. Variations in these parameters can result in different potential minima, including a deeper minimum at high energy scales. It raises the possibility that the current electroweak minimum, where the present Universe resides, may be metastable. In such a case, quantum tunneling or thermal fluctuations could eventually lead to a transition to a deeper true vacuum, posing a theoretical warning about the potential destruction of the Universe.

2 The Higgs discovery and warnings

The discovery of the Higgs boson in 2012 at the Large Hadron Collider (LHC) [1, 2] confirmed the existence of all particles predicted by the SM. Furthermore, the values of all parameters in the SM Lagrangian are now determined at the electroweak scale (246 GeV). We now have the values of the SM parameters at electroweak scale as follows: the Higgs self quartic coupling $\lambda \sim 0.127$ (still need more experimental data to have direct proof), gauge couplings $g_1 \sim 0.36$, $g_2 \sim 0.67$, $g_3 \sim 1.17$ and the Yukawa couplings $(\sqrt{2}Mass/246.2)$ $y_{e,\mu,\tau} \sim \{0.0000028,\ 0.000603,\ 0.0102\}$, $y_{d,s,b} \sim \{0.0000241,\ 0.00055,\ 0.0258\}$ and $y_{u,c,t} = \{0.0000137,\ 0.00706,\ 0.995\}$ [3, 4]. The SM Higgs potential $-\mu^2\,\Phi^\dagger\Phi + \lambda(\Phi^\dagger\Phi)^2$ with $\mu^2 = \lambda v_{SM}^2$, when plotted without the Renormalization effect, exhibits only one minimum at the electroweak energy scale $v_{SM} \sim 246$, and it is generally assumed that our Universe resides in this minimum. However, the parameters of the SM Lagrangian suggest that if the SM remains valid up to the Planck scale $M_{pl} = 10^{19}$

GeV (no new physics in between), a second, deeper minimum exists at a very high energy scale near M_{pl}. The additional deeper minimum arises mainly due to the effect of the Higgs top Yukawa and gauge couplings via running of the Renormalization Group equation [3, 4]. We have shown a similar scalar potential in Fig. 2 considering the Renormalization effect. This deeper minimum indicates that the electroweak minimum, where the Universe currently resides, is metastable. In such a scenario, quantum tunneling or thermal fluctuations could eventually induce a transition to the true vacuum state with lower energy. This transition will create huge energy $\mathcal{O}(10^{64})$ Joules that can burn out everything in the Universe. While this process is extremely unlikely to occur in the near future, it could potentially destroy the current Universe after an incredibly long timescale, estimated to be around 10^{300} years [3, 4].

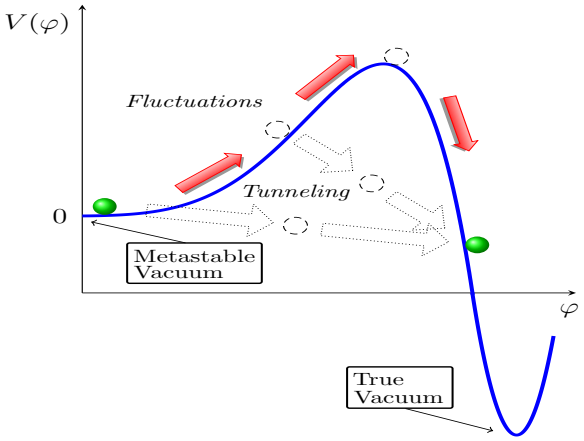

Fig. 2: *Illustration of vacuum decay for potential with a metastable vacuum [5].*

3 Effect of new particles

Several unexplained experimental observations, such as neutrino masses, dark matter, cosmic inflation, and baryogenesis, indicate the need for new physics beyond the SM. The inclusion of additional particles in extensions of the SM can significantly affect the stability of the Higgs potential and the Universe's lifetime. For instance, additional fermions interacting with the Higgs field decrease the Universe's lifetime by destabilizing the electroweak vacuum more. In contrast, the introduction of additional scalar fields coupled to the Higgs can enhance vacuum stability, potentially preventing a transition to a deeper minimum in the Higgs potential. The exact impact of such new physics depends on the nature of these interactions and the parameters of the extended model. Consequently, the predicted lifetime of the Universe could range from a $few\ years$ to $infinity$, depending on the specific details of the new physics framework [6, 7, 8].

In the SM, by construction, the neutrinos are massless as it does not include right-handed neutrinos. But from the neutrino oscillation experiments, we were convinced that at least two neutrinos have non-zero mass. These experiments reveal the mass-squared differences between neutrino eigenstates. The individual masses are still unknown to us. As neutrino masses are tiny compared to other fermion masses, the mechanism behind neutrino mass generation is believed to be different from the other fermions, which obtain mass from the Higgs mechanism. The most popular natural explanation of small neutrino masses is via the see-saw mechanism. There are broadly three classes of such models, namely type-I, type-II, and type-III see-saw models [9]. These models have additional Yukawa coupling with the Higgs, destabilizing the Higgs potential result in threatening the Universe stability [6, 7].

The last few years have seen a revolution in cosmology and astrophysics. It is confirmed that the Universe is filled with dark matter (DM) and even more enigmatic dark energy. Various kinds of astrophysical observations, e.g., anomalies in the galactic rotation curves, gravitational lensing effects in Bullet clusters, etc., have indicated the existence of dark matter in the Universe. Dark matter interacts gravitationally. It has no electric charge, so we cannot observe it through its interactions with photons. The satellite-based experiments such as Wilkinson Microwave Anisotropy Probe (WMAP) [10] and Planck [11] have measured the Cosmic Microwave Background Radiation (CMBR) of the Universe with unprecedented accuracy and suggest that the Universe consists of about 4% ordinary matter, 27% dark matter and the rest 69% is mysterious unknown energy called dark energy which is thought to be the cause of accelerated expansion of the Universe. The SM fails to provide a viable dark matter candidate. To explain the observed presence of the dark matter, new physics beyond the SM is required. Dark matter particles could be new gauge bosons, scalar, and fermion fields. Additional gauge bosons and scalar fields could stabilize the Universe via the additional gauge and scalar quartic couplings. This coupling reduces the dominant effect of Higgs top Yukawa coupling [12, 13]. However, the fermionic dark matter interacting with Higgs may create additional and deeper minima and threaten stability again. Depending on the additional parameters, the Universe could be sustained for a long time or end soon.

It is also studied in various literature that the presence of both fermions and scalar fields could not only explain the unexplained shortcomings of the

SM but also help to calculate the exact lifetime of the Universe [6, 7, 8, 12, 13].

4 Summary

The Standard Model successfully describes nature's fundamental particles and forces but falls short in explaining key phenomena such as neutrino masses, dark matter, and cosmic inflation. The Higgs boson, which plays a central role in providing particle masses, also influences the Universe's stability. Current parameters within the SM indicate that the electroweak vacuum is metastable, meaning it could theoretically undergo a catastrophic vacuum transition through quantum tunneling. However, this process is predicted to occur on a timescale of approximately 10^{300} years. The introduction of new physics beyond the Standard Model can significantly affect vacuum stability. For instance, additional fermions interacting with the Higgs field tend to destabilize the vacuum, whereas the presence of scalar fields and gauge bosons can enhance its stability. While these possibilities remain speculative, it is reassuring that any potential instability is an incredibly distant concern. More work is needed to understand these issues fully, and drawing concrete conclusions will take considerable time. For now, we can take comfort in the fact that the Universe appears stable for the foreseeable future.

References

[1] G. Aad *et al.* [ATLAS], Phys. Lett. B **716**, 1-29 (2012) doi:10.1016/j.physletb.2012.08.020 [arXiv:1207.7214 [hep-ex]].

[2] S. Chatrchyan *et al.* [CMS], Phys. Lett. B **716**, 30-61 (2012) doi:10.1016/j.physletb.2012.08.021 [arXiv:1207.7235 [hep-ex]].

[3] G. Degrassi, S. Di Vita, J. Elias-Miro, J. R. Espinosa, G. F. Giudice, G. Isidori and A. Strumia, JHEP **08**, 098 (2012) doi:10.1007/JHEP08(2012)098 [arXiv:1205.6497 [hep-ph]].

[4] D. Buttazzo, G. Degrassi, P. P. Giardino, G. F. Giudice, F. Sala, A. Salvio and A. Strumia, JHEP **12**, 089 (2013) doi:10.1007/JHEP12(2013)089 [arXiv:1307.3536 [hep-ph]].

[5] T. Markkanen, A. Rajantie and S. Stopyra, Front. Astron. Space Sci. **5**, 40 (2018) doi:10.3389/fspas.2018.00040 [arXiv:1809.06923 [astro-ph.CO]].

[6] I. Garg, S. Goswami, K. N. Vishnudath and N. Khan, Phys. Rev. D **96**, no.5, 055020 (2017) doi:10.1103/PhysRevD.96.055020 [arXiv:1706.08851 [hep-ph]].

[7] S. Goswami, K. N. Vishnudath and N. Khan, Phys. Rev. D **99**, no.7, 075012 (2019) doi:10.1103/PhysRevD.99.075012 [arXiv:1810.11687 [hep-ph]].

[8] N. Khan and S. Rakshit, Phys. Rev. D **90**, no.11, 113008 (2014) doi:10.1103/PhysRevD.90.113008 [arXiv:1407.6015 [hep-ph]].

[9] A. Abada, C. Biggio, F. Bonnet, M. B. Gavela and T. Hambye, JHEP **12**, 061 (2007) doi:10.1088/1126-6708/2007/12/061 [arXiv:0707.4058 [hep-ph]].

[10] C. L. Bennett *et al.* [WMAP], Astrophys. J. Suppl. **208**, 20 (2013) doi:10.1088/0067-0049/208/2/20 [arXiv:1212.5225 [astro-ph.CO]].

[11] P. A. R. Ade *et al.* [Planck], Astron. Astrophys. **571**, A16 (2014) doi:10.1051/0004-6361/201321591 [arXiv:1303.5076 [astro-ph.CO]].

[12] N. Khan and S. Rakshit, Phys. Rev. D **92**, 055006 (2015) doi:10.1103/PhysRevD.92.055006 [arXiv:1503.03085 [hep-ph]].

[13] N. Khan, Eur. Phys. J. C **78**, no.4, 341 (2018) doi:10.1140/epjc/s10052-018-5766-4 [arXiv:1610.03178 [hep-ph]].

Largest Scientific Endeavour on Earth: From LEP to LHC

Mohammed Mohsin Khan
Department of Applied Physics, Aligarh Muslim University, Aligarh, UP, India-202002

The "Lord of the Collider Rings" at the European Center for Nuclear Research (CERN) was the mighty title that was first given to the LEP (Large Electron Positron Collider) by Herwig Schopper. LEP, the largest electron-positron accelerator ever built was dismantled in 2000. Its 27-kilometre tunnel now hosts the LHC (Large Hadron Collider). The LHC is now undisputedly recognized as the largest scientific endeavour on our globe. Sometimes the LEP and its successor in the same tunnel, the LHC are compared to cathederal built in the Middle Ages. They have some aspects in common, such as belonging to the largest objects created by man, requiring an exceptional collective effort, applying the most advanced techniques available at their time and swallowing a large fraction of GNP. Both of these manifested in many respects the spirit of their age, although certainly some people considered them as useless from a practical point of view.

The LHC at CERN is a gigantic scientific instrument spanning across the Swiss-French border near Geneva. This world's largest and most powerful particle accelerator is used by thousands of physicists from the various countries (including India) across the globe to search for particles to unravel the chain of events that shaped our Universe a fraction of a second after the Big Bang. It could resolve puzzles ranging from the properties of the smallest particles to the biggest structures in the vastness of the Universe.

The design and construction of the LHC took about 20 years at a total cost of approximately €3.6 billion. It is housed in a 27 km long and 3.8 m wide tunnel about 100 m beneath the ground. At this level, there is a geologically stable stratum, and the depth prevents any radiation from escaping. Until 2000, the tunnel was the home to the LEP storage ring, which was built in 1989. This earlier accelerator collided electrons with their anti-particles, positrons to study the properties of the resulting particles and their interactions with great precision.

There are eight elevators leading down into the tunnel. To move between the eight access points, maintenance and security people use bicycles to move around the tunnel – sometimes for several kilometres. The LHC is automatically operated from a central control centre, so once the machine is in operation, Physicists, engineers and technicians will only have to access the tunnel for maintenance.

The actual experiment is a rather simple process: the LHC will collide two hadrons, either protons or lead nuclei at speeds close to the speed of light. The very high levels of energy involved will allow the kinetic energy of the colliding particles to be transformed into matter, according to Einstein's law $E = mc^2$. Particles created in the collisions pass through detectors where the measurement of the momenta, emission angles etc. are recorded for physics studies. This experiment repeats up to 600 million times per second and for quite long duration. The LHC is mainly performing proton-proton collisions, which will be studied by three of its four detectors (ATLAS, CMS, and LHCb). However, for several weeks per year, heavy ions (lead nuclei) are being accelerated and collided instead, to be studied mainly by the dedicated ALICE detector. The Physics Department, AMU, Aligarh has also been a part of the ALICE Collaboration since the year 2000.

Like any other particle accelerator, the LHC has three main components: the beam pipes, the accelerating structures, and the magnet system. Inside its two beam pipes, each 6.3 cm in diameter, proton (or heavy ion) beams travel in opposite directions (one direction in each pipe) in an ultra-high vacuum of 10^{-13} bar, comparable to the density of matter in outer space. This low pressure is necessary to minimize the number of collisions with resting gas molecules and the subsequent loss of the accelerated particles.

The protons are supplied from a hydrogen gas bottle. Hydrogen atoms consist of a proton and an electron. Electrons are removed using an electric discharge, after which the protons are guided towards the accelerator through electric and magnetic fields. For

the LHC beam, 300 trillion protons are required, but since a single cubic centimetre of hydrogen gas at room temperature contains about 60 million trillion protons, the LHC can be refilled 200000 times with just one cubic centimetre of gas – and it only needs refilling twice a day!

Every time the particles run through these cavities, they are accelerated by a strong electric field of about 5 MV/m. The functionality of the accelerators is comparable to surf on the sea: a bunch of protons, about 100 billion of them – the surfers – ride together on an enormous electromagnetic wave and gain kinetic energy. Each wave accelerates one bunch of protons, and each of the two beams consists of 2800 discrete bunches, one every seven metres. After 20 minutes, they reach their final energy, while doing 11245 circuits of the LHC ring per second. In those 20 minutes, the protons cover a distance more than that from Earth to the Sun and back.

They enter the LHC at 99.9997828% of the speed of light. After acceleration, they reach 99.9999991%. This is the maximum speed that can be reached, since nothing can move faster than light, according to the theory of relativity. Although it is not a significant gain in speed, at close to the speed of light, even a small acceleration results in a large gain in mass, and this is the important part. A motionless proton has a mass of 0.938 GeV. The accelerators bring them to a final mass (or energy, which in this case is practically the same thing) of 7000 billion electron volts (7 tera-eV or 7 TeV). If you could – hypothetically – accelerate a person of 100 kg in the LHC, his or her mass would end up being 700 t.

Without external forces, the protons would fly in a straight line. To give them a circular trajectory, the pipes are surrounded by a large magnet system that deflects the protons' path – these magnets are the third part of every particle accelerator. The larger the mass of a particle, the stronger the magnets needed to keep it on track. This is where the limitations of a particle accelerator lie, since at a certain magnetic energy, the material of the magnetic coils cannot resist the forces of its own magnetic field anymore. The magnets used in the LHC have been specially designed: the dominant part of the magnet system consists of 1232 dipole magnets, each with a length of about 16 m and a weight of 35 t, which create a maximum magnetic field of 8.33 tesla – 150 000 stronger than Earth's magnetic field.

The magnets have a special two-in-one design: they contain two magnet coils on the inside, each surrounding one of the two beam pipes. The current runs through the coils to create two magnetic fields, pointing downwards in one pipe and upwards in the other. This is how two particles (protons or lead nuclei) of the same charge can follow the same track in opposite directions – one in each beam pipe.

In addition to the dipole magnets, there are quadrupole magnets (with four magnetic poles) for focusing the beams, and thousands of additional smaller sextupole and octupole magnets (with six or eight magnetic poles each, respectively) for correcting the beam size and position.

All magnet coils and the accelerator cavities are built from special materials (niobium and titanium) that become superconducting at very low temperatures, conducting electricity to produce the electric and magnetic fields without resistance. To reach their maximum performance, the magnets need to be chilled to -271.3°C (1.9K) – a temperature colder than outer space. To cool the magnets, the accelerator is connected to a distribution system of liquid nitrogen and helium. Just one-eighth of the LHC's cryogenic distribution system would qualify as the world's largest fridge.

Around the ring there are four points at which the chain of magnets is broken: they contain the four huge caverns for the LHC experiments and their detectors. Here, the trajectories of the inner and outer beams are made to cross each other and swap places in special X-shaped beam pipes. In all four X-shaped pipes, the beams cross at an angle of 1.5 degrees, allowing the beams to be brought into collision.

To increase the probability of particle collisions, the bunches of particles are squeezed, by special magnets just in front of each collision chamber, to a diameter of 16 μm – thinner than a human hair – and 80 mm in length. The beams are so tiny that the task of making them collide is akin to firing needles from two positions 10 km apart with such precision that they meet halfway! However, the LHC technology manages this intricate task. Nonetheless, even in these focused beams of particles, the density is still very low – 100 million times lower than that of water – so most of the particles pass straight through the other bunch of particles without colliding or even slowing down. Thus, although there are 100 billion protons in each bunch, when two bunches collide, only about 20 particle collisions occur. Since collisions between two bunches occur 31 million times per second (2800 bunches $\times$ 11 245 turns of the LHC ring per second), this still gives about 600 million proton collisions per second when the LHC is operating at maximum intensity.

A single bunch of protons travelling at full speed has the same kinetic energy as a one-tonne elephant

running at 50 km/h, and the entire energy contained in the beam is 315 megajoules (MJ), enough to melt nearly 500 kg of copper. Therefore, considerable efforts have gone into the security of the LHC. Should the beam become unstable, this will be immediately detected by the beam sensors, and within the next three laps around the ring (i.e. in less than a thousandth of a second) the beam will be deflected into a kind of emergency exit, where it is absorbed by graphite plates and concrete before it can cause any further damage.

At LHC two protons will collide with a total kinetic energy of $7 + 7 = 14$ TeV (or two lead ions at a total energy of 1140 TeV). The particles created are detected and measurements are performed for physics studies.

According to quantum physics, these collisions will generate all particles of the standard model with certain probabilities. However, the probability of generating the heavy particles that scientists are actually looking for is very low. Few of the particle collisions will be hard enough to produce new, heavy particles. Theory predicts that Higgs bosons (to learn more about the Higgs boson, or other completely new phenomena that are being searched for will be produced only very rarely (typically once in 10^{12} collisions), so it is necessary to study many collisions in order to find the 'needle in a million haystacks'. That is why the LHC will be run for many years, 24 hours a day.

The events (an event is a collision with all its resulting particles) are studied using giant detectors that are able to reconstruct what happened during the collisions – and to keep up with the enormous collision rates. Detectors can be compared to huge three-dimensional digital cameras that can take up to 40 million snapshots (with digitised information from tens of millions of sensors) per second. The detectors are built in layers, and each layer has a different functionality. The inner ones are the least dense, while the outer ones are denser and more compact.

The heavy particles that scientists hope to be produced in the LHC collisions are predicted to be very short-lived, rapidly decaying into lighter, known particles. After a hard collision, hundreds of these lighter particles, for example electrons, muons and photons, but also protons, neutrons and others, fly to the detector where these are recorded. Study of the characteristics of these particles establishes production of heavy flavours.

The trajectories of charged particle are bent by magnetic fields, and their radius of curvature is used to calculate their momenta: the higher the kinetic energy, the shallower the curvature. For particles with high kinetic energy, therefore, a sufficiently long trajectory must be measured in order to accurately determine the curvature radius. Other important parts of a detector are calorimeters for measuring the energy of particles (both charged and uncharged). The calorimeters too have to be large enough to absorb as much particle energy as possible. These are the two principle reasons why the LHC detectors are so large.

The detectors are built to hermetically enclose the interaction region in order to account for the total energy and momentum balance of each event and to reconstruct it in detail. Combining the information from the different layers of the detector, it is possible to determine the type of particle which has left each trace.

Charged particles – electrons, protons and muons – leave traces through ionisation. Electrons are very light and therefore lose their energy quickly, while protons penetrate further through the layers of the detector. Photons themselves leave no trace, but in the calorimeters, each photon converts into one electron and one positron, the energies of which are then measured. The energy of neutrons is measured indirectly: neutrons transfer their energy to protons, and these protons are then detected. Muons are the only particles that reach (and are detected by) the outermost layers of the detector.

Each part of a detector is connected to an electronic readout system via thousands of cables. As soon as an impulse is registered, the system records the exact place and time and sends the information to a computer. Several hundred computers work together to combine the information. At the top of the computer hierarchy is a very fast system which decides – in a split second – whether an event is interesting or not. There are many different criteria to select potentially significant events, which is how the enormous data of 600 million events is reduced to a few hundred events per second that are investigated in detail.

The LHC detectors were designed, constructed and commissioned by international collaborations, bringing together scientists from institutes all over the world. In total, there are four large (ATLAS, CMS, LHCb and ALICE) and two small (TOTEM, LHCf) experiments at the LHC. Considering that it took 20 years to plan and construct the detectors, and they are intended to run for more than 10 years, the total duration of the experiments is almost equivalent to the entire career of a physicist.

The construction of these detectors is the result of what could be called a 'group intelligence': while the scientists working on a detector understand the function of the apparatus in general, no one scientist is familiar with the details and precise function of each single part. In such a collaboration, every scientist contributes with his or her expertise to the overall success.

The two largest experiments, ATLAS (A Toroidal LHC ApparatuS) and CMS (Compact Muon Solenoid), are general-purpose detectors optimised for the search for new particles. ATLAS and CMS are located on opposite sides of the LHC ring, 9 km apart. Having two independently designed detectors is vital for cross-confirmation of any new discoveries.

The ATLAS and the CMS collaborations each consist of more than 2000 physicists from 35 countries. The ATLAS detector has the shape of a cylinder 25 m in diameter and 45 m in length, about half as big as Notre Dame Cathedral in Paris, France, and weighing the same as the Eiffel Tower (7000 t). Its magnetic field is produced by a solenoid in the inner part and an enormous doughnut-shaped toroid magnet further outside.

The CMS detector also has a cylindrical shape (15 m in diameter and 21 m in length) and is built around a superconducting solenoid magnet generating a field of 4 tesla, which is confined by a steel yoke that forms the bulk of the detector's weight of 12500 t. While ATLAS was constructed in situ, the CMS detector was constructed at the surface, lowered underground in 15 sections and then assembled.

The LHCb experiment will help us to understand why we live in a universe that appears to be composed almost entirely of matter but no antimatter. It specialises in investigating the slight differences between matter and antimatter by studying a type of particle called the bottom quark, or b quark. To identify and measure the b quarks and their antimatter counterparts, the anti-b quarks, LHCb has sophisticated movable tracking detectors close to the path of the beams circling in the LHC. ALICE (A Large Ion Collider Experiment) is a specialised detector for analysing the collisions of lead ions. For a few weeks each year these, rather than protons, will be collided in the LHC. Within the dimensions of an atomic nucleus, this will create conditions that prevailed about a millionth of a second after the Big Bang, when the temperature of the entire Universe was about 100000 times hotter than the interior of the Sun. These conditions might create a state of matter called a quark-gluon plasma, the characteristics of which physicists hope to study.

The LHC produces roughly 15 petabytes (15 million gigabytes) of data annually – enough to fill more than 3 million DVDs. Thousands of scientists around the world want to access and analyse these data, so CERN is collaborating with institutions in 33 countries to operate a distributed computing and data storage infrastructure: the LHC Computing Grid (LCG).The LCG will allow data from the LHC experiments to be distributed around the globe, with a primary backup kept at CERN. After initial processing, the data will be distributed to eleven large computer centres. These tier-1 centres will make the data available to more than 120 tier-2 centres for specific analysis tasks. Individual scientists can then access the LHC data from their home country, using local computer clusters or even individual PCs.

References

[1] The LHC, a look inside, Landua R, Rau M (2008) The LHC: a step closer to the Big Bang. Science in School 10: 26-33.

[2] The Making, Operation and Legacy of the World's Largest Scientific Instrument, Herwig Schopper

[3] http://education.web.cern.ch/education/Chapter2/Intro.html

Exploring the Universe with AMS-02: A Window to Cosmic Mysteries

Meeran Zuberi *
AMS Experiment, CERN, Geneva, Switzerland

The Alpha Magnetic Spectrometer (AMS-02) is a state-of-the-art particle physics detector installed on the International Space Station (ISS) to study cosmic rays and the fundamental nature of the universe. Designed to identify antimatter, dark matter, and measure cosmic ray composition, AMS- 02 provides unprecedented precision in particle detection from space. Since its deployment in 2011, it has revolutionized our understanding of high-energy phenomena, contributing to questions about the origins of the universe, the nature of dark matter, and the prevalence of antimatter. AMS-02 continues to shape modern astrophysics, bridging the gap between particle physics and cosmology through innovative space-based research.

The Alpha Magnetic Spectrometer-02 (AMS-02) is a state-of-the-art particle physics detector mounted on the International Space Station (ISS). Its primary mission is to study cosmic rays to gain insights into the universe's fundamental structure and origin. By analyzing high-energy particles from space, AMS-02 seeks to detect evidence of dark matter, antimatter, and other phenomena that could shed light on the composition of the cosmos.

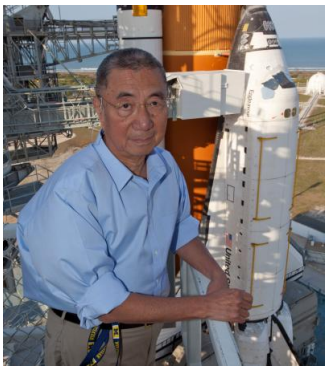

Samuel C. C. Ting, the principle investigator of the AMS-02 experiment.

The concept for AMS-02 was proposed by Nobel laureate physicist Samuel C. C. Ting in the mid-1990s. The project is a collaborative effort involving 56 institutions from 16 countries, highlighting its global significance. A prototype, AMS-01, was tested aboard the Space Shuttle Discovery during the STS-91 mission in 1998. Following this successful demonstration, AMS-02 was developed for long-term operation on the ISS. It was launched aboard the Space Shuttle Endeavour on May 16, 2011, during the STS-134 mission and was installed on the ISS on May 19, 2011.

AMS-02 is designed to address several key questions in modern physics:

Search for Antimatter: One of the experiment's primary goals is to search for primordial antimatter by detecting antihelium nuclei. The presence of such particles would suggest the existence of large amounts of antimatter in the universe, providing insights into the matter-antimatter asymmetry observed today.
Dark Matter Detection: AMS-02 analyzes cosmic ray particles to identify anomalies that could indicate interactions involving dark matter particles. By studying the flux of positrons and electrons, the experiment aims to detect signatures consistent with dark matter annihilation or decay.
Study of Cosmic Ray Propagation: The detector measures the composition and energy spectra of cosmic rays, including protons, nuclei, and electrons.

*Ph.D., Aligarh Muslim University, Aligarh.
PDF with Samuel C. C. Ting (Nobel Laureate), CERN, Geneva.

These measurements help scientists understand the propagation mechanisms of cosmic rays through the galaxy and provide information on their sources and acceleration processes.

AMS-02 comprises several sophisticated subsystems that work together to identify and measure particles with high precision:

- **Magnet:** A permanent magnet creates a magnetic field that bends the trajectories of charged particles, allowing the determination of their charge and momentum.
- **Silicon Tracker:** This component measures the curvature of particle tracks within the magnetic field, providing precise momentum and charge sign information.
- **Transition Radiation Detector (TRD):** The TRD distinguishes between light particles, such as electrons and positrons, and heavier protons by detecting transition radiation emitted as particles traverse materials at relativistic speeds.
- **Time of Flight (TOF) System:** The TOF system measures the time it takes for particles to traverse a known distance, aiding in velocity determination and particle identification.
- **Ring Imaging Cherenkov Detector (RICH):** The RICH measures the velocity of charged particles by detecting Cherenkov radiation, which, combined with momentum information, allows for mass determination.
- **Electromagnetic Calorimeter (ECAL):** The ECAL measures the energy of electrons, positrons, and photons by absorbing the entire energy of the particle, providing a complete energy measurement.

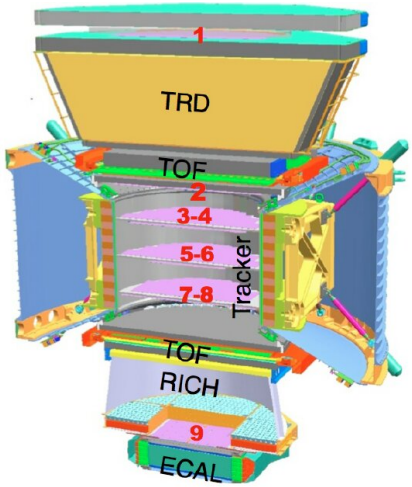

A schematic diagram of the AMS-02 detector, illustrating its various components.

One of the most significant results from AMS-02 is the precise measurement of the positron fraction in cosmic rays, spanning a wide energy range. This measurement revealed an unexpected excess of positrons at high energies, sparking discussions about their origin. The observed anomaly has been linked to possible contributions from dark matter annihilation, pulsars, or other astrophysical phenomena, making it a focal point for theoretical and experimental investigations.

AMS-02 has also provided detailed measurements of the fluxes of various nuclei, such as protons, helium, and heavier elements like carbon and iron. These data have improved our understanding of cosmic ray propagation in the galaxy and the processes involved in their acceleration and interactions with interstellar matter. Additionally, AMS-02 has been instrumental in distinguishing between primary cosmic rays, which originate from astrophysical sources, and secondary cosmic rays, which result from interactions of primary rays with interstellar material.

Another groundbreaking result is the precise measurement of cosmic ray anti-protons. These data have constrained models of dark matter and cosmic ray production, as any significant contribution from dark matter annihilation would manifest as deviations in the anti-proton spectrum. AMS-02 has achieved the most sensitive search to date for primordial anti-helium, a potential signature of antimatter in the universe, though none has been detected so far.

A recent AMS-02 result highlights an intriguing excess in the detection of cosmic rays composed of deuterons—atomic nuclei consisting of a proton and a neutron. Deuterons are believed to form similarly to helium-3 nuclei through collisions between primary helium-4 nuclei and other nuclei in the interstellar medium. If this hypothesis holds, the deuteron-to-helium-4 flux ratio would closely resemble the helium-3-to-helium-4 flux ratio.

However, AMS-02 observations show a significant disparity in these ratios above a rigidity of 4.5 gigavolts (GV). Unlike the helium-3-to-helium-4 ratio, which decreases more steeply with increasing rigidity, the deuteron-to-helium-4 ratio declines more gradually. Even more unexpectedly, above 13 GV, the AMS-02 data indicate that the deuteron flux is nearly identical to the proton flux, characteristic of primary cosmic rays. To put it simply, AMS has found more deuterons than expected from collisions between primary helium-4 nuclei and the interstellar medium.

"Measurement of deuterons is quite difficult because of the large cosmic proton background," says AMS spokesperson Samuel Ting. ***"Our unexpected results continue to show how little we know about cosmic rays. With the coming upgrade of AMS to increase its acceptance by 300%, AMS will be able to measure all the charged cosmic rays to one percent accuracy and provide an experimental basis for the development of an accurate cosmic-ray theory."***

AMS-02 stands as a groundbreaking instrument in exploring cosmic mysteries, from the nature of dark matter to the universe's composition. Its achievements continue to advance our understanding of cosmic rays and the fundamental questions of physics.

Exploring Unusual Measurements of Neutron Stars: HESS J1731-347, XTE J1814-338, and Beyond

Ishfaq Ahmad Rather[1] *and Anisul Ain Usmani*[2]
[1]*Institute for Theoretical Physics, Goethe University, Max-von-Laue-Str. 1, D-60438 Frankfurt am Main, Germany*
[2]*Department of Physics, Aligarh Muslim University, Aligarh, UP, India-202002*

1 Introduction

Neutron stars (NSs) are extraordinary cosmic laboratories that allow us to probe the fundamental properties of matter under intense gravitational and magnetic fields, extreme densities, isospin asymmetry, and high temperatures. They embody a fascinating interplay between nuclear processes and astrophysical observables. Studying NSs integrates expertise from disciplines such as general relativity (GR), high-energy physics, nuclear physics, and quantum chromodynamics (QCD). With masses exceeding the Sun's compressed into a sphere of 10 km radius, NSs offer unparalleled access to the phase diagram of matter at extreme conditions, shaping our understanding of diverse astrophysical phenomena.

Significant theoretical and observational advances have deepened our understanding of NSs. Observations from X-ray and gamma-ray observatories, as well as gravitational wave detections from events like GW170817, GW190814, and GW230529 [1, 2, 3], have unveiled new insights into NS structures and equations of state (EoS). These findings indicate that EoS must be sufficiently stiff at high densities to support NSs with masses above $2M_\odot$, as confirmed by precise mass measurements of pulsars like PSR J1614-2230 ($M = 1.97 \pm 0.04\, M_\odot$) [4], PSR J0348+0432 ($M = 2.01 \pm 0.04\, M_\odot$) [5], and PSR J0740+6620 ($M = 2.08 \pm 0.07\, M_\odot$) [6].

The measurement of NS radii from various observations, including Neutron Star Interior Composition Explorer (NICER), X-ray Multi-Mirror (XMM), and gravitational-wave detectors like Laser Interferometer Gravitational-Wave Observatory (LIGO) and Variability of Irradiance and Gravity Oscillations (VIRGO), has significantly constrained the EoS of dense matter. Recent NICER observations of the high-mass pulsar PSR J0740+6620, complemented by XMM-Newton data, have updated the radius estimates to $R = 12.49^{+1.28}_{-0.88}$ km and $R = 12.76^{+1.49}_{-1.02}$ km [7] which also cover the earlier measurements of $R = 12.39^{+1.30}_{-0.98}$ km and $R = 13.71^{+2.61}_{-1.50}$ km [8, 9]. For the millisecond pulsar PSR J0030+0451, radii were measured to be $R = 13.02^{+1.24}_{-1.06}$ km [10] and $R = 12.71^{+1.14}_{-1.19}$ km [11].

These measurements imply that the EoS must remain sufficiently stiff at high densities to prevent gravitational collapse under such extreme conditions. Models that fail to achieve this maximum mass threshold are incompatible with observational data, emphasizing the need for a delicate balance between stiffness at high densities and compliance with lower-density constraints, such as those derived from radius and tidal deformability measurements. This implies that for a given model, the EoS should be compatible with the chiral effective field theory constraints at very low density, satisfy the radius and tidal deformability constraints at the intermediate densities, and also meet the $2\, M_\odot$ at high density.

The measurements of HESS J1731-347 and XTE J1814-338 have introduced compelling challenges to our understanding of neutron star (NS) structure and the equation of state (EoS) governing ultra-dense matter. These objects, with their distinct properties, stand apart from typical neutron star measurements and demand novel theoretical insights to reconcile their characteristics with established models.

1.1 HESS J1731-347: A Low-Mass, Compact Star

HESS J1731-347 is an exceptionally low-mass neutron star, with a mass of $M = 0.77^{+0.20}_{-0.17}\, M_\odot$ and a radius of $R = 10.4^{+0.86}_{-0.78}$ km [12]. Such low-mass NSs are rare and present significant challenges to EoS models, as they require an explanation for how matter remains stable at densities substantially lower than those typically observed in more massive neutron stars.

This measurement is particularly intriguing when compared with the canonical $1.4\, M_\odot$ NSs observed in events like GW170817. Models of dense matter must address the stability and structure of stars at lower masses, where gravitational forces are weaker but still sufficient to compress matter to densities exceeding that of nuclear matter. The compactness of HESS J1731-347 suggests that it may exhibit an unusual internal structure, such as exotic phases of matter (e.g., hyperons, deconfined quarks, or Bose-Einstein condensates) or interactions dominated by non-standard nuclear forces.

1.2 XTE J1814-338: An Extremely Small Radius

XTE J1814-338, on the other hand, is notable for its unusually small radius, $R = 7.0\,\mathrm{km}$, coupled with a mass of $M = 1.21\,M_\odot$ [13]. This combination yields an exceptionally high compactness ratio, which challenges the stiffness of most standard EoS models. Such a compact radius for a relatively low mass implies an EoS that is much softer at intermediate densities than what is typically inferred from observations of higher-mass neutron stars.

In contrast to GW170817, which provides constraints on tidal deformability and supports a radius range of approximately 11.9–13.6 km for $1.4\,M_\odot$ neutron stars, XTE J1814-338 falls significantly below this range. This suggests that models accommodating such small radii must reconcile the behavior of dense matter across a wide range of densities, from soft EoS at low masses to stiff EoS capable of supporting $2\,M_\odot$ stars like PSR J0740+6620.

The existence of such outliers as HESS J1731-347 and XTE J1814-338 presents several challenges. One being that the models must exhibit an extraordinary degree of flexibility to simultaneously describe soft and stiff matter behavior, as required by low-mass and high-mass neutron stars, respectively.

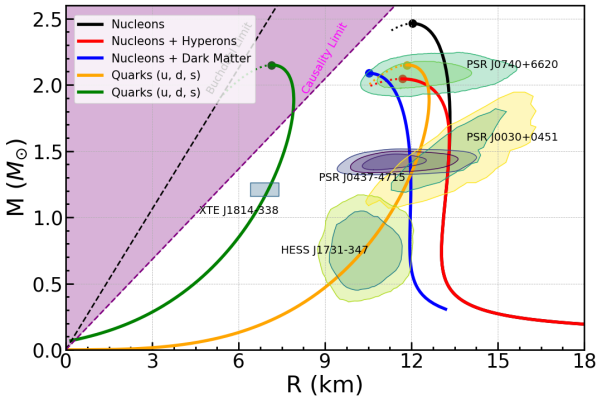

Fig. 1: *Mass-Radius relation for EoS with different compositions: Nucleons only (black), Nucleons with Hyperons (red), Nucleons with Dark matter admixed (blue), Strange matter (orange and green) at two different parameter values. The magenta and black dashed lines correspond to the causality limit and Buchdahl limit, respectively. The various shaded areas are credibility regions for mass and radius inferred from the analysis of PSR J0740+6620, PSR J0030+0451, PSR J0437-4715, HESS J1731-347, and XTE J1814-338 [9, 14, 10, 11, 15, 12, 13].*

Figure 1 shows the mass-radius (MR) relationship for the different interior compositions of an NS, obtained by solving the Tolmann-Oppenheimer-Volkoff (TOV) equations. The black line represents the EoS from a Density-Dependent Relativistic Mean-field (DD-RMF) model with nucleons only. In this model, the interaction is described considering nucleons (and other hadrons) interacting through the exchange of virtual mesons. The red line corresponds to the DD-RMF model with nucleons and hyperons, that soften the EoS and hence lower the maximum mass [16]. The blue line represents the nucleons with Dark Matter (DM) in the RMF model [17]. The orange and green curves represent the Strange stars (stars made of pure quark matter: u, d, s) at two different parameter values of the vector interaction enhanced bag (vBag) model which is a free Fermi gas model with repulsive vector interaction [18]. The magenta and black dashed lines correspond to the causality limit ($C = M/R$ = 0.354 where the speed of sound squared c_s^2 = 1) and the Buchdahl limit (C = 0.49), respectively. Any MR relation in these two regions is ruled out. The various shaded areas are credibility regions for mass and radius inferred from the analysis of PSR J0740+6620, PSR J0030+0451, PSR J0437-4715, HESS J1731-347, and XTE J1814-338.

We see that all the MR curves satisfy the $2M_\odot$ limit and the radius constraints. For the orange curve, it starts from the origin as it is a strange star which are self-bound,compared to the hadronic stars, which are gravity-bound, it satisfies the HESS J1731-347 constraint also. For the green curve, although it satisfies the XTE J1814-338 measurement and also reaches the $2M_\odot$ limit, it ends up in the causality region, which is forbidden. So we can explain this measurement only if the maximum mass is less than $2M_\odot$ which then is ruled out because its a first condition for EoS to be accepted. There are several studies in this measurement, but all fail to reach a $2M_\odot$ constraint. Hence, the nature of XTE J1814-338 is very elusive because of its very low radii, which sits right away from other measurements.

2 Summary

The HESS J1731-347 and XTE J1814-338 measurements may hint at the presence of exotic matter such as quarks, hyperons, or condensates. For XTE J1814-338, such states might account for its compactness, while for HESS J1731-347, they could explain its stability at low mass.

Events like GW170817 provide stringent constraints on tidal deformability, favoring intermediate stiffness. Reconciling these with extreme cases like XTE J1814-338 is non-trivial.

These measurements test the precision and consistency of current instruments like NICER, XMM-Newton, and gravitational wave observatories. Further observations are critical to confirm these results and refine their uncer-

tainties.

Together, these measurements broaden the landscape of neutron star studies. They underscore the diversity of neutron star properties and demand a deeper exploration of dense matter physics. Furthermore, these results may hold clues to the nature of the strong force under extreme conditions, offering pathways to refine our understanding of fundamental interactions in the universe.

Future observations and theoretical developments are essential to interpret these challenging and unusual neutron star properties within a unified framework.

References

[1] B. P. Abbott and R. Abbott *et al.* Gw170817: Observation of gravitational waves from a binary neutron star inspiral. *Phys. Rev. Lett.*, 119:161101, Oct 2017.

[2] R. Abbott, T. D. Abbott, et al. Gw190814: Gravitational waves from the coalescence of a 23 solar mass black hole with a 2.6 solar mass compact object. *Astrophys. Jour.*, 896(2):L44, jun 2020.

[3] A. G. Abac et al. Observation of Gravitational Waves from the Coalescence of a 2.5–4.5 M $_\odot$ Compact Object and a Neutron Star. *Astrophys. J. Lett.*, 970(2):L34, 2024.

[4] Paul Demorest, Tim Pennucci, Scott Ransom, Mallory Roberts, and Jason Hessels. Shapiro Delay Measurement of A Two Solar Mass Neutron Star. *Nature*, 467:1081–1083, 2010.

[5] John Antoniadis et al. A Massive Pulsar in a Compact Relativistic Binary. *Science*, 340:6131, 2013.

[6] E. Fonseca et al. Refined Mass and Geometric Measurements of the High-mass PSR J0740+6620. *Astrophys. J. Lett.*, 915(1):L12, 2021.

[7] Tuomo Salmi et al. The Radius of the High-mass Pulsar PSR J0740+6620 with 3.6 yr of NICER Data. *Astrophys. J.*, 974:294, 2024.

[8] Thomas E. Riley et al. A NICER View of the Massive Pulsar PSR J0740+6620 Informed by Radio Timing and XMM-Newton Spectroscopy. *Astrophys. J. Lett.*, 918(2):L27, 2021.

[9] M. C. Miller et al. The radius of psr j0740+6620 from nicer and xmm-newton data. *The Astrophysical Journal Letters*, 918(2):L28, sep 2021.

[10] M. C. Miller *et al.* PSR j0030+0451 mass and radius from NICER data and implications for the properties of neutron star matter. *Astrophys. J.*, 887(1):L24, dec 2019.

[11] T. E. Riley *et al.* A NICER view of PSR j0030+0451: Millisecond pulsar parameter estimation. *Astrophys. J.*, 887(1):L21, dec 2019.

[12] Victor Doroshenko, Valery Suleimanov, Gerd Pühlhofer, and Andrea Santangelo. A strangely light neutron star within a supernova remnant. *Nature Astronomy*, 6(12):1444–1451, Dec 2022.

[13] Yves Kini et al. Constraining the Properties of the Thermonuclear Burst Oscillation Source XTE J1814-338 Through Pulse Profile Modelling. *Mon. Not. Roy. Astron. Soc.*, 535:1507, 2024.

[14] Thomas E. Riley et al. A nicer view of the massive pulsar psr j0740+6620 informed by radio timing and xmm-newton spectroscopy. *The Astrophysical Journal Letters*, 918(2):L27, sep 2021.

[15] Devarshi Choudhury et al. A NICER View of the Nearest and Brightest Millisecond Pulsar: PSR J0437–4715. *Astrophys. J. Lett.*, 971(1):L20, 2024.

[16] Ishfaq Ahmad Rather, Kauan D. Marquez, Betania C. Backes, Grigoris Panotopoulos, and Ilidio Lopes. Radial oscillations of hybrid stars and neutron stars including delta baryons: the effect of a slow quark phase transition. *JCAP*, 05:130, 2024.

[17] Prashant Thakur, Tuhin Malik, Arpan Das, T. K. Jha, B. K. Sharma, and Constança Providência. Feasibility of dark matter admixed neutron star based on recent observational constraints. 8 2024.

[18] Ishfaq Ahmad Rather, Grigoris Panotopoulos, and Ilídio Lopes. Quark models and radial oscillations: decoding the HESS J1731-347 compact object's equation of state. *Eur. Phys. J. C*, 83(11):1065, 2023.

Positron Emission Tomography (PET) Scan

R. Prasad and B. P. Singh
Department of Physics, Aligarh Muslim University, Aligarh, UP, India-202002

Abstract

Recently, I had an opportunity to interact with several senior as well as some junior medical doctors from large and reputed hospitals in Sydney, Australia. Most of them were radiologists and/or experts in interpreting the images/scans obtained from different types of diagnostic gadgets. As is common elsewhere, it is a common practice here as well for doctors to ask for the results of various diagnostic tests before prescribing any medication or deciding on the course of action. I asked these expert doctors whether they knew how a particular medical diagnostic tool or gadget, starting from a simple stethoscope to a complicated MRI or PET scan unit, really works. Though not surprising, most of them replied, "No". They said they know how to interpret a given image or scan but do not know how the image is taken by the machine. When asked if they would like to know how the scanning machine works, the reply was a quick and emphatic, "Yes." Later, I also discussed this point with my friends from different walks of life who use gadgets like a BP instrument or a glucometer. They all showed great eagerness to know, in simple and essentially non-mathematical language, the working of some frequently used medical diagnostic tools like a stethoscope, pulse oximeter, MRI, PET, or CT unit. I, therefore, took up a project on the subject. A book on the working of ten diagnostic gadgets is in the pipeline as the first phase of the project. A brief write-up on the PET scan, based on the material provided in the book, is presented here.

1 Introduction

Positron emission tomography is a technique used to identify and capture an image of an anatomical body part by studying the performance levels of its metabolic and/or biological processes. Humans eat food, digest it, and convert it primarily into glucose, amino acids (which make up proteins), and fatty acids (which make up fats). The digested food—glucose, etc.—is absorbed into the blood and distributed to different parts of the body through blood circulation. Tissues and cells in different body parts (anatomical structures) convert glucose/sugars into energy. Energy is defined as the ability to do work. It would not be wrong to say that modern civilization has been made possible because humans learned how to transform energy from one form to another and then use it to perform work. Energy is something that a physical system may possess, and work is something that an energetic system may perform. As such, both energy and work are measured in the same unit, called the joule, represented by the letter J. Of course, several other units are also used to measure energy and work.

The pathways in the human body that convert food to energy constitute metabolic activity. Metabolism refers to the chemical (metabolic) processes that take place as the human body converts food and drinks into energy. Metabolism in the human body constantly provides it with energy for essential body functions like breathing, circulating blood, growing and repairing cells, managing hormone levels, regulating body temperature, and digesting food, etc. The human body needs a minimum number of joules (of energy) to sustain these essential functions. This minimum number of joules is called the Basal Metabolic Rate (BMR). The BMR value varies from person to person. An average man has a BMR of around 7100 kilojoules (kJ) per day, while the average woman has a BMR of around 5900 kJ per day.

It has been observed that the metabolic activity of abnormal body parts, for example, the anatomic part that has cancer, increases much more than that of the corresponding normal part. Normal cells have a particular way of converting carbohydrates, fats, and proteins into energy; however, cancer cells do it differently. Compared to healthy cells, cancer cells use more glucose to produce the same amount of energy. Therefore, the consumption rate of glucose in cancer-infected body parts is much higher than in the corresponding healthy parts. Similarly, the metabolic activity of parts of the brain that do not function properly becomes considerably enhanced compared to the parts that function normally. As a result of the enhanced metabolic activity, a considerably larger amount of sugar/glucose accumulates in the abnormal body part.

In PET scanning, the patient is given some form of sugar, like glucose, that has a very small amount of short-lived radioactive atoms attached to it. Such sugar is called tracer-labeled sugar, and the short-lived radioactive material is referred to as the tracer. The glucose labeled with radioactive tracer atoms is generally injected into the patient via a vein using an intravenous (IV) line. Within 30 to 90 minutes, the injected tracer-labeled glucose gets distributed in the patient's body and accumulates in the abnormal body part in larger concentrations, where the radioactive atoms undergo decay. The decaying radioactive atoms of the tracer, emit radiation in the abnormal body part where they have accumulated in large quantities. Radiation emitted from the abnormal body part is recorded by suitable detectors housed in the scanner of the system. The detectors convey the information obtained to the computer, which analyzes the data and illuminates the abnormal area of the body where the radioactive material has accumulated, producing the required image of the abnormal body part. The intensity of the image depends on the decay rate of the tracer atoms; the larger the number of tracer atoms accumulated in the affected part, the greater the metabolic activity of the part, corresponding to a higher level of abnormality

2 Radioactivity and Tracers

Some atoms in nature are found to be unstable and undergo spontaneous disintegration. This property of disintegration is called natural radioactivity. Essentially, it is the nucleus of a radioactive atom that disintegrates; hence, radioactivity is a nuclear phenomenon. If one takes some atoms of a radioactive material, the number of radioactive atoms decreases with time; the time in which the number of radioactive atoms reduces to half of its original number is called the "half-life" of the atom. Radioactive atoms with half-lives ranging from several thousand and billions of years to a few milli-microseconds are found in nature.

It is also possible to create new radioactive atoms by hitting a sample of stable atoms with focused beams of high-energy nuclear particles like neutrons, protons, alpha particles, etc. Nuclear projectiles may be accelerated to high energies in special machines called particle accelerators or atom smashers. An important property of radioactive atoms is that each atom of a given species decays by a very specific decay mode. The decay modes of atoms of two different species are different from each other. This property of individual decay modes makes it possible to identify the radioactive atom in a unique way, without any ambiguity, by studying its decay mode. Radioactive atoms, when they decay, emit specific radiation, like alpha particles, beta particles, and/or gamma rays. The alpha particle is the nucleus of the helium atom, while there may be two types of beta particles: beta-plus, denoted as β^+, and beta-minus, denoted by β^-. Gamma rays, high-energy electromagnetic radiation denoted by γ, are also emitted in radioactive decay.

Radioactive atoms of short half-lives are often used for research on living beings and plants. A small quantity of these short half-life radioactive atoms, called tracers or radiopharmaceuticals, is mixed with a suitable substance or fluid and injected into the living object. The flow of the injected substance or fluid in the object may be monitored by detecting the specific radiation emitted by the decaying radioactive tracer atoms. The reason why atoms of short half-life are used as tracers is the fact that all the radioactive tracer atoms of short half-life injected into the living object decay in a short time. It is estimated that in a time span equal to about five times the half-life of the atomic nucleus, almost 99.9% of the injected atoms decay.

In PET scanning, radioactive atoms of ^{18}F (an isotope of the element fluorine) are mixed with glucose as tracer atoms. The ^{18}F-tracer-mixed glucose is called fluorodeoxyglucose, or FDG. The half-life of ^{18}F is about 110 minutes, and therefore, almost all atoms of ^{18}F decay out of the body within, say, 10 hours of their injection into the body. When an atom of ^{18}F decays, it emits a nuclear particle called a positron, which is denoted by the symbol β^+. It is like an electron that revolves around the nucleus in atoms, with the difference that while the electron (denoted by e^- or β^-) has a negative electric charge, the positron has an equal amount of positive electric charge. The positron is also called the antiparticle of an electron. In particle physics, there are several pairs of particles and their antiparticles.

3 Annihilation gamma rays

Since the metabolic activity of the abnormal body part (infected with cancer or not working normally) is higher than the normal part, a considerably large amount of ^{18}F-activated sugar injected into the blood through an IV line gets accumulated in the cancerous or abnormal body part. The tracer atoms of ^{18}F, accumulated in the abnormal part, undergo radioactive decay, emitting one positron (β^+) per decay in the abnormal body part. The emitted positron travels a very small distance, less than 1 mm, before it encounters an electron (β^-) of some atom present in this part. Positrons (emitted by tracer atoms) and electrons (present in atoms in the body part) undergo a very special phenomenon called 'annihilation' when they meet each other.

In the process of annihilation, the positron and the electron vanish (get converted into energy), and two gamma radiations, each of energy 511 keV, are emitted simultaneously in opposite directions. The angle between the emitted gamma pair will be 180° if they annihilate at rest (i.e., the process of annihilation takes place when both the positron and the electron are at rest or stationery). However, in most cases, the annihilation occurs while they are still in motion, and the angle will be slightly less than 180° (maybe 178°). Fig. 1, shows the decay sequence of the ^{18}F atom and the annihilation of the electron-positron pair. It may be noted that the sizes of atoms, the position, and the electron are highly exaggerated in the figure.

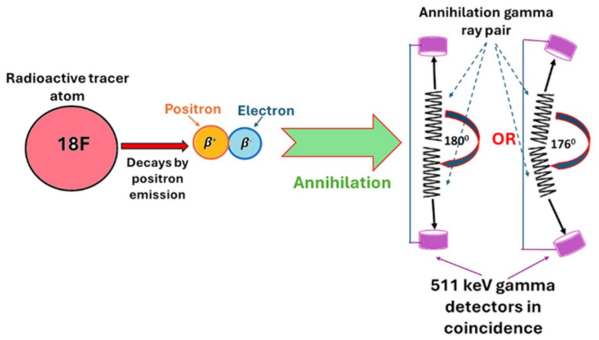

Fig. 1: *Pictorial representation of ^{18}F decay and gamma annihilation.*

A few pairs of gamma ray detectors, placed opposite to each other, are kept in the scanner of the PET system. The gamma detectors of each pair are tuned to detect annihilation gammas of 511 keV energy that reach the two detectors within a very short time of the order of 10^{-9} seconds. The selection of gamma ray energy and time coincidence between the two gamma rays detected by the two detectors ensures that the possibility of detecting stray gamma rays, which are present in the background and are not associated with the annihilation of the positron-electron pair, is reduced to almost zero. The gammas detected by the two detectors are actually the annihilation gammas created as a result of the annihilation of the positron-electron pair. The detectors generate signals only for 511 keV gamma rays that are in time coincidence in the two detectors placed diagonally opposite each other.

The detectors provide coincident gamma signals to the computer of the system. The computer analyzes the detector data using specialized software and, by extending the trajectories of the detected gammas in the backward direction with the help of suitable software. This helps in determining the point on the patient's body where the event of annihilation has taken place. Further, the computer also illuminates these annihilation points. Since there is excess accumulation of ^{18}F-loaded sugar (FDG) in the abnormal/infected body part, many positron-electron annihilation events take place in that part. These events are detected by coincidence gamma detectors, and the part is brightly illuminated by the computer in comparison to the other normally functioning body parts. It may be noted that in actual PET images, the abnormal/infected body parts appear darker since they are negative images of the actual photograph. In short, PET scanning is the technique of mapping the 3-D tracer concentration in the body using the positron-electron annihilation process.

4 PET Scanner unit

A PET scan machine, shown in Fig. 2, has four important components: (a) a control console, (b) a powerful minicomputer with appropriate analyzing software, (c) a doughnut-shaped scanner unit that has a large hole at its center, and (d) a patient bed that can slide into the central hole of the scanner unit. The scanner unit may rotate at different speeds around the bed. There are a few (up to four) detector setups fixed in the scanner unit, spaced symmetrically. These detector setups rotate around the patient's bed with the rotation of the scanner unit.

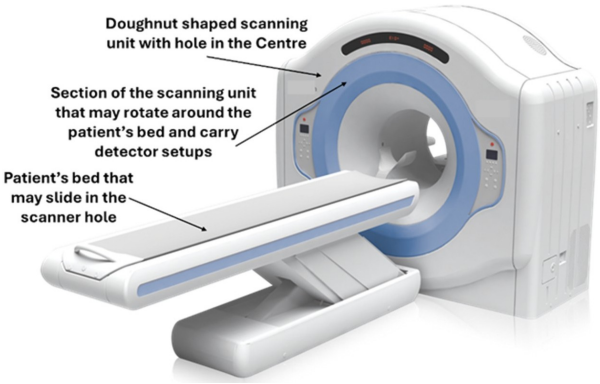

Fig. 2: *An image of a PET scan Unit*

Each detector setup consists of a pair of gamma-ray detectors held diametrically opposite to each other to detect the pair of coincident annihilation gamma rays emitted when a positron (emitted by the tracer atom) combines with an electron (present in the human body). Events (simultaneous detection of 511 keV gammas by the two detectors of a given detector setup) recorded by different detector setups activate the analyzing software of the minicomputer. Then it extrapolates the trajectories of the detected

gamma rays to identify and illuminate the point on the human body where the annihilation event has taken place. The computer also takes a snapshot of the illuminated area.

In each rotation of the scanner, several snapshots of the part of the patient's body lying immediately below the rotating scanner, with illuminated areas indicating the locations with large FDG concentrations, are taken by different detector setups. The analyzing software generates a single image by synthesizing the large number of snapshots taken by different detector setups in one rotation. This image is called a slice. With the patient lying on the bed, the operator/technician operating the system remotely from the control console may bring different sections of the patient's body under the scanner one after the other and generate several slices of the target body part. A full-body image is made by synthesizing images/slices of different sections.

A full-body PET scan is of great help in identifying regions of enhanced metabolic activity in the body, which may be locations with high potential for future development of cancer, etc., or may indicate the onset of abnormal metabolic activity. To further confirm the PET scan findings, a CT scan of the patient is also taken in most cases.

PET scanning is a noninvasive, harmless, and safe method of imaging body parts that have higher than normal metabolic/biological activity. Since the radioactive tracer material injected into the patient is in very small amounts and has a short half-life, it decays out of the body within a few hours. Moreover, the tracer decay product, the positron itself, has a very short time span, combining with an electron within a few nanoseconds of its emission. As such, there is no residual effect of the tracer left in the patient after a few hours. During this time, there is also no adverse effect either on the patient or on the people staying near the patient. Fig. 3 shows the FDG PET scan of a patient having a cancer infected lymph node and a cancer developing in the neck.

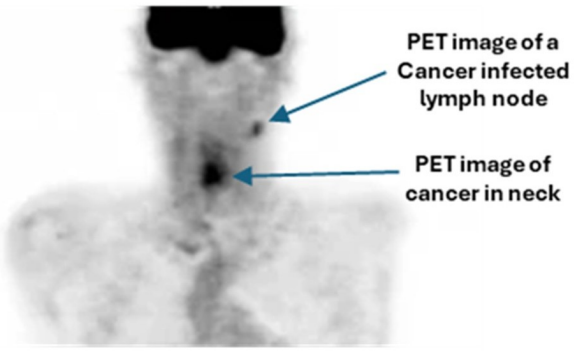

Fig. 3: *FDG PET scan of neck indicating the infected lymph node and a part of neck*

In conclusion, PET scanning is an important, noninvasive imaging technique that helps doctors find areas of abnormal activity in the body, like early signs of cancer. This technology relies on nuclear physics, using small amounts of radioactive tracers to detect changes in metabolism. The process works by detecting positrons emitted during radioactive decay, which helps create detailed images of the body. Nuclear physics plays a key role in making PET scans possible, and it has greatly improved how doctors diagnose and treat various health conditions.

Assessing Exposure to Natural Radiation and Health Implications

B. P. Singh and R. Prasad
Department of Physics, Aligarh Muslim University, Aligarh, UP, India-202002

Abstract

This exploration into natural radiation's origins within Earth's environment covers its historical progression, health and environmental impacts, and the essential evaluation as well as regulation of these sources. It underscores the need for understanding and establishing safety measures, encompassing types, exposure methods, health effects, regulations, and future challenges. As a matter of fact, cosmic, terrestrial, and internal elements contribute to natural radiation. Cosmic rays from the outer space, terrestrial sources like uranium, and internal absorption from within the body may pose health risks. Measurement units like Roentgen, Gray, Sievert, and Becquerel regulate exposure, vital for safeguarding health and the environment. Exposure assessment tools like Thermos-Luminescent Dosimeter (TLD), Optical Stimulated Luminescent (OSL) dosimeters, and gamma spectrometry measure doses and identify radioisotopes. Biological dosimetry evaluates radiation effects on living organisms, offering insights into health risks and management strategies. Advancements like gamma-ray spectrometry and digital Geiger Muller (GM) Counters enhance understanding and data precision in various environments, enabling risk assessment and regulatory compliance. Attempts have been made to touch upon the health risks like lung cancer, genetic mutations, tissue damage, emphasizing the need for extensive research and safety strategies. International regulatory frameworks manage natural radiation risks, with nations setting varying limits. Environmental impact studies aim to preserve safety for future generations.

1 Introduction

Natural radiation refers to electromagnetic waves or particles that originate from naturally occurring sources and are found in the environment. It is believed that this type of natural radiation has been present since the formation of the Earth and is an integral part of its natural environment. This includes cosmic radiation from outer space, radiation produced by radioactive elements present in soil, rocks, and building materials, as well as radiation from radon gas. Thus, as shown in Fig. 1, we can say that natural radiation is present everywhere around us.

This radiation can equally affect our health and environment. If we understand this radiation, it can help us establish safety standards and potentially reduce the associated risks. It also provides a basis for comparing the effects of human-made radiation sources from industries, medicine, and nuclear technology. It is noteworthy that the historical context and understanding of natural radiation composition have undergone significant changes over time. Initially, awareness about natural radiation was quite limited, and the potential health effects, whether positive or negative, were not fully understood. After Henri Becquerel's discovery of radioactivity in 1896, and subsequent work by Marie Curie and Pierre Curie, efforts were quickly made to understand the composition of natural radiation. Research revealed that radioactive elements like uranium and thorium contribute to the composition of natural radiation. Later, radon was identified as a radioactive gas, and due to its hazardous effects, efforts were made toward better measurement and safety standards. Radon levels were measured at various locations, and methods and measures were developed to address the associated risks, such as increased lung cancer rates [1].

Fig. 1: *Typical sources of Natural Radiation — Food, Air, Home, Body, Soil, Cement, etc.*

Advances in technology and studies have helped to improve our understanding of natural radiation. These studies assist us in providing strong policies [2] for public health and environmental protection. Assessing the composition of natural radiation is crucial for the protection of human health and the environment. If we can identify high-radiation areas and regulate natural and artificial sources of radiation, we can increase necessary precautions and develop effective policies for the long-term welfare of society [3]. The following description aims to provide a comprehensive understanding of the various types of natural radiation, exposure assessment methods, health-related outcomes, regulatory framework, environmental impacts, and future possibilities and challenges.

2 Types of Natural Radiation

Natural radiation occurs in various forms, including cosmic, terrestrial, and internal radiation. Cosmic radiation originates from the sun and other celestial bodies, continuously bombarding the Earth's atmosphere with high-energy particles. Terrestrial radiation comes from radioactive elements within the Earth's surface, such as uranium, thorium, and potassium. Radon gas, a decay product of uranium, can accumulate indoors and poses a significant health risk. Internal radiation results from the ingestion, inhalation, or absorption of radioactive substances by living organisms, presenting challenges for assessment and regulation. These different sources contribute to natural exposure.

In Fig. 2, a typical background gamma-ray spectrum recorded in nuclear laboratory over a fifteen-minute period using a high-purity germanium (HPGe) detector is shown. Several energy peaks related to emissions from background radioactive materials can be observed here. Despite the detector shielding, a significant amount of background radiation is present. Radon gas emitted from the soil poses a major internal health risk, primarily leading to lung cancer. Cosmic rays, though less impactful, can increase cancer risk among airline crew members and frequent fliers. To prevent organ damage from internal radiation due to ingested radioactive substances, safe exposure levels are necessary. Therefore, understanding these sources is essential for effectively reducing risks and maintaining safe radiation levels.

Radiation risk is measured using various units based on specific contexts [4]. The Roentgen (R) measures the amount of ionization in air caused by X-rays and gamma rays; for this type of radiation, 1 R is approximately equal to 0.01 Gray (Gy). Gray (Gy) is the standard unit for absorbed dose, representing the absorption of one joule of radiation energy per kilogram of matter. For certain types of radiation, such as gamma rays and X-rays, one Gray is equivalent to one Sievert (Sv). However, for other types of radiation, a specific conversion factor is applied. Sievert (Sv) measures the effective dose by considering the biological effects of radiation on living tissues. The Becquerel (Bq) determines the level of radioactivity of a source, with specific relationships between Bq, Gy, and Sv depending on the type of radiation and the particular radioactive substances involved. These units are essential for assessing and comparing radiation risks across various fields, including medicine, industry, and environmental monitoring. The Table 1, presents the different radiation protection measures based on the scale of exposure and associates them with various sources and activities. It emphasizes how radiation safety is applied to different segments of society. The protection strategies are tailored to different radiation sources and practices, including natural radiation, medical applications, nuclear power, industrial uses, and space flight, ensuring comprehensive safety across diverse environments.

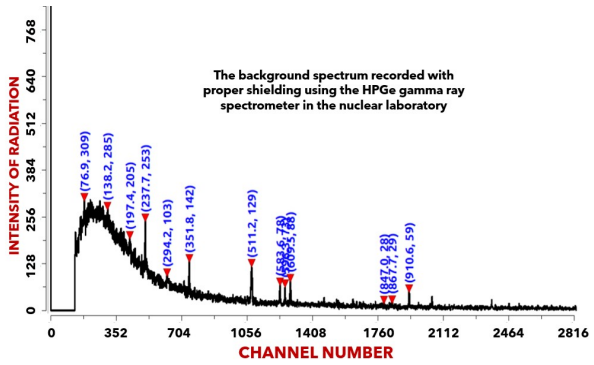

Fig. 2: *Gamma-ray spectrum of the typical background recorded by a high-purity germanium detector over a duration of fifteen minutes. As observed, despite the shielding of the detector, a significant amount of radiation is present in the background.*

3 Methods of evaluating radiation exposure

Dosimetry uses devices like Thermo-Luminescent Dosimeters (TLD) and Optically Stimulated Luminescence (OSL) dosimeters to measure absorbed radiation doses [5]. TLDs measure cumulative exposure over time by gauging the light emitted when heated, while OSL dosimeters provide precise data on the dose received at specific intervals by measuring light from trapped electrons. These methods are used in various fields, including occupational safety, medical facilities, and environmental monitoring, to ensure that radiation levels remain within safe limits [5]. Radon, a radioactive gas, forms from the decay

Table 1: *Overview of Radiation Protection Measures and Associated Sources*

Radiation Protection Measures for	**Sources and Activities**
Entire Population	Natural Radiation
Large Segments of Society	Medical Uses
Groups of People	Nuclear Energy
Smaller Communities	Industrial, Research, and Other Applications
Individuals	Space Exploration, Flight Crew members

of uranium and radium found in soil, rocks, and water. It can enter buildings through cracks, posing a risk to indoor air quality. The decay sequence from ^{238}U to ^{222}Rn is provided below for reference [6].

^{238}U ($t_{1/2} \approx 4.47$ billion years) $\rightarrow$ $^{234}Th + \alpha$-particle
^{234}Th ($t_{1/2} \approx 24.1$ days) $\rightarrow$ $^{234m}Pa + \beta^-$-particle
^{234m}Pa ($t_{1/2} \approx 1.17$ minutes) $\rightarrow$ $^{234}U + \beta^-$-particle
^{234}U ($t_{1/2} \approx 245{,}000$ years) $\rightarrow$ $^{230}Th + \alpha$-particle
^{230}Th ($t_{1/2} \approx 75{,}380$ years) $\rightarrow$ $^{226}Ra + \alpha$-particle
^{226}Ra ($t_{1/2} \approx 1{,}600$ years) $\rightarrow$ $^{222}Rn + \alpha$-particle

In measurement techniques for laboratory analysis, charcoal canisters, alpha-track detectors for recording damage tracks on films, and indoor radon monitors [7] are included. These methods help in reducing health risks associated with radon, particularly lung cancer. Gamma spectrometry involves the use of gamma-ray detectors [8,9,10] to identify and quantify radioactive isotopes present in samples. These detectors operate on the principle of detecting specific gamma rays emitted by the radioactive isotopes [11]. This provides precise information about the specific radioactive nuclei contributing to radiation levels in soil, water, and biological materials. Focusing on radiation levels in the natural environment, gamma spectrometry is widely used in environmental monitoring, geological surveys, and research laboratories. For tracking radiation levels, Geiger-Muller counters [12] and "scintillation" detectors [12] are used at environmental monitoring stations. This data helps in identifying potential risks to human and environmental health [13]. Biological dosimetry techniques assess the effects of radiation on living organisms. These methods include cytogenetic analysis and biomarker measurements, providing insights into health risks and aiding radiation management strategies.

Monitoring and measurement techniques are crucial for comprehensive assessment of natural radiation risks. Monitoring techniques measure radiation levels, assist in effective risk management, and ensure human and environmental safety [14,15]. These techniques ensure compliance with radiation safety standards, enabling prompt intervention to maintain regulatory compliance and public safety. Continuous monitoring detects unusual fluctuations, allowing timely checks and corrective actions to minimize long-term risk. Data from monitoring provides information for extensive evaluation, helping in the development of evidence-based health policies and preventive measures [16]. The assessment of radiation levels in the environment also enables targeted safety measures, maintaining ecological balance, and supporting sustainable resource management [17].

Technological advances have significantly improved exposure assessment methods, leading to revolutionary changes in the accuracy, efficiency, and scope of measuring and monitoring natural radiation. Recent progress includes the integration of satellite-based gamma-ray spectrometry and aerial radiometric surveys, expanding spatial coverage for detailed insights into the distribution of natural radiation sources. Additionally, instruments like digital Geiger-Muller counters provide high sensitivity and real-time data collection [18,19], enhancing efficiency under various environmental conditions. Fig. 3 shows a typical Geiger-Muller counter setup, which can be used for radiation monitoring.

Fig. 3: *A typical Geiger-Müller counter setup that can be used for radiation monitoring.*

4 A brief on Working of Geiger Muller Counter

The Geiger discharge process begins when incident radiation interacts with the fill gas, typically argon,

inside the Geiger-Müller (GM) tube. This causes ionization and creating an electron-ion pair. The electron is then accelerated toward the positively charged anode by a strong electric field. As it travels, it gains enough energy to knock additional electrons from nearby atoms, triggering a chain reaction known as a Townsend avalanche [4]. This cascading effect results in a rapid multiplication of electrons. Some of the ionized atoms may release photons as they return to their ground state. These photons can ionize other atoms, further contributing to the avalanche effect in a process known as a Geiger discharge. This amplification allows a single ionization event to produce between one billion and 10 billion electrons reaching the anode.

The discharge process stops when the positively charged ions, which are much heavier than electrons and move more slowly, accumulate around the central anode wire and reduce the electric field in the tube. This reduction in voltage prevents electrons from gaining enough energy for further ionization, effectively ending the discharge. The ions finally drift toward the cathode, where they capture electrons and return to their neutral state. This process takes several milliseconds, during which the tube experiences dead time, making it temporarily unable to detect new radiation.

To prevent false signals caused by residual energy, GM tubes often use quench gases such as ethyl alcohol. These gases absorb excess energy, preventing unnecessary discharges and reducing dead time. Alternatively, external quenching can be employed, temporarily lowering the tube's voltage after a discharge. However, external quenching increases dead time significantly, making it less suitable for detecting high radiation levels. Quench gases are preferred for their efficiency, though they degrade over time. Adding halogens like chlorine or bromine helps extend their lifespan by allowing the gas molecules to recombine after breaking apart. The Geiger discharge process relies on the ionization of fill gas by radiation, followed by a cascade of electron multiplication. This amplification mechanism helps Geiger counters to detect even small amounts of radiation with high sensitivity, while quenching methods ensure accurate and reliable readings by managing dead time and preventing false signals [12].

Recently, advanced systems equipped with artificial intelligence (AI) capabilities process extensive data collection, identifying trends in decision-making and risk management. Portable devices with wireless integration facilitate real-time data transmission for seamless integration and convenient statistical visualization, improving accessibility and usability. Compact and sensitive instruments enable continuous, personalized radiation monitoring for both personal and occupational safety, revolutionizing exposure assessment. By leveraging these technological advancements, risk assessment methods have become more robust and adaptable, facilitating informed decision-making, implementing measures, and effectively managing natural radiation risks to safeguard human health and the environment.

5 Units of Radiation Measurement: Understanding and Conversions

In nuclear radiation measurements, various units are used depending on the context, whether in laboratory research or in common practice. Radiation activity, which refers to the strength of a radioactive source, is measured in Becquerels (Bq). One Bq represents one disintegration per second. In older systems, the Curie (Ci) was used, where 1 Ci is equal to 3.7×10^{10} Bq. Absorbed dose, which quantifies the energy deposited in matter by radiation, is expressed in Grays (Gy), with 1 Gy representing 1 joule of energy absorbed per kilogram. The older unit for this is the Rad, where 1 Gy equals 100 rad. When we consider the biological impact of radiation, the Sievert (Sv) is the standard unit. It accounts for the absorbed dose and the type of radiation through a quality factor (QF). For instance, gamma rays have a QF of 1, while alpha particles have a QF of 20. The older unit, the Rem, is still used in some contexts, with 1 Sv is equal to 100 rem. Exposure, specifically the ionization produced in the air, is measured in Coulombs per kilogram (C/kg). In earlier days, the Roentgen (R) was the common unit, with 1 C/kg being approximately 3876 R. As a matter of fact, in practical scenarios, patient doses in medical diagnostics are often reported in millisieverts (mSv), while radiation workers' exposure is tracked in Sv or mSv. Environmental radiation monitoring frequently uses μSv/h (microsieverts per hour) to report dose rates. The table-2, provides the standard units used for measuring different aspects of radiation, including activity, absorbed dose, dose equivalent, and exposure, along with their older counterparts. It highlights the conversions between SI units and traditional units to ensure clarity and consistency in radiation measurement across various applications.

6 Health Implications

Let us briefly discuss the effects of continuous exposure to these natural radiations. Prolonged exposure to natural radiation, such as radon gas, significantly increases the risk of lung cancer, particularly in poorly ventilated indoor spaces. Ionizing radia-

Table 2: *Conversion Table of Radiation Measurement Units [4]*

Quantity	SI Unit	Older Unit	Conversion
Activity	Bq	Ci	1 Ci = 3.7×10^{10} Bq
Absorbed Dose	Gy	Rad	1 Gy = 100 rad
Dose Equivalent	Sv	Rem	1 Sv = 100 rem
Exposure	C/Kg	R	1 C/kg $\approx$ 3876 R

tion from these sources can cause genetic mutations and chromosomal abnormalities, potentially leading to hereditary disorders. It can also damage radiation-sensitive organs, resulting in radiation burns, cataracts, and reproductive issues. Additionally, it can weaken the immune system, making the individual more susceptible to diseases. Studies suggest potential cardiovascular and neurological effects, highlighting the need for active monitoring and stringent radiation risk management for overall health protection. In Table 3, a comparison between natural radiation risks and artificial sources along with their associated risks are presented.

A comparative view of the risks associated with natural and artificial sources of radiation reveals distinct differences in their origins and impacts. Natural radiation, which arises from cosmic, terrestrial, and internal sources, is widespread and generally unavoidable. The risks associated with natural radiation include an increased likelihood of certain cancers, especially lung cancer due to exposure to radon gas, as well as genetic mutations and chromosomal abnormalities. Prolonged exposure to natural radiation can also lead to tissue damage in radiation-sensitive organs, with potential immunological, cardiovascular, and neurological effects.

On the other hand, artificial radiation primarily results from medical procedures like X-rays and CT scans, nuclear energy production, laboratory experiments, and industrial applications. Unlike natural radiation, exposure to artificial radiation is typically controlled and regulated, yet it still carries certain risks. These include a higher risk of cancer due to cumulative exposure from diagnostic and therapeutic procedures. In the event of nuclear or industrial accidents, individuals exposed to high levels of radiation may suffer from both acute and long-term radiation sickness. Furthermore, artificial radiation poses potential long-term genetic and reproductive health risks, along with the dangers of environmental contamination and radioactive material leakage. In recent years, several studies and research have focused on understanding the effects of natural radiation risks on human health. Research has extensively examined the relationship between prolonged exposure to radon gas, a significant contributor to natural radiation, and the increasing risk of lung cancer. Studies have emphasized the importance of effective radon monitoring and mitigation strategies to reduce the risk of lung cancer from indoor radon exposure, particularly in residential and occupational settings.

Scientific studies have thoroughly investigated the genetic and chromosomal effects of prolonged exposure to natural radiation, especially ionizing radiation. The research has demonstrated the potential for genetic mutations and chromosomal aberrations resulting from continuous exposure to natural radiation, underscoring the importance of effective radiation protection measures to reduce genetic health risks. The studies have also explored the dermatological effects of natural radiation, indicating the possibility of radiation-induced skin damage. These studies highlight the need for appropriate protective measures, especially in occupations or environments with elevated natural radiation levels, to minimize the risk of radiation-induced skin conditions and related health complications. Research has shown that prolonged exposure to certain forms of natural radiation can lead to immunosuppressive effects, increasing the likelihood of infectious diseases and other health complications. Epidemiological research plays a crucial role in identifying health effects associated with natural radiation risks, particularly in recognizing elevated cancer rates and other adverse health outcomes. Ongoing studies continue to advance our understanding of health effects, ensuring the well-being of populations exposed to natural radiation.

7 Regulatory Framework

International and national regulatory guidelines are essential for assessing and managing the risks of natural radiation to ensure human health safety. The International Commission on Radiological Protection (ICRP) is a globally recognized organization that provides recommendations on radiation protection. Its guidelines establish frameworks for assessing radiation risks and implementing protective measures, including those related to natural radiation risks. ICRP recommendations influence the development of national regulations worldwide.

Table 3:

Type of Radiation Source	**Exposure Characteristics**	**Associated Risks**
Natural Radiation	Originates from cosmic, terrestrial, and internal sources. Exposure is generally unavoidable and widespread.	1. Increased risk of certain cancers, especially lung cancer due to radon gas. 2. Genetic mutations and chromosomal abnormalities. 3. Tissue damage in radiation-sensitive organs. 4. Immunological effects and potential cardiovascular and neurological effects.
Artificial Radiation	Arises from medical procedures like X-rays, CT scans, nuclear energy production, laboratory use, and industrial applications. Exposure is generally controlled and regulated	1. Increased risk of cancer due to cumulative radiation exposure from diagnostic and therapeutic procedures. 2. Potential long-term genetic and reproductive health effects. 3. Acute and long-term radiation sickness in individuals exposed to high levels of radiation during nuclear accidents or industrial accidents. 4. Environmental contamination and the risk of radioactive material leakage

The International Atomic Energy Agency (IAEA), Vienna, Austria establishes safety standards and provides guidance on radiation protection. It helps member countries implement these standards and supports the assessment and management of natural radiation risks through various programs and publications. The United Nations Scientific Committee on the Effects of Atomic Radiation (UNSCEAR) is a United Nations body responsible for assessing the global level of radiation risks and their effects on human health, preparing comprehensive reports and data to inform international radiation safety standards.

Several countries have dedicated environmental protection institutions responsible for monitoring and regulating radiation risks from natural sources. These institutions establish limits and guidelines for various natural radiation sources, including radon gas, cosmic radiation, and terrestrial radiation. In the United States, the Occupational Safety and Health Administration (OSHA) sets guidelines for occupational radiation risks, including those related to natural radiation sources in workplaces. These guidelines are designed to protect workers from significant radiation risks. National public health and safety authorities, often in collaboration with environmental and nuclear regulatory bodies, also establish rules for natural radiation risks in residential and public sectors. The goal of these agencies is to protect public health by setting permissible levels and providing guidance on radon mitigation in homes and workplaces.

The current permissible limits for natural radiation risks vary globally and are regularly updated based on scientific research and regulatory provisions. The World Health Organization (WHO) recommends indoor radon levels below 100 Bq/m^3, while national authorities set occupational risk limits. Cosmic radiation limits primarily apply to the aviation sector, with specific guidelines for aircrew and regular passengers. Terrestrial radiation risks are managed through building codes, and radon mitigation measures are implemented in some countries.

Many countries have established permissible limits for natural background radiation, which includes contributions from both cosmic and terrestrial sources. The discrepancies in radiation management methods across countries highlight the need for an international radiation safety system. Different regulations on medical radiation and various radiation risk limits for workers and patients emphasize the need for universally accepted international standards. These limits are designed to ensure that radiation risks from natural sources remain within acceptable levels for the general public, preventing harm.

The permissible radiation exposure limits (measured in mSv/year) vary across different countries (See Fig. 4). In Canada, the limit is set at 9.0 mSv/year, the highest among the listed nations. Germany follows with a limit of 5.0 mSv/year, while Japan allows up to 3.8 mSv/year. The United States of America has a limit of 3.1 mSv/year, and the United Kingdom permits 2.2 mSv/year. India has the lowest permissible limit, set at 1.5 mSv/year. These variations

reflect each country's approach to regulating radiation exposure to ensure public safety.

It can be observed that the permissible limits for natural radiation may vary significantly depending on the specific regions of these countries and the related guidelines set by their regulatory authorities. It is important to consult the latest guidelines and regulations from the International Atomic Energy Agency, the International Commission on Radiological Protection, and national regulatory agencies. These standards are subject to periodic updates and revisions; therefore, it is essential to stay informed about any changes to ensure compliance with the latest safety guidelines. A robust regulatory framework is critical to ensuring public health and environmental safety.

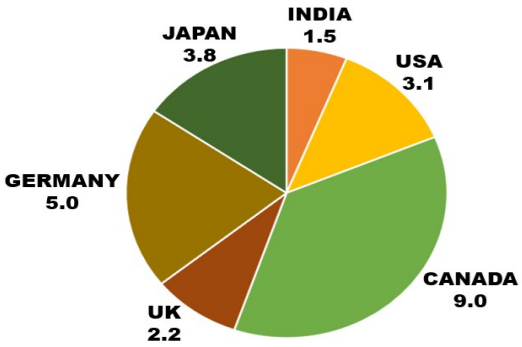

Fig. 4: *Permissible radiation exposure limits (mSv/year) in various countries*

8 Environmental Effects

Natural radiation affects biological systems, genetic diversity, and ecosystems. Soil and water pollution pose threats to plants and aquatic life, necessitating effective environmental management. Understanding its role in microbial communities is crucial for ecosystem stability. A comprehensive analysis guides strategies for conservation, sustainability, and risk mitigation.

There are several studies and examples demonstrating the effects of radiation on flora and fauna. A prominent example is the impact of radiation exposure on vegetation and wildlife in the areas surrounding the Chernobyl and Fukushima nuclear disasters. These events have provided valuable insights into the effects of radiation on various living organisms. The explosion at the Chernobyl nuclear power plant released large amounts of radioactive substances into the environment. Studies conducted in the area show various impacts on local flora and fauna [20]. For instance, researchers observed mutations and changes in the reproductive capacities of plants, as well as changes in the populations and behaviour of animals such as birds, mammals, and insects. The Fukushima nuclear disaster resulted in the release of radioactive substances into the environment, affecting nearby ecosystems. Studies conducted after the event also highlighted the effects of radiation on aquatic life. Changes in the abundance and diversity of some plant and animal species, as well as potential genetic effects on the affected populations, were observed. Additionally, some regions of the world are naturally known to have radioactive areas. These areas have higher levels of natural background radiation. This has provided researchers the opportunity to study the long-term effects of radiation on local ecosystems. It has shown adaptation to high radiation levels in plant and animal species, as well as potential impacts on their evolutionary processes. Fig. 5 illustrates the biological effects of chronic and acute radiations, highlighting results from experiments on model organisms such as Caenorhabditis elegans (C. elegans), which clarify the long-term and immediate effects of these radiations.

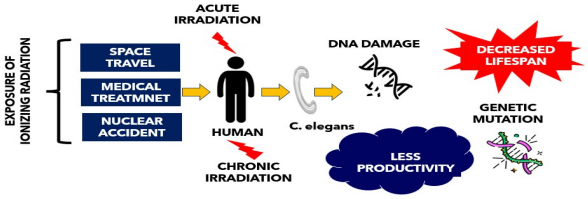

Fig. 5: *Biological effects of chronic and acute radiation*

A comprehensive approach, including monitoring systems and regulatory frameworks, helps reduce environmental risks. Public awareness campaigns, especially among schoolchildren [21,22], can promote safety practices, while risk assessments in land use planning can minimize risks. Environmental improvements, biodiversity conservation, and proper waste management are essential for sustainable development. Ongoing research and innovation are crucial for managing natural radiation risks and preserving human well-being.

9 Future Possibilities and Challenges

Natural radiation risk assessment is advancing with more sensitive detectors, instruments, and real-time remote sensing devices. The integration of big data analytics and artificial intelligence is likely to identify exposure trends. Additionally, improved computational models will predict radiation behaviour and

risk levels. Bioindicators and biomarkers will contribute to understanding risks and provide insights into biological effects. Standardized regulations and data integration will support effective environmental and public health management.

Challenges remain in understanding the effects of radiation on ecosystems and long-term human health in high-radiation areas. Universal regulatory frameworks, community engagement, proper education, and information sharing are essential for global understanding and effective management. There is a need for broad efforts to increase public awareness and understanding of natural radiation risks. This includes educational campaigns through various communication channels such as social media, television, radio, and workshops, providing accurate information about sources and potential health effects of radiation.

This article presents key challenges related to nuclear radiation exposure and suggests methods for addressing them. These solutions focus on fostering group discussions, promoting in-depth understanding, and introducing program elements that enhance awareness and community involvement in tackling social and educational issues. The ultimate goal of these strategies is to increase public engagement and understanding of the risks associated with radiation exposure. One of today's major challenges is managing nuclear radiation and its effects. To address this, it's crucial to strengthen regulatory research and monitoring systems globally. Community involvement through awareness programs can play a vital role in building understanding of science and technology, with a strong emphasis on safety and sensitivity. To address the long-term impacts of radiation on human health, widespread health awareness initiatives are essential. Collaborating with communities can encourage healthier lifestyles and greater awareness of personal health risks and preventive measures. Reducing risks from natural radiation also requires robust public awareness programs. Social media, radio, and television are powerful tools for educating the public about these risks and sharing valuable safety information. Effective communication strategies, particularly on global platforms [23], are necessary to raise awareness and reach a broader audience. Expanding access to education and awareness programs through diverse information-sharing channels is key.

To support technical progress and innovation, it's important to focus on developing and applying new technologies. Encouraging scientific innovation, along with organizational and industrial collaboration, can accelerate advancements and address emerging challenges. Finally, promoting collective dialogue and deeper understanding demands initiatives like group discussions and community programs. Education and training programs designed to build awareness can foster a shared understanding and facilitate meaningful discussions on common challenges related to radiation and public health. Public outreach programs [24], integration of radiation safety education [25] into school curricula, and collaboration with the media and local authorities play a vital role in creating an informed and vigilant society [26]. These initiatives will help address potential risks associated with natural radiation exposure, ensuring the overall well-being and safety of communities for sustainable development.

10 Conclusion

Managing natural radiation risks is crucial for protecting health and the environment. Regular monitoring and risk checks form the foundation of safety. They allow early detection of hazards and quick responses. Clear rules and public awareness build a culture of preparedness and resilience. Success depends on teamwork between leaders, scientists, and the public. Working together ensures a strong, unified approach to managing these risks. This effort is vital for current safety and for supporting sustainable development. It ensures future generations can live safely alongside natural radiation.

References

[1] World health Organization International Agency for research on cancer IARC Monographs on the Evaluation of Carcinogenic Risks to Humans. Ionizing Radiation, Part 1: X- and Gamma (γ)-Radiation, and Neutrons VOLUME 75, This publication represents the views and expert opinions of an IARC Working Group on the Evaluation of Carcinogenic Risks to Humans, which met in Lyon, 26 May–2 June 1999 2000.

[2] Technical Reports Series No. 419 International Atomic Energy Agency Vienna, 2003.

[3] ICRP, 2019. Radiological protection from naturally occurring radioactive material (NORM) in industrial processes. ICRP Publication 142. Ann ICRP 48(4).

[4] Glen F. Knoll, Radiation Detection and Measurement, 4th Edition; ISBN-10. 9780470131480 · ISBN-13. 978-0470131480 · Edition. 4th · Publisher. John Wiley & Sons Inc · Publication date. 24 September 2010.

[5] Environmental Health Perspectives Vol.91, pp.45-48,1991, Radiation Dosimetry by John Cameron.

[6] R Prasad, NUCLEAR PHYSICS: R Prasad; ISBN-10. 9789332522657 · ISBN-13. 978-9332522657 · Edition. 1st · Publisher. Pearson Education India (2014).

[7] Applied Radiation and Isotopes, Volume 187, September 2022, 110344, Applied Radiation and Isotopes, Study of alpha spectrometry for detection of radon and progeny using gas microstrip detector; Mehdi Hassanpour a, Parvin Dehghanipour b, Mohammadreza Rezaie c, Marzieh Hassanpour a, Mohammad Rashed Iqbal Faruque a, Mayeen Uddin Khandaker

[8] Q. Zhang, Y. Zhao, C.H. Xu, 238U radioactivity distribution in soils in the Beijing-Tianjin-Hebei region, Chin J Radiol Med Prot, 35 (9) (2015), pp. 692-695.

[9] Q.H. Meng, Y.Z. Ma, H. Wang, et al. Monitoring and analysis of radioactivity in soils in Beijing during 2017-2018, Chin J Radiol Med Prot, 40 (9) (2020), pp. 702-706, Radiation Medicine and Protection, Volume 3, Issue 4, December 2022, Pages 171-174

[10] Jiaying Wang, Yu Chen, Zhongjian Ma, Lu Zhang Zhen Zhang; "Radiation Medicine and Protection, Analysis of gamma-emitting radionuclides in soils around high energy accelerators"; Volume 3, Issue 4, December 2022, Pages 171-174

[11] R. M. Singru; "Introduction to Experimental Nuclear Physics" Wiley Eastern Private Limited, New Delhi (1972): SBN-13 978-0852268216

[12] W. R. Leo; William R. Leo, Techniques for Nuclear and Particle Physics Experiments: A How-to Approach; Springer-Verlag Berlin Heidelberg GmbH; (1994)

[13] C. L. GREENSTOCK and A. TRIVEDI, Prog. Biophys. molec. Biol., Vol. 61, pp. 81-130, 1994 1994 Elsevier Science Ltd Printed in Great Britain 0079 o107/94, title: , BIOLOGICAL AND BIOPHYSICAL TECHNIQUES TO ASSESS RADIATION EXPOSURE: A PERSPECTIVE

[14] Cardona, O.D., M.K. van Aalst, J. Birkmann, M. Fordham, G. McGregor, R. Perez, R.S. Pulwarty, E.L.F. Schipper, and B.T. Sinh, 2012: Determinants of risk: exposure and vulnerability. In: Managing the Risks of Extreme Events and Disasters to Advance Climate Change Adaptation

[15] Field, C.B., V. Barros, T.F. Stocker, D. Qin, D.J. Dokken, K.L. Ebi, M.D. Mastrandrea, K.J. Mach, G.-K. Plattner, S.K. Allen, M. Tignor, and P. M. Midgley (eds.)]. A Special Report of Working Groups I and II of the Intergovernmental Panel on Climate Change (IPCC). Cambridge University Press, Cambridge, UK, and New York, NY, USA, pp. 65-108.

[16] Scott Samuel A. Health impact assessment—theory into practice. J. Epidemiol Community Health 1998; 52:704-5] [United Nations conference on environment and development. The earth summit (agenda21). Rio de Janeiro: United Nations,1992.] [Asian Development Bank. Guidelines for the health impact assessment of development projects. Environmental Paper No 11. Manilla: ADB,1992.

[17] Kashif Abbass1 · Muhammad Zeeshan Qasim · Huaming Song, Muntasir Murshed, Haider Mahmood, Ijaz Younis ; A review of the global climate change impacts, adaptation, and sustainable mitigation measures, Environmental Science and Pollution Research (2022) 29:42539–42559, https://doi.org/10.1007/s11356-022-19718-6].

[18] Francisco J. Tovar-Lopez. Review article "Recent Progress in Micro- and Nanotechnology-Enabled Sensors for Biomedical and Environmental Challenges, Sensors 2023, 23(12), 5406

[19] Madhusudan B. Kulkarni, Narasimha H. Ayachit and Tejraj M. Aminabhavi; Biosensors 2022, 12, 892, Review: Recent Advancements in Nano biosensors: Current Trends, Challenges, Applications, and Future Scope.

[20] Kovalchuk I, Abramov V, Pogribny I, Kovalchuk O. Molecular aspects of plant adaptation to life in the Chernobyl zone. Plant Physiol. 2004 May;135(1):357-63. doi: 10.1104/pp.104.040477. Epub 2004 May 7. PMID: 15133154; PMCID: PMC429389.

[21] Synergistic Training program Utilizing the Scientific and Technological Infrastructure (STUTI); DST, Government of India: https://www.dststutitraining.com/aligarh-muslim-university/index

[22] B. P. Singh: "Historical Perspective and Applications of Nuclear Radiation," Vigyan Pragati (ISSN 0042-6075), Volume 71-72(05), May 2023, pp. 15-23. Published by the National Institute of Science Communication and Information Resources (NIScIR), a CSIR, New Delhi (Hindi Magazine).

[23] B P Singh; "REPORT on Science Awareness Week at AMU"; "Science Reporter", published by National Institute of Science Communication and Policy Research (NIScPR), Council of Scientific & Industrial Research (CSIR), New Delhi, Vol. 59 No. 7 (July 2022) Pg. 48-49.

[24] B. P. Singh, M. Wasi Khan and Jai Prakash; COMPANDIUM; Synergistic Training program Utilizing the Scientific and Technological Infrastructure (STUTI); submitted to DST, Government of India; (2023) (Unpublished).

[25] B. P. Singh "Nuclear radiations and their applications"; School Science: A quarterly Journal of Science Education; Vol.61; No.2 and 3, June-September 2023. NECRT, New Delhi.

[26] B. P. Singh: "Nuclear Energy Dynamics: Balancing Policy Imperatives and Public Sentiments - Insights from a Survey," Popular Science Magazine - Vigyan Setu e-Magazine, Year 4, Issue 2, April-June 2024.

Measurement of Beta Energy Spectrum of ^{90}Sr source using Magnetic Deflection Method and a GM Counter

Mohd Shuaib, Aquib Siddique, M Shariq Asnain and B P Singh
Department of Physics, Aligarh Muslim University, Aligarh, UP, India-202002

1 Introduction

Radioactive decay is a phenomenon where the unstable atomic nuclei release energy to become stable [1]. Some nuclei are unstable because they have an uneven balance of protons and neutrons, which creates excess energy. To fix this imbalance, they emit nuclear particles or radiation. There are several types of radioactive decay, including alpha decay, beta decay, gamma decay, positron emission (beta-plus decay), and electron capture. In case of an alpha decay, generally, the heavy nucleus loses two protons and two neutrons by releasing an alpha particle, which reduces its charge and mass both. On the other hand, beta decay takes place, when a neutron inside the nucleus is converted into a proton or a proton into a neutron, emitting a beta particle, either an electron (β^-) or a positron (β^+). In positron decay, a proton turns into a neutron, releasing a positron and a neutrino, and occurs mostly in proton-rich nuclei. In β^- decay, a neutron turns into a proton, releasing an electron and an antineutrino, and occurs in neutron-rich nuclei. The β^+ decay requires extra energy (1.022 MeV) and competes with electron capture, while β^- decay has no such requirement and is more common in nature. Both the beta decays involve the weak nuclear force, energy release, and the emission of neutrinos.

Another type of common decays is electron capture (EC) decay which leaves the similar residues as in case of positron decay, and hence both compete with each other. The gamma decay is entirely different, as it doesn't change the particles inside the nucleus but instead releases excess energy in the form of high-energy radiation called gamma rays. Other types, like neutron emission and spontaneous fission, are less common but still important and studied in nuclear physics. The study of beta decay is interesting because it gives us information about the behaviour of atomic nuclei. Measuring the energy of these beta particles is important in areas like nuclear medicine [2], where it helps in imaging and treatment, and in particle physics, where it helps us understand the fundamental forces.

In natural radioactive decay, the energy spectrum of beta particles is continuous, because the total decay energy is shared between the beta particle and the neutrino [3]. This creates a characteristic continuous spectrum shape. The spectrum peaks at intermediate energies and falls off toward the maximum energy, referred to as the end point energy. A typical energy spectrum of beta particles observed in natural radioactive decay is shown in Fig. 1.

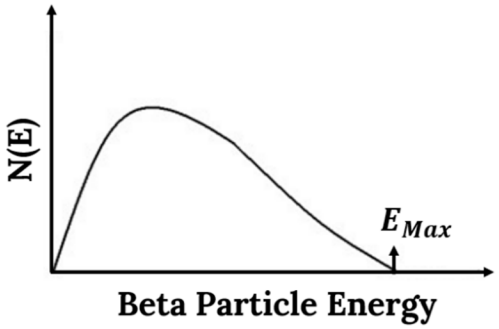

Fig. 1: *A typical beta particle energy spectrum obtained in natural radioactive decay.*

To measure this type of energy spectrum is quite challenging due to the continuous distribution. The involvement of high-speed particles, indicate the need for precise instrumentation to distinguish energies accurately. Gas-filled detectors, like Geiger-Müller (GM) counters, are generally not used for measuring the energy of beta particles. The GM detectors provide only a count of particle events, without distinguishing the energy of individual beta particles. To measure the energy accurately, the techniques, like magnetic deflection, are required. By using a magnetic field to bend the paths of these particles, it is possible to determine their energy and create a beta particle spectrum. This method combines magnetic deflection with principles of relativity for precise results. The experiment was carried out in the Nuclear Physics Laboratory using advanced techniques to explore the details of such nuclear decay.

When beta particles are emitted from a radioactive source, they travel with a certain energy or velocity in all possible directions. However, when these particles pass through a magnetic field, they experience a force due to their electric charge. This force causes the beta particles to move in a curved path. The radius of curvature of path depends on their velocity, the strength of the magnetic field, and the

charge and mass of the particle. In this experiment, the magnetic deflection method has been adopted. The beta particles emitted from a radioactive source are subjected to a magnetic field. By adjusting the magnetic field strength, it is possible to measure the energy of the beta particles.

2 The Force Balancing Equation

The fundamental principle behind this setup lies in the balance of forces acting on the beta particles. When a charged particle like an electron moves through a magnetic field, the magnetic force provides the necessary centripetal force to keep the particle moving in a circular path. The force balance is given by the equation:

$$evB = \frac{mv^2}{r} \tag{1}$$

where e is the charge of the beta particle (the electron charge), v is the velocity of the beta particle, B is the magnetic field strength, m is the mass of the beta particle (the electron), and r is the radius of curvature of the path of beta particle.

The expression indicate that the velocity of the beta particle is directly related to the radius of curvature and the magnetic field strength. By measuring the radius and knowing the magnetic field, we can calculate the velocity of the beta particle. However, this relationship assumes that the beta particles are non-relativistic, which is only accurate for low-energy emissions.

3 Transition to Relativistic Kinematics

In general, the beta particles emitted during natural radioactive decay typically have energies in the range of 0.3 MeV to 2.5 MeV, corresponding to velocities greater than 95% of the speed of light (v>0.95c). This means that, for accurate energy measurements, we need to account for relativistic effects, because the particles are having energies that corresponds to the speeds that are significant fractions of the speed of light.

To properly describe the motion of these high-energy beta particles, we generally use the relativistic energy-momentum relation, given as;

$$\frac{E^2}{c^2} = p^2 + m_o^2 c^2 \tag{2}$$

where, E is the total energy of the particle, p is the relativistic momentum, m_0 is the rest mass of the electron and c is the speed of light. From this, the total energy E of the particle is the sum of its kinetic energy and its rest mass energy;

$$E = E_{Kinetic} + m_o c^2 \tag{3}$$

where $E_{Kinetic}$ is the kinetic energy, and m_0c^2 is the rest mass energy of the particle. Using the relativistic expression for momentum, we can rewrite the kinetic energy $E_{Kinetic}$ as:

$$E_{Kinetic} = \sqrt{(eRB)^2 + (m_o^2 c^4)} - m_o c^2 \tag{4}$$

This equation takes into account both the speed of the beta particles and the strength of the magnetic field. This helps us to accurately get the kinetic energy of the emitted beta particles.

4 Calibration of the spectrometer Setup

To relate the magnetic field strength with the kinetic energy of the beta particles, we set a fixed radius of curvature for the particle path. For this purpose, we use a typical chamber where only the particles moving at a given radius of curvature will reach the detector. In the present experiment, conducted in the Nuclear Physics Laboratory, the path radius is fixed at 50 mm. This allows us to vary the magnetic field strength, and for each value of B, we can calculate the corresponding kinetic energy of the beta particles using the above relativistic formula (Eq. 4). A calibration curve relating the energy of the beta particles for different strengths of magnetic field required to bend them at the same radius of curvature *r=50 mm* and deduced from above expression is plotted in Fig. 2.

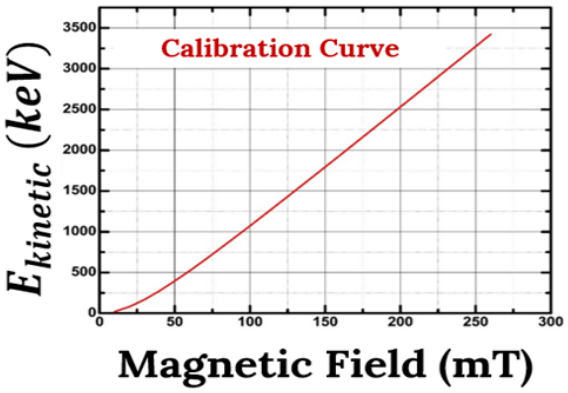

Fig. 2: *Calibration curve of the spectrometer with the relation between magnetic field and corresponding beta particle energy derived from the relativistic equation.*

A Hall probe is used to measure the strength of magnetic field inside the chamber. A typical picture of the hall probe used is shown in Fig. 3. This Hall probe is inserted inside the chamber to determine the strength of magnetic field.

Fig. 3: *Axial Hall probe used for measuring magnetic field.*

When, a current flow through a conductor placed perpendicular to a magnetic field. The field causes charge carriers (electrons) to accumulate on one side of the conductor, creating a voltage difference called the Hall voltage (V_H). The Hall voltage is directly proportional to the magnetic field strength (B).The strength of magnetic field B, can be calculated using the expression:

$$B = \frac{V_H.I}{q.d} \tag{5}$$

where V_H is the Hall voltage, I is the current, q is the charge of the carrier (typically the electron charge), and d is the thickness of the conductor.

Thus, by varying the strength of the current in the electromagnet coil, the magnetic field is varied. This method provides a precise measurement of the magnetic field strength, commonly used in laboratory experiments.

As already mentioned, before counting the beta source, a calibration curve is created by plotting the magnetic field strength against the calculated kinetic energy for each value of B (using Eq. 4). As can be seen from this curve, a relatively stronger field is required to bend high-energy beta particles in order to keep them at the same radius of curvature, i.e., 50 mm. This curve (Fig. 2) is used as a reference, allowing us to determine the energy of beta particles for any given magnetic field.

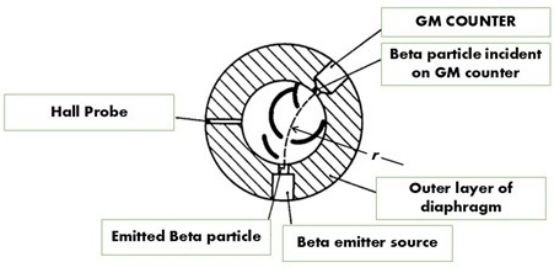

Fig. 4: *Experimental setup for measuring the Beta Particle energy.*

The beta particle spectrum of ^{90}Sr have been measured in the experiment carried out using the beta ray spectrometer setup in the Nuclear Physics Lab of the department. The decay scheme of ^{90}Sr source is shown in Figure 5 [4]. As shown in this figure, when ^{90}Sr undergoes beta decay to form ^{90}Y, the maximum energy released in the process is about 0.544 MeV. The emitted beta particle (electron) and the antineutrino sharing this energy. The energy of the emitted beta particles ranges from 0 to 0.544 MeV, with the maximum energy corresponding to the full available energy from the decay. Similarly, ^{90}Y decays via beta decay to form stable ^{90}Zr, with a maximum energy release of 2.27 MeV. In this case also, the energy is shared between the emitted beta particle and the antineutrino, with the energy of the beta particles ranging from 0 to 2.27 MeV.

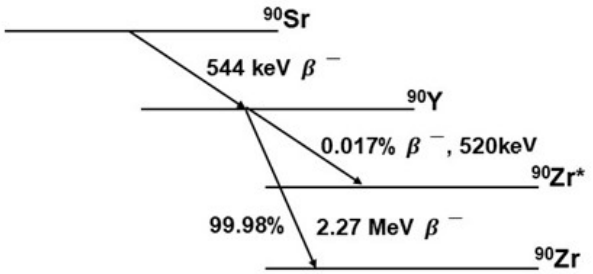

Fig. 5: *Decay scheme of ^{90}Sr source.*

In the present experiment, the beta particles emitted from the ^{90}Sr radioactive source are allowed to pass through a magnetic field. For this purpose, a pencil type source of ^{90}Sr is used. The strength of the magnetic field is varied by changing current in the electromagnet coil. The radius of curvature of the particles' paths is fixed at 50 mm, by using a specially designed chamber (Fig.4). The magnetic field strength is varied systematically so that beta particles of different energies reach at the detector at the same radius of curvature. As the magnetic field strength is adjusted, the beta particles of different energies are allowed to pass through at the same radius of curvature. The number of beta particles that reach the detector is measured using an end window GM counter placed at the other end of the chamber setup (see Fig. 4). An end-window Geiger-Müller (GM) counter is a special type of GM counter designed for detecting ionizing radiation, particularly beta particles. Unlike standard GM counters that typically have a window at the side of the tube, the end-window GM counter has a window at the end of the tube. The window is often made up of a thin, transparent material like mica. This specific design allows the low energy beta particle to enter and reach the active volume of the detector. A photograph of the experimental setup in the lab is given in Fig. 6.

The tube is filled with a low-pressure argon gas. When ionizing radiation (such as beta particles) passes through the window, it ionizes the argon gas present inside. The resulting free electrons and ions are collected at respective electrodes due to strong electric field generated by an applied voltage. The collected charges when pass through a load resistance generate a voltage pulse that is counted and analysed. The end-window design makes it particularly sensitive to low-energy beta particles, as the thin window allows these particles to pass through with minimal attenuation. Thus, by recording the number of counts at different magnetic field strengths, it is possible to obtain the beta particle energy spectrum.

Fig. 6: *A photograph of experimental arrangement.*

5 Data Collection and Results

For data collection, the source and detectors are placed at their respective positions as shown in Fig. 4. The current in the electromagnet coil is varied to change the magnetic field. For each current value, the magnetic field is measured, and the corresponding counts are recorded using the GM counter. For each magnetic field strength, the corresponding energy of the beta particles is determined from the calibration curve (Fig. 2). Using this calibration curve, the magnetic field values are converted to energy.

6 Analysis of the Measured Beta Particle Energy Spectrum

Using this data, a plot of beta energy versus counts is generated to obtain the beta energy spectrum. The measured energy spectrum of the beta particles emitted from ^{90}Sr source is shown in Fig. 7. The energy spectrum typically exhibits a peaked distribution, with a sharp increase in counts at lower energies, and followed by a gradual decrease as the energy increases. This behaviour is expected from the continuous spectrum of beta decay. Here the emitted beta particles have a range of energies. Towards the high-energy side of the spectrum, the end point energy can be observed. The end point energy is the energy difference between the initial and final states of the nucleus, minus the energy carried away by the emitted neutrino. The fall-off at higher energies is a direct consequence of the statistical distribution of energy between the electron and the antineutrino during the decay. The number of counts detected at each energy also reflects the detection efficiency of the GM counter setup.

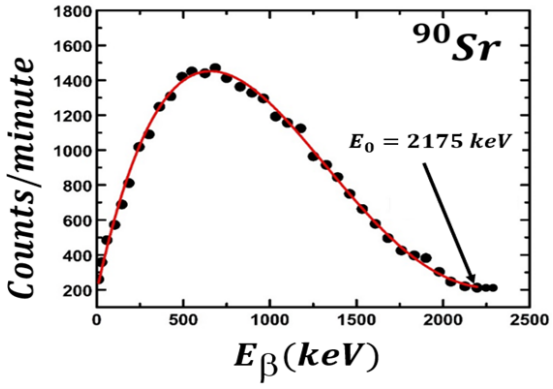

Fig. 7: *Experimentally obtained β particle spectrum of ^{90}Sr.*

The analysis of the spectrum also provides a confirmation of the relativistic energy formula, which governs the behaviour of the beta particles emitted during decay. The varying magnetic fields used in this experiment and the corresponding changes in the detected energy are consistent with the predictions of relativistic kinematics. The measurement of the energy spectrum also serves as a powerful validation of the Fermi theory of beta decay. The magnetic field values and corresponding energies observed in the spectrum agree well with the expected values, confirming that the calibration curve accurately reflects the actual energy of the beta particles.

This measured energy spectrum, along with the calibration curve and relativistic formulations, provides an essential tool for the study of beta spectrum.

References

[1] Arthur Beiser, *Concepts of Modern Physics*, McGraw Hill Education, 6^{th} Edition (2002).

[2] Evelina Miele *et al.,* Journal of Experimental and Clinical Cancer Research, Vol. 27, Article number: 52 (2008).

[3] H. A. Enge, *Introduction to Nuclear Physics*, Wesley Publishing Company (1966).

[4] E. Browne and R. B. Firestone, *Table of Radioactive Isotopes*, Wiley, New York, (1996).

Comprehensive Measurement of Target Thickness Using Rutherford Backscattering Spectrometry (RBS)

Aquib Siddique, M. Shariq Asnain, Mohd Shuaib and B. P. Singh
Department of Physics, Aligarh Muslim University, Aligarh, UP, India-202002

In various scientific experiments, accurate measurement of the thickness of thin foils is essential. This is particularly important in fields like material science, nuclear physics, and semiconductor technology, where precise thickness of the sample is required for understanding the properties and behaviour of materials and/or to study the reaction dynamics. Out of the various techniques available for thickness measurement, Rutherford Backscattering Spectrometry (RBS) is one of the most reliable and powerful methods. This technique provides both the precision and depth profiling capabilities. In this article, we present a detailed methodology for measuring the thickness of thin substrate aluminum (Al) and thin ytterbium (Yb) material deposited on it. We have used both the α-transmission method and RBS.

1 Introduction

Accurate determination of sample foil thickness is essential for getting good quality data in various experiments. The thickness of these materials plays a critical role in the success of the experiments, as it can directly influence the measurement accuracy and the interpretation of results. Several methods are available for thickness measurement, each offers distinct advantage and may have limitations depending on the specific requirements of the experiment. The common methods for thickness measurements used generally, for nuclear physics experimentation are the simple weighing method and the α-transmission method [1]. However, in recent years with the availability of dedicated low energy accelerators the Rutherford Backscattering Spectrometry (RBS) [2] has become very popular and effective. These techniques not only provide accurate thickness of the material foil but also allows for the analysis of its composition and structural properties. As such, the RBS has become an indispensable in nuclear physics experiments and material characterization.

In nuclear physics experiments, especially those focused on studying reaction dynamics, measuring nuclear reaction cross-sections experimentally is the basic requirement. The measurements involve bombarding an incident ion beam, produced by a particle accelerator, onto a thin target material. The emitted nuclear particles and/or gamma radiations are detected with the help of suitable nuclear radiation detectors. The data is then analysed within the framework of theoretical models to get information about the reaction dynamics or to get information about the structure of the nuclei under study. If the target is too thick or too thin, it can lead to erroneous data. As such, accurate thickness measurement is an essential requirement in such experiments.

Recently, we conducted an experiment at the Pelletron facility of the Inter-University Accelerator Centre (IUAC), New Delhi, focusing on the nuclear system ^{16}O + ^{174}Yb [3]. The objective of the experiment was to study the fusion and break-up fusion reaction cross-sections of radioactive residues generated as a result of the interactions. Analysis of the reaction cross-sections of these residues as a function of energy provides information about the reaction dynamics involved.

Isotopically enriched ^{174}Yb ($\approx$ 97%) in oxide form ($^{174}Yb_2O_3$) was used as the target material, with thicknesses ranging from $\approx$ 0.4 to 1.0 mg/cm^2. These targets were prepared using the vacuum evaporation technique. The melting point of ytterbium oxide is 2355°C, and the deformation parameter (β_2) of ^{174}Yb is 0.332. To support the enriched material, self-supporting aluminum catcher foils were used. The aluminum foils, with thicknesses of $\approx$ 0.8-1.5 mg/cm^2, were prepared using a high-pressure rolling machine. The target material ($^{174}Yb_2O_3$) was then deposited onto the aluminum substrate using a high-vacuum evaporator system [4]. In this experiment, precise thickness measurement of both the aluminum foil and the deposited ^{174}Yb layer was critical. The thickness of the target is essential not only for ensuring proper interaction between the ion beam and the target but also for evaluating the quality and uniformity of the enriched material. This makes the thickness measurement, a crucial aspect of the experimental setup.

In the following sections, we will discuss the details of the thickness measurement techniques employed in our recent experiments conducted at IUAC, New Delhi. These methods were instrumental in deter-

mining the exact thickness of the target materials, ensuring the accuracy and success of the experiments.

Fig. 1: *Vacuum Chamber use in the experiment for determination of thickness.*

2 α-Transmission Method for Preliminary Thickness Measurement

This experiment uses a specialized vacuum chamber (Fig. 1) to create a controlled, air-free environment for studying alpha particles emitted by a ^{241}Am (Americium-241) source (Fig. 2). The cylindrical chamber, with an 8 cm diameter and 14 cm height, ensures uniform pressure distribution, essential for accurate energy measurements. A rotary pump (Fig. 3) evacuates air to maintain a near-perfect vacuum. Alpha particles are detected using a surface barrier detector (Fig.4), which converts their energy into electrical signals for analysis. Calibration with known sources ensures precision.

Fig. 2: *The ^{241}Am as alpha emitting source available in the nuclear laboratory.*

The α-transmission method is widely used for measuring the thickness of thin materials, particularly foils. The principle behind this method is straightforward: as α particles pass through a material, they lose energy due to interactions with the atoms of the material. The amount of energy lost by the α particles is directly related to the thickness of the material through which they pass. So, by measuring the energy loss ΔE, of alpha particles while passing through the target foil, and then using the stopping power, dE/dx value, one can determine the thickness of the foil. A typical expression in this regard is given below;

$$\Delta x = \Delta E/(dE/dx) \tag{1}$$

In the present work, a ^{241}Am source emitting α particles of energy 5.486 MeV was used to measure the energy loss in the prepared sample. The method involves detecting the energy loss of α particles as they traverse the material, which enables the determination of the sample thickness. For the aluminum catcher foils used in this experiment, the thickness was measured before the deposition of ytterbium (Yb) material. Here energy of α-particles from the ^{241}Am source are measured with and without the sample. The difference of energy gives the energy loss in the sample foil thickness. Once the Yb material was deposited on the aluminum foil, the thickness of the Yb layer was measured by analysing the energy loss of α-particles passing through the layer. The method provides a quick and efficient measurement of the thickness. However, it only gives a one-dimensional measurement along the path of the α particles. Though, this is sufficient for many applications, but a better precision can be achieved by using the RBS technique.

Fig. 3: *The Rotary oil pump of "VALUE" make with flow rate 51 Litre/min with $\frac{1}{4}$ HP.*

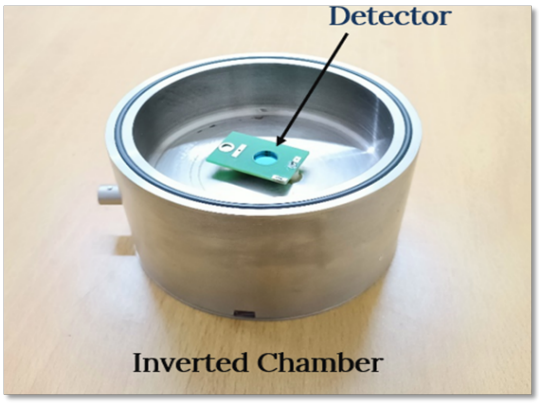

Fig. 4: *Photograph of the silicon surface barrier detector inside the vacuum chamber taken in the nuclear laboratory.*

3 Rutherford Backscattering Spectrometry (RBS) for Accurate Thickness Measurement

As already mentioned, the α-transmission method gives a good and first estimate of foil thickness. The Rutherford Backscattering Spectrometry (RBS) is an advanced and precise method of measuring thickness, especially when dealing with layered materials. The RBS also gives additional information, like the depth distribution of atoms in a material, which is sometimes useful for analyzing multilayer structures.

As a matter of fact, the RBS was developed in the early 1950s by Ernest Rutherford and his colleagues, who discovered the process of backscattering when bombarding a target with energetic α-particles. Rutherford's pioneering work led to the understanding of structure of atomic nucleus and also the development of techniques that helps in probing the surface and structure of materials. The breakthrough in RBS came with the ability to analyze the backscattering of α-particles from a thin film. This provides a method to measure the composition and thickness of materials with a depth resolution. The method quickly gained popularity as a non-destructive, high-precision tool for studying thin films and layered materials.

In this study, the Pelletron Accelerator for RBS-AMS System (PARAS) at the Inter-University Accelerator Centre (IUAC) in New Delhi, India, was used to perform the RBS measurements. This facility is equipped with a 1.7 MV 5SDH-2 Pelletron accelerator, which generates a 2 MeV α-particle beam directed normal to the surface of the Al-backed $^{174}Yb_2O_3$ target. The energetic α-particles interact with the target material, and are scattered off the atoms in the sample and losing energy in the process.

Fig. 5: *RBS facility at IUAC New Delhi.*

An important part of the experiment was the use of the Alphatross ion source, which produces negatively charged helium (He) ions. These ions were accelerated and directed onto the target material. The backscattered α-particles, after interacting with the sample, were detected using a Silicon Surface Barrier Detector (SSBD) which is kept at 166^o with respect to the beam direction. The inside view of the RBS setup is shown in Fig. 6. A Silicon Surface Barrier Detector (SSBD) is a type of semiconductor detector used generally in nuclear physics for detecting charged particles, like α and β particles, as well as ions. It is made up of a thin layer of high-purity silicon with a potential barrier just at the surface working as a junction. When a charged particle enters the detector, it creates electron-hole pairs in the silicon. The current produced as a result of collection of electron-hole pairs is measured to identify and analyse the particle's energy. The SSBDs have high resolution, compact size, and fast response time, making them ideal for particle spectroscopy and radiation detection. This detector is sensitive to the energy and intensity of the backscattered ions. The data collected can be used to infer the elemental concentration and thickness distribution of the materials in the target.

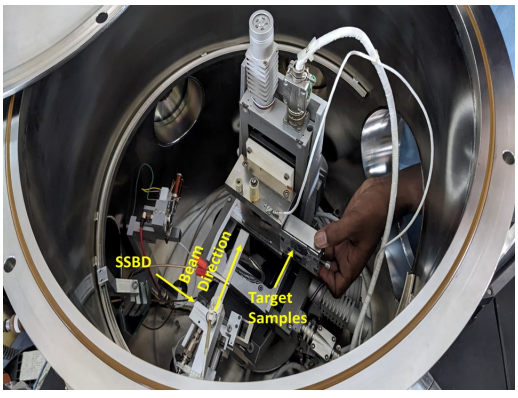

Fig. 6: *Inside view of the RBS setup at IUAC, New Delhi.*

3.1 RBS Spectrum Analysis

A typical measured RBS spectrum for one of the $^{174}Yb_2O_3$ samples is shown in Fig. 7. The spectrum reveals several key features. The prominent peak between channel numbers 1500 and 1840 corresponds to the energy of backscattered α-particles from the Yb layer, confirming the presence of ytterbium in the material. A smaller yield at lower channels represents the backscattering of α-particles from the aluminum substrate behind the Yb layer. This distinction is crucial for ensuring that the RBS measurement accurately captures both the thickness of the Yb layer and the substrate. Through this method, the depth of the Yb material and its interaction with the α-particles can be determined, leading to precise measurements of both the total target thickness and the composition of the layers within the target.

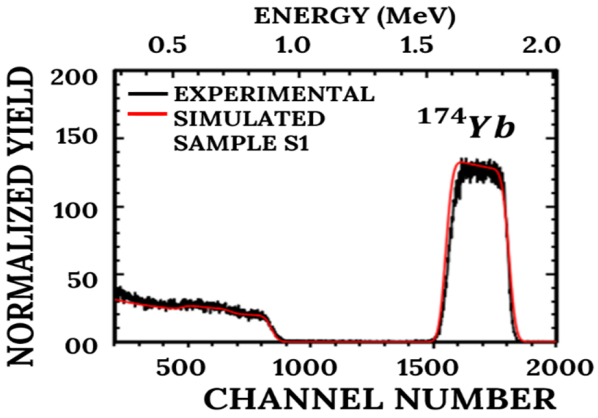

Fig. 6: *The RBS spectrum obtained for one of the samples of ^{174}Yb in RBS method.*

The Rutherford Universal Mass Program (RUMP) is a widely used simulation tool designed for analyzing Rutherford Backscattering Spectrometry (RBS) spectra. It is a sophisticated software that models the depth profile of materials in a sample by simulating the interaction of incident ions (usually α-particles) with the atoms in the target material. The primary goal of RUMP is to solve the inverse problem of RBS, where the material composition and thickness distribution are inferred from the experimental backscattering data. By adjusting material properties such as thickness and composition, RUMP iteratively fits the simulated spectrum to the experimental data.

RUMP operates by first taking an initial guess of the sample's structure and composition, including the number of layers, materials, and their thicknesses. It then simulates the scattering of incident ions using well-established physical models, such as the Rutherford scattering cross-section and the energy loss of ions in the material. The simulated spectrum is compared with the experimental data, and the software iterates to adjust the model parameters until a good fit is achieved. This iterative process allows RUMP to determine the distribution of elements and the thicknesses of different layers in a multi-layered sample.The core mathematical formulation used in RUMP involves Rutherford scattering and ion interactions with materials. The Rutherford scattering cross-section, which determines the probability of a backscattering event, is described by the Rutherford formula:

$$\frac{d\sigma}{d\Omega} = \left(\frac{Z_1 Z_2 e^2}{4\pi\epsilon_o E}\right)^2 \frac{1}{sin^4(\theta/2)} \tag{2}$$

This formula calculates the angular distribution of scattered ions based on the energy of the incident particles and the atomic numbers of the projectile and target materials. In addition to the Rutherford scattering model, RUMP also uses stopping power equations to account for the energy loss of ions as they pass through the material. One commonly used model for this is the Bethe-Bloch formula, which estimates the rate of energy loss per unit distance traveled:

$$\frac{dE}{dx} = \frac{4\pi N_A e^4 Z^2}{mv^2} ln\left(\frac{2mv^2}{l}\right) \tag{3}$$

This equation helps simulate how much energy the incident ion loses in the material, which is critical for accurately determining the depth at which ions scatter and providing reliable backscattering spectra.

Once the RBS data is collected, RUMP uses the simulated spectra to extract the material properties, such as layer thickness and composition. The program calculates the expected backscattering yield from each layer in the sample based on its thickness, material composition, and the scattering events. By fitting these simulated spectra to the experimental data, RUMP derives the precise material profile of the sample. The iterative adjustment process continues until the calculated and experimental spectra match, providing the final results for the thickness and composition of each layer.

In practical applications, RUMP has been used to analyse complex multi-layer samples, such as a system involving an enriched ytterbium (Yb) layer deposited on an aluminum (Al) foil. In this case, RUMP was employed to extract the thicknesses of both the Yb layer and the underlying aluminum substrate from the experimental RBS spectrum. The experimental data revealed backscattering signals from both the Yb and Al layers. By adjusting

the model parameters (thickness and composition), RUMP successfully matched the simulated spectra to the experimental results, as shown by red curve in Fig. 7. This process yielded consistent results that were in agreement with those obtained using the α-transmission method, further validating the accuracy of both techniques.

4 Comparison of results of α-Transmission and RBS Methods

The thickness measurements obtained using both the α-transmission and RBS methods were found to be in good agreement (Table 1). The α-transmission method, though less complex, provided a quick estimate of the foil thickness, while the RBS technique offered more detailed information, including the depth profiling of the material and the elemental composition.

Table 1: *Comparison of the thickness measurements of Yb material using α-transmission method and RBS method.*

Samples	**Thickness Measurements of Yb Material**	
	α-transmission method (μg/cm^2)	RBS Method (μg/cm^2)
S1	437	450 $\pm$ 9
S2	541	550 $\pm$ 7

The RBS method is especially useful in scenarios where multilayered structures or complex compositions are involved, as it provides depth-resolved information that the α-transmission method cannot. In this experiment, RBS not only validated the thickness measurement of the Yb material but also provided valuable insight into the structure of the target material.

5 Conclusions

In this study, we used the α-transmission method and Rutherford Backscattering Spectrometry (RBS) to measure the thickness of aluminum (Al) and ytterbium (Yb) target foils. Both methods provided consistent and reliable measurements, with RBS offering more detailed compositional and depth-resolved information. The complementary use of these techniques ensures high confidence in the accuracy of the measurements and enhances our understanding of the material's structure.

The combination of α-transmission and RBS is especially valuable in experiments that require high precision and detailed analysis of thin films or layered materials. The successful application of these methods highlights their importance in the precise measurement and characterization of thin foils, and their ability to provide complementary data that is essential for furthering research in these domains.

References

[1] C Yalcin, J. Phys.: Conf. Ser. **590**, 012050 (2015).

[2] Jaques Perrière, Vacuum **37**, 429 (1987).

[3] Aquib Siddique *et al.,* Phys. Rev. C **110**, 064605 (2024).

[4] S. R. Abhilash and D. Kabiraj, Proceedings of the DAE-BRNS Symp. on Nucl. Phys, Vol. 61, pp1062, (2016).

Notes on Fundamentals of Lasers

Mubashshara Fatma and Haris Kunari
Department of Physics, Aligarh Muslim University, Aligarh, UP, India-202002

The word 'LASER' is an acronym for the 'Light Amplification by Stimulated Emission of Radiation.' Its operation is based on the 'stimulated' or 'induced' emission phenomenon, which Albert Einstein first predicted in 1916 [1]. This prediction was paid little attention until the 1950s when Charles Townes and his colleagues developed a microwave amplifier (which they called a 'MASER' – an acronym for 'Microwave Amplification by Stimulated Emission of Radiation) using ammonia (NH_3) at Columbia University, New York [2]. In 1958, Arthur Schawlow and Charles Townes theoretically showed that the maser principle could be extended to the visible-infrared region [3], and the possibility of achieving lasing action in buffer gas discharges was given by John Sanders [4] and Ali Javan [5]. In 1960, Theodore Maiman made the first realization of a laser in the optical wavelength of $\lambda = 6943$ Å using ruby as the active medium [6]. In the following year, Javan and his co-researchers constructed the first gaseous He-Ne laser at the Bell Telephone Laboratories, New Jersey, USA [7]. The ruby laser is a three-level solid-state laser that operates in pulse mode; however, the gaseous He-Ne laser is a four-level system that produces a continuous light beam (CW mode). Since then, the lasing action has been obtained in a large variety of material systems (including solids, liquids, ionized gases/plasmas, fibers, dyes, and semiconductors) at different wavelength regions from infrared to x-rays.

In this article, we would like to describe the basic principles and processes related to lasers. We limit these discussions to typical three-level (ruby) and four-level (He-Ne) laser systems only, as these are part of the curriculum at undergraduate and postgraduate levels. We found that many students, irrespective of their levels, are still unclear or have misconceptions about the fundamentals of lasers and have difficulty in understanding the basic concepts behind them. Apart from these, we also notice that students' understanding of these basic lasers is limited to very naive energy level diagrams – for example, those of the He-Ne laser – therefore, we intend to provide an augmented energy level diagram for the same (see Section 5). In this article, we introduced the basic ideas and concepts of atomic and molecular physics to explain the underlying mechanism behind the laser.

1 Boltzmann Distribution

Consider a system containing discrete sets of energy levels with energies E_n, where $n = 1, 2, 3, ...$ and their corresponding degeneracies are denoted by g_n. For simplicity, the energy of ground level is taken to be $E_1 = 0$. Suppose the system contains N number of particles (atoms/molecules), then at absolute temperature $T = 0$ K (Kelvin), all particles in the system are occupied in the ground energy level, i.e., $N = N_1$. The thermal energy can excite atoms/molecules in the system, i.e., elevating them to the higher/excited energy level E_n with $n > 1$. If more thermal energy (i.e., higher the T) is applied to a system, the more would be populations in excited energy levels. At thermal equilibrium, the population of levels are described by the Boltzmann statistics:

$$\frac{N_n}{N_1} = \frac{g_n}{g_1}\ exp\left(\frac{-E_n}{k_B T}\right) \tag{1}$$

where k_B is the Boltzmann constant, and T is the thermodynamic temperature in the Kelvin (K) scale. For $T > 0$ K, the excited energy levels may get populated. It is evident from Eq. (1) that the higher the energy of the excited levels, the higher the temperature required to populate them. Generally, atomic systems have larger excitation energies than molecular systems, meaning it is easier to excite a system composed of molecules than atoms. Note that molecular energy levels are due to the combined effect of the electronic, vibrational, and rotational components [8]. Nevertheless, each of them has distinct energies: the electronic transitions are in the UV/visible (1 – 10 eV) spectral energy range, the vibrational ones are in the infrared (0.01 – 1 eV) range, and the rotation transitions are in the microwave (1 μeV – 10 meV) regions. In Fig. 1, the rotational, vibrational, and electronic energy levels and their populations are shown for a molecule. The energy separation between adjacent rotational levels $\Delta E = 3{\times}10^{-3}$ eV is the least; thus, its upper levels are significantly populated[1] at low temperature[2]

[1] This is a simplified case with $g_n = 1$, but the rotational level population strongly depends on the level degeneracies ($g_n = 2J + 1$, where $J = 0, 1, 2, 3, ...$, is the rotational quantum number). As a consequence of this, the population at lower rotational levels is not always higher [8].

[2] Temperature equivalent to 1 eV = 11604.51812 K.

$T = 30$ K, whereas those for vibrational levels with $\Delta E = 0.1$ eV is minimal – just one molecule is in the excited vibrational state – even when $T = 500$ K, and the electronic excited state of the molecule (almost equivalent to those of atomic excited states) with $\Delta E = 2$ eV is hardly populated. One can notice that the population at higher levels increases with increasing temperature, but it should be noted that Eq. (1) is a continuous function, meaning that lower energy levels are always more populated than higher ones. This indicates that the lasing action cannot occur under normal conditions between two arbitrary levels as no population inversion is achieved in the system.

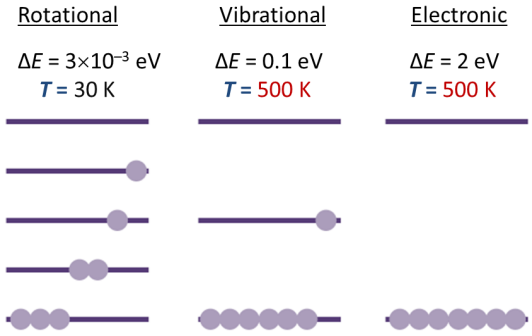

Fig. 1: *Boltzmann populations of Rotational, Vibrational, and Electronic energy levels of a molecule. Energy separation (ΔE, not shown on a single-uniform energy scale) between their levels is given on the top with their excitation temperature T (see text).*

Some special techniques are required to achieve population inversion in the medium irrespective of their types – molecular rotational, vibrational, or roto-vibrational, and molecular/atomic electronic states – and their distinct excitation energies (see Section 2 for more details). Indeed, the excitation techniques are different for different systems; for example, the molecular rotational or vibrational states can easily be excited by heat (thermal radiation) or small discharges; thus, such systems are suitable for masers, which amplify microwave or infrared radiation. Meanwhile, the excitation of the molecular/atomic electronic states requires optical or collisional (discharge) techniques; thus, such a system may give out the amplified light (laser) in the infrared to ultraviolet region.

2 Spontaneous and Stimulated Emission

Consider an ensemble comprises of a simple two-level system E_1 and E_2, with their respective population N_1 and N_2. Three fundamental processes – stimulated absorption, spontaneous emission, and stimulated emission – that occur between the energy levels are illustrated in Fig. 2.

The main difference between spontaneous and stimulated emission processes are the following:

- In spontaneous emission, the atoms/molecules randomly decay in time, producing photons with random phase correlation, direction, polarization, and total flux isotopically distributed.
- In stimulated emission, an external photon triggers or instigates the decay of atoms/molecules, thereby producing two photons with the same frequency, correlated phase, defined direction, and fixed polarization.

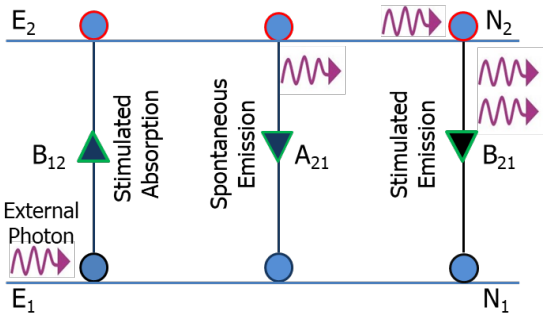

Fig. 2: *Stimulated absorption, spontaneous and stimulated emission of radiation (photon) with energy $h\nu = E_2 - E_1$ between two energy levels E_1 and E_2 with population N_1 and N_2. Their corresponding Einstein's coefficient are B_{12}, A_{21}, and B_{21}.*

The expressions for the rates of spontaneous and stimulated processes are the following:

$$\Gamma_{12}^{ab} = N_1 B_{12} \rho(\nu) \tag{2}$$

$$\Gamma_{21}^{sp} = N_2 A_{21} \tag{3}$$

$$\Gamma_{21}^{st} = N_2 B_{21} \rho(\nu) \tag{4}$$

where B_{12}, A_{21}, and B_{21} are Einstein's coefficients for stimulated absorption, spontaneous emission, and stimulated emission, respectively, and $\rho(\nu)$ is the spectral energy density of radiation at the frequency ν. In equilibrium, $\Gamma_{12}^{ab} = \Gamma_{21}^{sp} + \Gamma_{21}^{st}$, and the rearrangement of Eqs. (2−4) leads to the following:

$$\rho(\nu) = \frac{A_{21}/B_{21}}{(B_{12}/B_{21})(N_1/N_2) - 1} \tag{5}$$

At thermal equilibrium, the population N_1 and N_2 are described by the Boltzmann distribution (see Eq. (1)). Therefore, the above equation for a non-degenerate case (i.e., $g_1 = g_2 = 1$) leads to

$$\rho(\nu) = \frac{A_{21}/B_{21}}{(B_{12}/B_{21})\, e^{h\nu/k_B T} - 1} \tag{6}$$

Planck's radiation formula may be written in the form:

$$\rho(\nu) = G(\nu) \times h\nu \times \overline{n}(\nu) \tag{7}$$

where $G(\nu) = 8\pi\nu^2/c^3$ is the number of modes of vibrations per unit volume per unit frequency, $h\nu$ is the photon energy, and $\overline{n}(\nu)$ is the Bose-Einstein factor, which defines the thermal occupation number of a mode of a cavity. The Bose-Einstein factor takes the form:

$$\overline{n}(\nu) = \frac{1}{e^{h\nu/k_BT} - 1} \tag{8}$$

An immediate comparison of Eqs. (6) & (7) gives the following results:

$$\begin{aligned} B_{12} &= B_{21} \\ \frac{A_{21}}{B_{21}} &= \frac{8\pi h\nu^3}{c^3} \end{aligned} \tag{9}$$

Note that the refractive index of the medium is taken as unity here, and the above Einstein relations are strictly valid if the medium is optically isotropic. Now, we can draw some mathematical conclusions for the above equations, for which we need to calculate the ratio of stimulated to spontaneous emission from Eqs. (3) & (4).

$$\frac{\Gamma_{21}^{st}}{\Gamma_{21}^{sp}} = \frac{B_{21}\rho(\nu)}{A_{21}} \tag{10}$$

This ratio must be greater than unity for stimulated emission to exceed spontaneous emission. Substitution of the results from Eqs. (7) & (9) further simplifies the above relation to

$$\frac{\Gamma_{21}^{st}}{\Gamma_{21}^{sp}} = \overline{n}(\nu) \tag{11}$$

This means that the competition between stimulated and spontaneous emission for a two-level system, which is in equilibrium with thermal radiation, depends on its Bose-Einstein factor. At room temperature, $T = 300$ K, the $\overline{n}(\nu)$ has different values in different spectral regions:

- $\overline{n}(\nu) >> 1$ for $h\nu << k_BT$; microwave region.
- $\overline{n}(\nu) \approx 1$ for $h\nu << k_BT$; infrared region.
- $\overline{n}(\nu) << 1$ for $h\nu >> k_BT$; visible region.

It can be concluded that the stimulated emission dominates over the spontaneous emission at small frequencies (i.e., for microwave region $h\nu << k_BT$), and at large frequencies (i.e., for visible region $h\nu >> k_BT$), the spontaneous emission is the major process for a two-level system in equilibrium with thermal radiation. This means that the stimulated emissions are a general phenomenon that occurs not only in lasers/masers but also in our surroundings.

It is worth mentioning that the predominance of stimulated emission at small frequencies, for example, in microwave region at $\nu = 10^{11}$ Hz, does not produce any lasing action in a medium in equilibrium with thermal radiation. Most of these photons emitted via the stimulated process are absorbed by the atoms/molecules in the lower energy level. Note that the lower energy level is always populated more than that of the upper level ($N_1 > N_2$) in normal conditions (i.e., at all positive temperatures) governed by Boltzmann distribution. This implies that an inverted condition, the so-called population inversion – where an upper level is more populated than a lower level ($N_2 > N_1$) – is required for lasing action to occur in a medium so that the amplification (irrespective of the operating frequencies) by stimulated emission exceeds over the absorption. This required condition was easy to realize in molecular systems (at microwave frequencies), for example, by injecting the preselected (excited ammonia) molecules into a resonant cavity and triggering them with microwave frequency photons, thus amplifying the microwave photons. This discovery was named MASER [2]; indeed, it was a precursor to the laser and its invention.

2.1 Population Inversion

Population inversion is a non-equilibrium state in a medium (or in a system) where $N_2 > N_1$. According to Eq. (1), the state of population inversion, possible only if T becomes a negative number, is often described as a state with a negative temperature, which cannot occur in reality. Population inversion must be maintained for photon amplification in all practical laser media except for the free-electron Laser (FEL). In such systems, population inversion is often achieved in the active medium by means of a pumping process. The FEL works on the principle of the self-amplified spontaneous emission (SASE) of high-energy electron beams [9].

3 Practical Laser and Level Schemes

A two-level scheme, illustrated in Fig. 2, is the simplest one; however, it does not produce any lasing action because no population inversion can be achieved in such a system. This is true even if its upper level is a long-lived or metastable state. Therefore, more than two levels are required to achieve lasing action. Two such generalized – a three-level and a four-level – schemes are depicted in Fig. 3. The level lifetimes, τ, given in these schemes are just representative figures to illustrate that the intermediate (laser) level is relatively metastable than other levels (except the ground most level).

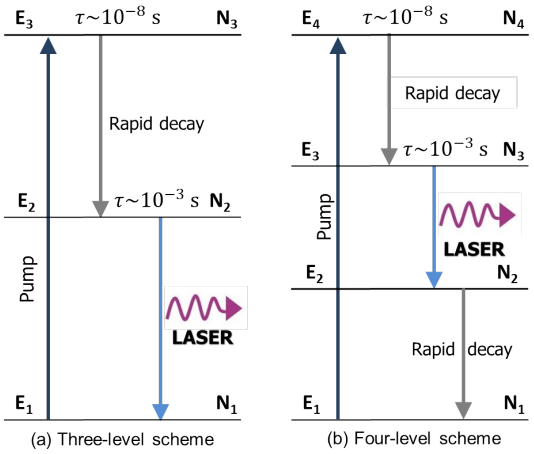

Fig. 3: *Laser schemes using (a) three-level (b) four-level systems.*

The pumping process lifts the atoms/molecules directly to the highest energy level, i.e., to level E_3 for a three-level and E_4 for a four-level laser. The population in this upper level undergoes rapid relaxation (mostly by non-radiative decay) to an intermediate level, i.e., to level E_2 in the case of a three-level and to level E_3 for a four-level system. This intermediate level has a relatively longer lifetime than other excited levels and is called a 'metastable state.' The radiative transition from this metastable state to the lower level is called the 'laser transition.' In the case of a three-level laser, this transition terminates at the ground level E_1; thus, the state of population inversion (i.e., more than 50% of the population in the metastable state) is not maintained at every instant of time instead, it may achieve the inverted population at certain intervals only; therefore, such laser has a pulse mode operation (see ruby laser in Section 4). In the case of a four-level laser, an additional intermediate level E_2 with a short lifetime is introduced between the metastable and ground levels. The lasing action occurs between the metastable state and the intermediate level E_2; hence, a continuous wave (CW-mode) or light beam is emitted. Note that this advantage is obtained when the ground level is omitted for the lasing transition. The He-Ne laser is a perfect example of a four-level scheme (see Section 5).

From a theoretical perspective, a laser has essentially three major components:

- An optical resonator, or cavity, is made of two exactly parallel and oppositely placed mirrors, which provides the selective positive feedback of the radiation emitted by the excited atoms/molecules of the active medium.
- An active medium, which amplifies or multiplies the photons in a cavity, consists of a collection of atoms/molecules in gas/liquid/solid form. The photon amplification is achieved when population inversion is maintained.
- An energy pump (source) that selectively populates the desired energy level by pumping the energy into the active medium, thereby achieving population inversion. Several types of pumping processes are used in lasers, such as optical, electrical, and chemical pumping.

4 The Ruby Laser

The ruby laser is a solid-state laser, which essentially works on the lasing principles of a three-level system. It was the first practical laser developed in 1960 by Theodore Maiman [6]. The active medium of this laser is a synthetic ruby crystal rod made of aluminum oxide (Al_2O_3) lightly doped with small amounts (about 0.05%) of chromium (Cr^{3+}) ions. An isolated atomic Cr^{3+} ion has a ground electronic configuration $3d^3$ with 19 fine structure energy levels, the energy of which varies up to 6.59 eV. The energy levels of its first excited electronic configuration $3d^2 4s$ start from the energy 12.89 eV. In the ruby crystal, the Cr^{3+} energy structures (of $3d^3$ configuration) are modified by the (stark effect) octahedral crystal field; therefore, it (ruby) forms many energy bands with distinct energies.

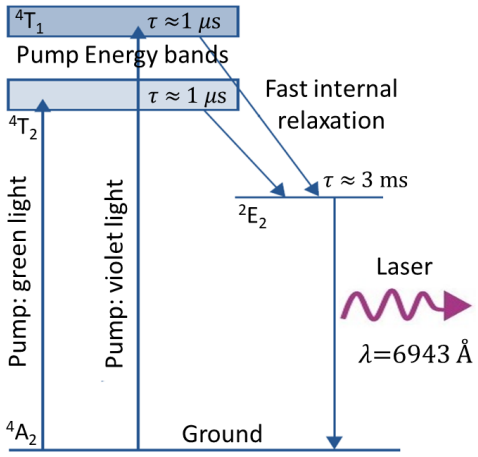

Fig. 4: *Energy level diagram of Ruby laser*

A simplified energy level diagram of ruby crystal relevant to its laser is given in Fig. 4. Its ground level is $^4A_2$ (shown as a single level in the figure, but in reality, it is a collection of discrete and closely spaced levels), the two excited broad energy bands $^4T_1$ and $^4T_2$ are at energy 3.0 eV and 2.2 eV, respectively, and its intermediate energy level $^2E_2$ (actually two, but only single is shown in the figure) is at 1.79 eV. Two of its very broad and strong absorp-

tion bands, $^4A_2 \longrightarrow {}^4T_2$ (U band) and $^4A_2 \longrightarrow {}^4T_1$ (Y band), are in the visible region at 4080 Å and 5580 Å, respectively. Therefore, population inversion can be achieved by means of optical pumping to these bands. Usually, a high-power xenon flash lamp is used for this purpose. The Cr^{3+} ions are excited to the upper pump energy bands $^4T_1$ and $^4T_2$ with the help of a xenon flash lamp. These pump energy bands have a very short lifetime, $\tau \approx 1\ \mu s$, and a portion of their population undergoes fast decay to the intermediate level $^2E_2$ by means of internal conversion. The level $^2E_2$ has a longer lifetime, $\tau \approx 3\ ms$, and thus is metastable. The transition from the metastable state $^2E_2$ to the ground level (at $\lambda = 6943$ Å) is triggered by photons in the resonant cavity. Whenever a sufficient population threshold is attained in level $^2E_2$, the lasing action will occur; therefore, the mode of operation of the laser will be in pulse form.

5 The He-Ne Laser

The He-Ne laser was the first gaseous laser built-in 1960 [7], which works on the principles of a four-level system. It was also the first laser to operate in CW mode. In its prototype version, the lasing action was obtained at an infrared wavelength of 1.1530 μm [7]. White and Rigden [10] first reported the amplification of its famous red line at 6328.16 Å. Nowadays, the He-Ne laser can be operated at various wavelengths in the visible-infrared region.

As we mentioned in the introduction, when students are asked to draw the energy levels of the He-Ne laser, they often draw oversimplified diagrams (Bohr's type) with a few levels without any spectroscopic level labelling or designation. Different types of energy level diagrams have been illustrated in various textbooks and internet sources, which sometimes makes them confusing. We use the LS-coupling scheme to designate both He and Ne levels, albeit the excited levels of Ne follow the intermediate (pair) jK-coupling scheme [11]. On the other hand, in most textbooks, energy levels of neon are labelled in an (over) simplified Paschen and/or Racah notations [12], which we found that students have difficulty understanding or often mess up with electronic configurations and fine structure levels labelling. Therefore, we use an explicit style for labelling atomic energy levels – electronic configuration followed by the spectroscopic level designated in the LS-coupling scheme. The energy levels of the Ne atom, relevant to the He-Ne laser, are given in Table 1 along with their LS designation and radiative lifetimes, $\tau_{sp} = 1/\Sigma A_{ki}$, which we computed using Cowan's code [11]. The jK-coupling designation for the Ne levels from the NIST ASD [3], is shown in the last column of the table.

A detailed energy level diagram of the He-Ne laser is given in Fig 5. The particularity of this diagram is explained in its caption. Nevertheless, here we briefly describe the energy structure of He and Ne atoms. The ground electronic configuration of the neutral helium (He I) atom is $1s^2$ (even parity) with $^1S_0$ as the ground level. The first excited electronic configuration of He I is $1s2s$ (even parity) with $^3S_0$ and $^1S_0$ levels. Meanwhile, the ground configuration of the neutral neon (Ne I) atom is $2p^6$ (even) with $^1S_0$ level[4]. The excited electronic configurations are of the types $2p^5nl$ ($n \geq 3$, $l = s, p, d, ...$) with several fine structure levels. For example, the first excited configuration is $2p^53s$ (odd parity) with four levels, which are designated as follows (see Table 1 for their equivalent designation in the jK-coupling scheme):

$(i)\ 2p^53s\ ^3P^\circ_2$ $(ii)\ 2p^53s\ ^3P^\circ_1$
$(iii)\ 2p^53s\ ^3P^\circ_0$ $(iv)\ 2p^53s\ ^1P^\circ_1$

The next excited configuration is $2p^53p$ with even parity and has 10 fine structure levels. For the He-Ne laser, the following excited configurations – $2p^53s$, $2p^54s$, $2p^55s$, $2p^53p$, and $2p^54p$ – and transitions between their (selected) fine structure levels are important (see Table 1 for their fine structure energy levels and radiative lifetimes). These excited configurations have their corresponding Paschen notations as $1s$, $2s$, $3s$, $2p$, and $3p$.

In the He-Ne laser, the optimum ratio of helium and neon varies from 5:1 to 20:1. The role of He atoms is to selectively excite the desired Ne level(s), from which lasing actions are expected. The operation of the He-Ne laser is well-detailed in all standard textbooks (see ref. [12]). Nonetheless, a brief description of the lasing mechanism is given here for completeness.

- The ground He atoms are excited to the long-lived $1s2s\ ^3S_1$ and $^1S_0$ states at energy E = 19.82 eV and E = 20.62 eV, respectively, using the electron impact excitation (EIE) process. The EIE process is more efficient to excite to the metastable

[3] `https://physics.nist.gov/asd`

[4] Ne I has a total of 10 electrons, but only its valance $2p^6$ electrons are shown here as they can easily be excited, and only those are relevant to the He-Ne laser as well.

[5] The photon absorption or spontaneous emission follows the selection rules – parity must change by one unit ($\Delta l = \pm 1$) and the change of angular momentum $\Delta J = 0, \pm 1$ – for strong electric dipole (E1-type) transitions. The transitions that do not satisfy this rule are called "forbidden transitions". They have very low A_{ki}; thus, their upper levels are long-lived and called "metastable state."

Table 1: *Energy levels of Ne I relevant to He-Ne laser*

Level Designation [LS-coupling][a]	**Energy (eV)**	τ_{sp}^{b} **(ns)**	**Level designation [NIST] [jK-coupling]**[c]
$2p^6\ ^1S_0$	0.0000	—	$2p^6\ ^1S_0$
$2p^5 3s\ ^3P_2^\circ$	16.6191	14.7×10^9	$2p^5(^2P_{3/2}^\circ)3s\ ^2[3/2]^\circ_2$
$2p^5 3s\ ^3P_1^\circ$	16.6708	23.0	$2p^5(^2P_{3/2}^\circ)3s\ ^2[3/2]^\circ_1$
$2p^5 3s\ ^3P_0^\circ$	16.7154	430×10^9	$2p^5(^2P_{1/2}^\circ)3s\ ^2[1/2]^\circ_0$
$2p^5 3s\ ^1P_1^\circ$	16.8481	2.0	$2p^5(^2P_{1/2}^\circ)3s\ ^2[1/2]^\circ_1$
$2p^5 3p\ ^3S_1$	18.3816	21.3	$2p^5(^2P_{3/2}^\circ)3p\ ^2[1/2]_1$
$2p^5 3p\ ^3D_3$	18.5551	17.9	$2p^5(^2P_{3/2}^\circ)3p\ ^2[5/2]_3$
$2p^5 3p\ ^3P_2$	18.5758	18.4	$2p^5(^2P_{3/2}^\circ)3p\ ^2[5/2]_2$
$2p^5 3p\ ^3D_1$	18.6127	18.0	$2p^5(^2P_{3/2}^\circ)3p\ ^2[3/2]_1$
$2p^5 3p\ ^1D_2$	18.6368	17.9	$2p^5(^2P_{3/2}^\circ)3p\ ^2[3/2]_2$
$2p^5 3p\ ^1P_1$	18.6934	18.1	$2p^5(^2P_{1/2}^\circ)3p\ ^2[3/2]_1$
$2p^5 3p\ ^3D_2$	18.7041	19.0	$2p^5(^2P_{1/2}^\circ)3p\ ^2[3/2]_2$
$2p^5 3p\ ^3P_0$	18.7114	16.1	$2p^5(^2P_{3/2}^\circ)3p\ ^2[1/2]_0$
$2p^5 3p\ ^3P_1$	18.7264	17.2	$2p^5(^2P_{1/2}^\circ)3p\ ^2[1/2]_1$
$2p^5 3p\ ^1S_0$	18.9660	11.4	$2p^5(^2P_{1/2}^\circ)3p\ ^2[1/2]_0$
$2p^5 4s\ ^3P_2^\circ$	19.6640	35.2	$2p^5(^2P_{3/2}^\circ)4s\ ^2[3/2]^\circ_2$
$2p^5 4s\ ^3P_1^\circ$	19.6882	7.2	$2p^5(^2P_{3/2}^\circ)4s\ ^2[3/2]^\circ_1$
$2p^5 4s\ ^3P_0^\circ$	19.7606	35.3	$2p^5(^2P_{1/2}^\circ)4s\ ^2[1/2]^\circ_0$
$2p^5 4s\ ^1P_1^\circ$	19.7798	8.0	$2p^5(^2P_{1/2}^\circ)4s\ ^2[1/2]^\circ_1$
$2p^5 4p\ ^3S_1$	20.1496	187	$2p^5(^2P_{3/2}^\circ)4p\ ^2[1/2]_1$
$2p^5 4p\ ^3D_3$	20.1884	134	$2p^5(^2P_{3/2}^\circ)4p\ ^2[5/2]_3$
$2p^5 4p\ ^3P_2$	20.1969	149	$2p^5(^2P_{3/2}^\circ)4p\ ^2[5/2]_2$
$2p^5 4p\ ^1P_1$	20.2110	138	$2p^5(^2P_{3/2}^\circ)4p\ ^2[3/2]_1$
$2p^5 4p\ ^3D_2$	20.2142	119	$2p^5(^2P_{3/2}^\circ)4p\ ^2[3/2]_2$
$2p^5 4p\ ^3P_0$	20.2592	94.8	$2p^5(^2P_{3/2}^\circ)4p\ ^2[1/2]_0$
$2p^5 4p\ ^3D_1$	20.2909	138	$2p^5(^2P_{1/2}^\circ)4p\ ^2[3/2]_1$
$2p^5 4p\ ^3P_1$	20.2972	130	$2p^5(^2P_{1/2}^\circ)4p\ ^2[1/2]_1$
$2p^5 4p\ ^1D_2$	20.2973	137	$2p^5(^2P_{1/2}^\circ)4p\ ^2[3/2]_2$
$2p^5 4p\ ^1S_0$	20.3689	40.2	$2p^5(^2P_{1/2}^\circ)4p\ ^2[1/2]_0$
$2p^5 5s\ ^3P_2^\circ$	20.5601	73.7	$2p^5(^2P_{3/2}^\circ)5s\ ^2[3/2]^\circ_2$
$2p^5 5s\ ^3P_1^\circ$	20.5706	15.3	$2p^5(^2P_{3/2}^\circ)5s\ ^2[3/2]^\circ_1$
$2p^5 5s\ ^3P_0^\circ$	20.6566	74.0	$2p^5(^2P_{1/2}^\circ)5s\ ^2[1/2]^\circ_0$
$2p^5 5s\ ^1P_1^\circ$	20.6628	24.0	$2p^5(^2P_{1/2}^\circ)5s\ ^2[1/2]^\circ_1$

[a] In LS-coupling, fine structure levels are designated in the ^ML_J format, where the multiplicity $M = 2S + 1$ computed from the total electronic spin S, the total orbital angular momentum L takes the following values $L = 0, 1, 2, ...$, are designated as S, P, D, ... terms, and the total angular momentum J is produced by the spin-orbit coupling.

[b] Radiative lifetime is computed from the theoretical transition rates, $\tau_{sp} = 1/\Sigma A_{ki}$.

[c] The jK-coupling takes place when the spin-orbit interaction of more tightly bound inner electrons ($2p^5$ electrons of Ne atom) become dominant, and the outermost electron experiences a small spin-independent Coulomb interaction with the core inner electrons. As a consequence of this, energy levels tend to appear or observe in pairs. The order of (two electron case) angular momenta coupling scheme is:- the inner electron(s) generates the $j_1 = l_1 + s_1$ momenta, and (l_2, s_2) of outermost electron interaction provides the $K = j_1 + l_2$ and $J = K + s_2$ momenta. The standard level designation is $j_1\ ^2[K]_J$. In the case of Ne, $2p^5$ electrons produces $j_1 = 1/2, 3/2$, which are designated as $^2P_{1/2}^\circ$ or $^2P_{3/2}^\circ$ and their coupling with (l_2, s_2) of the outermost electron makes a series of $^2[K]_J$ states.

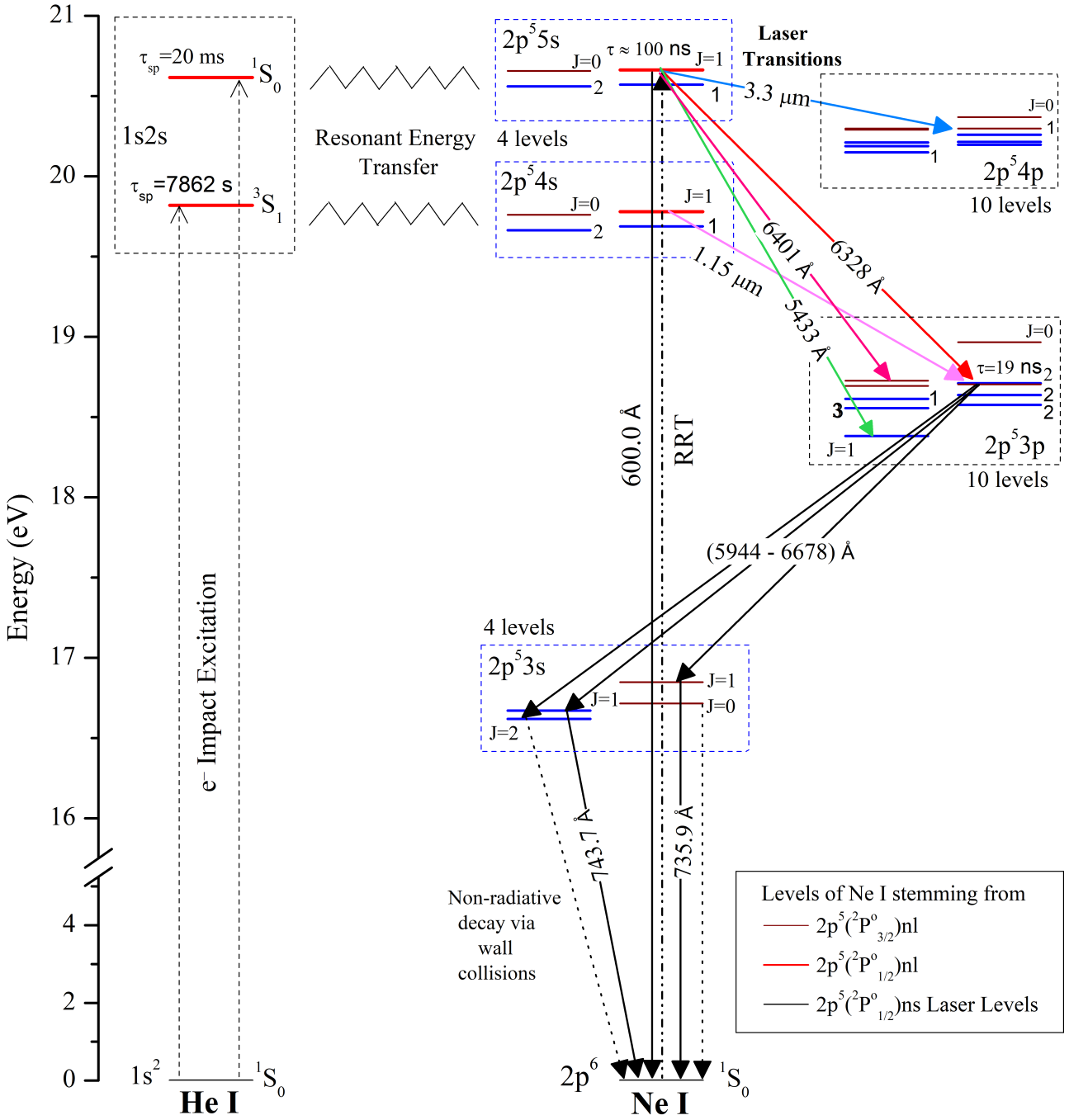

Fig. 5: *Energy level diagram of He-Ne laser with selected laser transitions from the levels of the $2p^5 4s$ and $2p^5 5s$ to those of $2p^5 3p$ and $2p^5 4p$ configurations. Only the decay channels for the famous 6328.16 Å laser line are shown in detail. All levels are shown at the fine structure level with their J-values. Note: The close energy levels of Ne I are horizontally separated for their better visibility; still, not all levels of $2p^5(3p + 4p)$ configurations are fully resolved (see text).*

states than the photon impact or absorption[5] process (see Section 6.4 of ref. [12]). The radiative lifetimes (τ_{sp}) of He I $1s2s\ ^3S_1$ and $^1S_0$ levels are about 7900 s and 20 ms, respectively. However, this metastability partly depends on the He atoms' collision rate with the cavity or discharge tube walls and their collision rates with slow electrons. In the latter process, the electrons gain more kinetic energy from the excitation energy (super-elastic collision). As a result of the collisions, the effective lifetime of the levels is always smaller than their radiative lifetime. It has been reported that the He metastable levels ($1s2s\ ^3S_1$ and $^1S_0$) are quenched by the super-elastic collision processes at high discharge current densities. Thus, in real scenarios, the system requires optimal values of gas pressures, cavity dimensions, and electron discharge current densities for smooth operation.

- The excited He atoms ($1s2s\ ^3S_1$ & $^1S_0$) collide with the ground Ne atoms and exchange their energy with the Ne atoms. This process is known as near-resonant energy transfer (RET) since the energy level values of the $1s2s\ ^3S_1$ & $^1S_0$ levels of He are about those of the $2p^54s$ and $2p^55s$ configurations (see Fig. 5); thus, there is a finite probability for the process. Although several RET schemes are possible with the fine structure levels of the Ne $2p^54s$ and $2p^55s$ configurations, only two relevant schemes are depicted below:

$$(i)\ He\ I\ (1s2s\ ^3S_1) + Ne\ I\ (2p^6\ ^1S_0) \longrightarrow He\ I\ (1s^2\ ^1S_0) + Ne\ I\ (2p^54s\ ^1P_1^\circ)$$

$$(ii)\ He\ I\ (1s2s\ ^1S_0) + Ne\ I\ (2p^6\ ^1S_0) \longrightarrow He\ I\ (1s^2\ ^1S_0) + Ne\ I\ (2p^55s\ ^1P_1^\circ)$$

Although the direct EIE in Ne also contributes to the population inversion, it has been confirmed that the collisional RET process described above significantly increases the population of the laser levels, $^1P_1^\circ$ of the $2p^54s$ and $2p^55s$. These laser levels have several decaying transitions to lower energy levels of $2p^53p$ and $2p^54p$ configurations. The radiative transition parameters of these selected laser levels – $^1P_1^\circ$ of $2p^54s$ and $2p^55s$ configurations – are given in Table 2. In this table, special focus is given for its well-known red line at $\lambda = 6328.16$ Å; its complete decay channels along with radiative line parameters are listed. The next step is to select a particular transition of lasing interest[6] and tune the laser cavity conditions to favor and amplify the selected laser line.

- For example, when the cavity is tuned for the amplification of the 6328.16 Å line, which is due to the following fine structure transition:

$$2p^55s\ ^1P_1^\circ \longrightarrow 2p^53p\ ^3D_2$$

The absolute branching fraction $|BF|$ for this transition is 0.083, the highest among all transitions terminating to the levels of the $3p$ and $4p$ configurations (see Table 2), indicating that the amplification factor of the expected laser output for this line would be the highest. It is evident from Table 2 that the strongest branch for the transitions originating from the $2p^55s\ ^1P_1^\circ$ level is a VUV (vacuum ultraviolet) line at $\lambda = 600.04$ Å with $|BF| = 0.694$, belongs to the spontaneous decay of the $2p^55s\ ^1P_1^\circ \longrightarrow 2p^6\ ^1S_0$. It may appear as a loss of the population of the upper level by radiative means; however, this transition makes the resonant radiation trapping (RRT) effect – a photon emitted by one atom is absorbed by another atom in the ground state before it escapes from the medium, and eventually an atom reaches back into the excited state – due to which the effective lifetime (τ) of its upper level $2p^55s\ ^1P_1^\circ$ is increased[7]. The radiative lifetime of this upper level is $\tau_{sp}^{5s} \approx 24$ ns (where A_{ki} is the transition probability, which represents the rate of spontaneous emission), but it will be increased up to $\tau^{5s} = 100$ ns by the RRT process [12] at a total pressure of 1 Torr. With this increased lifetime, the probability of the stimulated emission gets enhanced, and a CW operation of lasing transition at 6328.16 Å is achieved since the radiative lifetime of its lower level $2p^53p\ ^3D_2$ is $\tau_{sp}^{3p} \approx 20$ ns, is essentially defined by the following fast decaying transitions (see Table 2):

$$2p^53p\ ^3D_2 \longrightarrow 2p^53s\ ^3P_2^\circ$$

[6] One of the keys to selecting the laser transition is the absolute branching fraction $|BF|$ of the line (see Table 2). Note that not all lines have the net gain to produce lasing action. Different mirrors and wavelength-selecting elements (e.g., prisms or gratings) are generally used for single-line selection.

[7] In principle, this lifetime increase (by the RRT) depends on the following parameters:- gas pressure (atomic density), temperature, cross-section of the transition involved, and geometry and opacity of the medium, whether it is enclosed or not.

Table 2: *Radiative transition parameters for selected laser levels in Ne I.*

λ_{obs} (Å)	Intens.[a] (arb. u.)	A_{ki}[b] (s^{-1})	Level Designation & Energy				$\|BF\|$[c]	Comments[d]
			Lower	E_{low} (eV)	Upper	E_{upp} (eV)		
Decay channels of the $2p^5 5s\ ^1P_1^\circ$ level.								
600.04	20	2.85e+07	$2p^6\ ^1S_0$	0.000	$2p^5 5s\ ^1P_1^\circ$	20.663	0.694	RRT
5433.65	2500	2.83e+05	$2p^5 3p\ ^3S_1$	18.382	...	...	0.007	Laser
5939.32	500	2.00e+05	$2p^5 3p\ ^3P_2$	18.576	...	...	0.005	Laser
6046.13	500	2.26e+05	$2p^5 3p\ ^3D_1$	18.613	...	...	0.006	
6118.02	150	6.09e+05	$2p^5 3p\ ^1D_2$	18.637	...	...	0.015	Laser
6293.74	1000	6.39e+05	$2p^5 3p\ ^1P_1$	18.693	...	...	0.016	
6328.16	3000	3.39e+06	$2p^5 3p\ ^3D_2$	18.704	...	...	0.083	Laser
6351.85	1000	3.45e+05	$2p^5 3p\ ^3P_0$	18.711	...	...	0.008	
6401.08	1000	1.39e+06	$2p^5 3p\ ^3P_1$	18.726	...	...	0.034	Laser
7304.84	89	2.55e+05	$2p^5 3p\ ^1S_0$	18.966	...	...	0.006	
24162.55	12	9.60e+04	$2p^5 4p\ ^3S_1$	20.150	...	...	0.002	
30720.02	53	1.05e+05	$2p^5 4p\ ^3P_0$	20.259	...	...	0.003	
33341.79	230	6.48e+05	$2p^5 4p\ ^3D_1$	20.291	...	...	0.016	Laser
33912.26	440	1.07e+06	$2p^5 4p\ ^3P_1$	20.297	...	...	0.026	Laser
33922.35	1200	2.92e+06	$2p^5 4p\ ^1D_2$	20.297	...	...	0.071	Laser
42182.98	140	3.64e+05	$2p^5 4p\ ^1S_0$	20.369	...	...	0.009	
Decay channels for the red line at $\lambda = 6328.16$ Å.								
5944.83	5000	1.13e+07	$2p^5 3s\ ^3P_2^\circ$	16.619	$2p^5 3p\ ^3D_2$	18.704	0.214	
6096.16	3000	1.81e+07	$2p^5 3s\ ^3P_1^\circ$	16.671	...	...	0.343	
6678.28	5000	2.33e+07	$2p^5 3s\ ^1P_1^\circ$	16.848	...	...	0.442	
735.90	300	5.88e+08	$2p^6\ ^1S_0$	0.000	$2p^5 3s\ ^1P_1^\circ$	16.848	1.000	
743.72	120	4.40e+07	...	...	$2p^5 3s\ ^3P_1^\circ$	16.671	1.000	
741.74	-	-	...	...	$2p^5 3s\ ^3P_0^\circ$	16.715	0.000	FB, NR
746.04	-	6.79e-02	...	...	$2p^5 3s\ ^3P_2^\circ$	16.619	0.000	M2, NR
Decay channels of the $2p^5 4s\ ^1P_1^\circ$ level.								
626.82	60	9.45e+07	$2p^6\ ^1S_0$	0.000	$2p^5 4s\ ^1P_1^\circ$	19.780	0.796	RRT
8865.31	2100	8.31e+05	$2p^5 3p\ ^3S_1$	18.382	...	...	0.007	
10295.42	420	1.46e+05	$2p^5 3p\ ^3P_2$	18.576	...	...	0.001	
10620.66	780	2.21e+05	$2p^5 3p\ ^3D_1$	18.613	...	...	0.002	
10844.48	9400	2.99e+06	$2p^5 3p\ ^1D_2$	18.637	...	...	0.025	
11409.13	8800	2.71e+06	$2p^5 3p\ ^1P_1$	18.693	...	...	0.023	
11522.75	33000	1.07e+07	$2p^5 3p\ ^3D_2$	18.704	...	...	0.090	Laser
11601.54	2600	7.51e+05	$2p^5 3p\ ^3P_0$	18.711	...	...	0.006	
11766.79	15000	4.54e+06	$2p^5 3p\ ^3P_1$	18.726	...	...	0.038	
15230.71	5300	1.40e+06	$2p^5 3p\ ^1S_0$	18.966	...	...	0.012	Laser

[a] Relative observed intensity of spectral line in arbitrary units.
[b] Transition probability (A_{ki}) represents Einstein's A coefficient for spontaneous emission. Most of the transitions are allowed (strong) electric dipole (E1) types, otherwise their types are indicated in the last column.
[c] Absolute branching fraction ($|BF|$), computed using the expression $|BF| = A_{ki}/\sum A_{ki}$, represents the strength of a transition branch that originate from a common upper level.
[d] Comments: FB—strictly forbidden transition, by $\Delta J \neq 0 \leftrightarrow 0$ selection rule, for even isotopes of neon ($^{20,22}Ne$ with 90.4% & 9.3% abundances in Ne natural samples, and their nuclear spin $I = 0$) and for the odd isotope of Ne (^{21}Ne; 0.3%; $I = 1.5$), this decay is a weak hyperfine-induced transition with $\tau_{sp} = 0.71$ s, Laser—lasing action has been achieved for the indicated transition, M2—transition is a magnetic quadrupole type, NR—non-radiative decay due to collision of Ne atoms with walls of the tube, RRT—transition is affected by the resonant radiation trapping effect, which increases the lifetime of the higher level.

$$2p^5 3p\ ^3D_2 \longrightarrow 2p^5 3s\ ^3P_1^\circ$$
$$2p^5 3p\ ^3D_2 \longrightarrow 2p^5 3s\ ^1P_1^\circ$$

Note that all levels of $2p^5 3p$ configuration have nearly the same lifetime of about 20 ns, which indicates that, theoretically, lasing action can be achieved for all possible transitions between $2p^5 5s\ ^1P_1^\circ$ to the levels of $2p^5 3p$. Many researchers reported lasing actions at different wavelengths; thus, we marked particularly some of them in Table 2.

- The levels of $2p^5 3s$ are decayed to the ground level $2p^6\ ^1S_0$ via radiative or non-radiative decay channels:

  (i) The $2p^5 3s\ ^1P_1^\circ$ and $2p^5 3s\ ^3P_1^\circ$ levels have strong radiative decay channels to the ground level.

  (ii) The $2p^5 3s\ ^3P_0^\circ$ and $2p^5 3s\ ^3P_2^\circ$ levels are long-lived or metastable states and have very weak transition rates (A_{ki}) to the ground state (see Table 2). But their metastability will be destroyed by atom-atom, atom-slow electron, and atom-wall (of discharge tube or cavity) collisions, and thereby these levels are de-populated. This collisional destruction also reduces the possibility of the collisional excitation to the levels of $2p^5 3p$ configuration from the metastable levels of $2p^5 3s$ by electron impact. The atom-wall collisions become faster and more dominant as cavity dimensions (at least in one dimension) are smaller. In this regard, a narrow but long tube is generally used in all practical He-Ne laser systems.

A CW operation of the laser output is possible since a favorable lifetime ratio exists in the system between the levels of (i) $2p^5 5s$ and $2p^5 3p$ or (ii) $2p^5 5s$ and $2p^5 4p$ or (iii) $2p^5 4s$ and $2p^5 3p$. Indeed, it was one of the reasons Ali Javan and his colleagues [7] obtained lasing actions at five different infrared wavelengths, namely, 11180, 11530, 11600, 11990, and 12070 Å, which corresponds to fine structure transitions of the $2p^5 4s \longrightarrow 2p^5 3p$. The strongest amplification was found at 11530 Å with an output power of 15 mW. Also, gain in the medium at infrared wavelength is much larger than at visible ones (since gain is inversely proportional to ν^2 or use Eq. 11 for a simple comparison). The $2p^5 5s \longrightarrow 2p^5 4p$ transitions fall in the infrared region and those of $2p^5 5s \longrightarrow 2p^5 3p$ are in the visible region (see Table 2). For comparison purposes, one may consider their 3.3922 μm and 6328.16 Å lines; since the infrared line has a relatively larger gain compared to the red one, the laser oscillation and amplification will tend to occur at 3.3922 μm rather than at 6328.16 Å. Thus, for the oscillation and amplification of the red line at 6328.16 Å, the gain of the infrared line(s) must be suppressed by various means, for example, with the use of suitable infrared absorbers in the cavity and/or by introducing the line selection elements such as prism or grating or by increasing the linewidth of the unwanted lines by applying an inhomogeneous magnetic field. The laser output at the visible wavelength of 6328.16 Å was first demonstrated by White and Rigden [10].

References

[1] A. Einstein, "Zur Quantentheorie der Strahlung," *Physikalische Gesellschaft Zürich*, vol. 18, pp. 47–62, 1916, & also in *Physikalische Zeitschrift*, vol. 18pp. 121–128, 1917.

[2] J. P. Gordon, H. J. Zeiger, and C. H. Townes, "The maser—new type of microwave amplifier, frequency standard, and spectrometer," *Phys. Rev.*, vol. 99, pp. 1264–1274, 4 1955. DOI: 10.1103/PhysRev.99.1264.

[3] A. L. Schawlow and C. H. Townes, "Infrared and Optical Masers," *Physical Review*, vol. 112, no. 6, pp. 1940–1949, 1958. DOI: 10.1103/PhysRev.112.1940.

[4] J. H. Sanders, "Optical Maser Design," Phys. Rev. Lett., vol. 3, no. 2, pp. 86–87, 1959. DOI: 10.1103/PhysRevLett.3.86.

[5] A. Javan, "Possibility of Production of Negative Temperature in Gas Discharges," Phys. Rev. Lett., vol. 3, no. 2, pp. 87–89, 1959. DOI: 10.1103/PhysRevLett.3.87.

[6] T. H. Maiman, "Stimulated Optical Radiation in Ruby," Nature, vol. 187, no. 4736, pp. 493–494, 1960. DOI: 10.1038/187493a0.

[7] A. Javan, W. R. Bennett, and D. R. Herriott, "Population Inversion and Continuous Optical Maser Oscillation in a Gas Discharge Containing a He-Ne Mixture," Phys. Rev. Lett., vol. 6, no. 3, pp. 106–110, 1961. DOI: 10.1103/PhysRevLett.6.106.

[8] C. N. Banwell and E. M. McCash, *Fundamentals of molecular spectroscopy*. Tata McGraw-Hill, 1995.

[9] G. Margaritondo and P. Rebernik Ribic, "A simplified description of X-ray free-electron lasers," *Journal of Synchrotron Radiation*, vol. 18, no. 2, pp. 101–108, 2011. DOI: 10.1107/S090904951004896X.

[10] A. D. White and J. D. Rigden, "Continuous gas maser operation in the visible," *Proc. IRE*, vol. 50, p. 1697, 1962.

[11] R. D. Cowan, *The Theory of Atomic Structure and Spectra (Berkeley, CA: University of California Press)*, 1981.

[12] O. Svelto and D. C. Hanna, *Principles of Lasers*. 2010. DOI: 10.1007/978-1-4419-1302-9.

Progress in Inorganic-Organic Hybrid Perovskites Semiconductors

Mohammad Adnan
Department of Physics, Aligarh Muslim University, Aligarh, UP, India-202002

Abstract

Hybrid materials, which integrate organic and inorganic components at the molecular level, are emerging as highly promising materials due to the diverse yet complementary properties of these two distinct classes. The customized molecular integration of desirable inorganic and organic features within a single molecular-scale composite can be synergistically leveraged to overcome the limitations of individual components. Among various hybrid materials, the incorporation of suitable passive organic moieties into an active inorganic semiconducting matrix is particularly intriguing and extensively studied. These hybrid semiconductors demonstrate unique structural diversities and interesting optical, electrical, thermal and magnetic properties and are widely explored by research communities along with other semiconductors such as graphene, transition metal dichalcogenides (MoS_2, WS_2 etc), and phosphorene. Due to their fascinating room temperature characteristics and environmental stability, these hybrid perovskites have found promising applications in various photonic and optoelectronic devices such as light-emitting diodes, photodetectors, lasers, and solar cells. Embracing the challenges and opportunities in semiconductor technology, India is making significant strides in this field and emerging as a hub for one of the world's most promising renewable energy markets with a motto of *"India's semiconductor ecosystem is a solution not just for India's challenges but also for global challenges"*.

1 Introduction

India is on a path to becoming a global leader in semiconductor manufacturing, driven by a clear vision to advance its semiconductor industry. The Indian government has launched several initiatives, including the India Semiconductor Mission (ISM) and the Semicon India program, to promote semiconductor manufacturing and technology development through collaborative efforts among government ministries, industry stakeholders, and academic institutions. Additionally, India has established strong international partnerships with global technology leaders, such as Powerchip Semiconductor Manufacturing Corporation (PSMC) in Taiwan and Synopsys in the USA. One of the key advantages driving industry growth in India is its vast domestic market, making it the second-largest market for 5G smartphones after China. However, significant challenges remain, particularly the complexities of semiconductor fabrication, which demand substantial investments, state-of-the-art infrastructure, a highly skilled workforce, and advanced technology. In 2023, India's semiconductor market was valued at approximately $45 billion and is expected to experience rapid growth in the coming years.

Semiconductors are materials characterized by a small electronic bandgap, enabling thermally excited charge carriers to facilitate current flow at higher temperatures. Among these, silicon plays a pivotal role in the modern microelectronics industry, with key applications in solar cells, light sources, and detectors [1]. Beyond silicon technology, a wide array of advanced semiconductors has emerged, including inorganic-organic hybrid perovskites, graphene, transition metal dichalcogenides (TMDs), and phosphorene [2-4]. This article focuses on one of the most promising materials, inorganic-organic (IO) hybrid perovskites, which have found extensive applications in photonic, optoelectronic, and photovoltaic devices.

2 Advancing Research on Inorganic-Organic Hybrid Perovskite in India

Research on IO hybrid perovskites, under the broader category of Metal-Organic Frameworks (MOFs), began in India in the early 2000s. This pioneering work was led by Prof. Ram Seshadri's group and Prof. C. N. Rao's group at IISc Bangalore, with a primary focus on the synthesis and structural properties of these materials. Over the past two decades,

Prof. G. Vijaya Prakash's group at IIT Delhi has established a strong correlation between the optical properties and structural features of IO hybrid perovskites. The group is actively involved in exploring various IO hybrid perovskites, investigating their linear and nonlinear optical properties in both two-dimensional (2D) and three-dimensional (3D) structures. Utilizing ultrashort laser pulses, they conduct real-time monitoring of intercalation processes and one- or two-photon-induced crystal imaging [5,6]. Their research primarily focuses on developing novel perovskite materials tailored for applications in optoelectronic devices and solar cells. In recent years, several research groups have actively explored optoelectronic and photovoltaic devices, including those led by Prof. D. D. Sharma (IISc Bangalore), Prof. Dinesh Kabra (IIT Bombay), Prof. Samit Kumar Ray (IIT Kharagpur), Prof. Suman Kalyan Paul (IIT Mandi), and Prof. Sameer Sapra (IIT Delhi). Among them, Prof. Dinesh Kabra's group at IIT Bombay has made significant contributions over the past decade, particularly in the development of organic LEDs and stable photovoltaic devices [7].

3 Global Advancements in Inorganic-Organic Hybrid Perovskite Research

The IO hybrid perovskites have garnered global attention for their promising applications in optoelectronic devices and solar cells. Perovskite-based solar cells have shown a remarkable increase in power conversion efficiency, rising from approximately 3.8% in 2009 to over 28% today. However, the commercialization of this technology remains a significant challenge due to its instability under high temperatures and harsh environmental conditions [8-11]. In fact, few research groups are working on the hybrid inorganic-organic materials since late 80s. Ishihara group investigated the strong room-temperature optical properties then followed by Mitzi group [12-14]. They mostly investigated 2D perovskites, and focused on their optical absorption and photoluminescence properties. The crystal structural studies were extensively studied by Billing's group [15]. The first report on AMX_3 type 3D IO hybrid perovskites (where $A = CH_3NH_3^+$) were published by Papavassiliou group in 1995, which has now led to its tremendous application in photovoltaics [16]. Several research groups across the globe, notably led by Michael Graetzel, M. K. Nazeeruddin, Sir Richard Friend, Henry J. Snaith, Subodh Mhaisalkar, Annalisa Bruno, Christoph Brabec are working in the area of perovskites mainly targeted towards enhancing the stability of perovskite solar cells [17-19].

4 Excitons in Inorganic-Organic Hybrid Perovskite

2D IO hybrid perovskites are represented by the general formula R_2MX_4, where R is the organic moiety, M is divalent metal (Pb^{2+}, Sn^{2+} etc.) and X is halide (Cl^-, Br^-, I^-). The weak van der Waals interaction and hydrogen bonding between the organic ammonium cation and the terminal halide of the inorganic $[MX_6]^{4-}$ octahedral part determine the conformation and orientation of the organic ammonium cation as shown in Fig. 1(a). Due to the difference in their bandgaps, they form multiple quantum well structure (MQWs) (Fig. 1(a)), where inorganic and organic layers act as *well* and *barrier* respectively. The fascinating features of these 2D IO hybrid perovskites are the presence of room temperature optical excitons with large exciton binding energy ($\sim$ 200-250 meV) as compared to parent inorganic PbI_2 ($\sim$ 23 meV). The exciton energy levels are shown in Fig. 1(b) where exciton levels lie slightly below the bandgap of the material. The formation of natural multiple quantum well structure and reduced dielectric screening effects are mainly responsible for stable optical excitons which additionally enhances the stability [20,21].

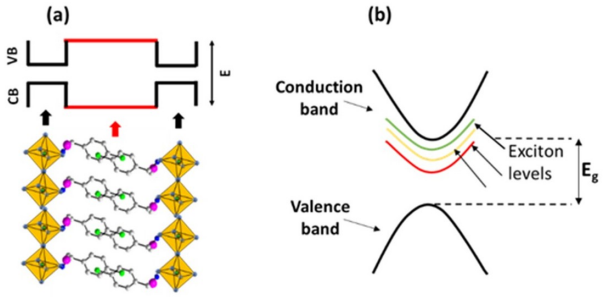

Fig. 1: *(a) represents the alternative stacking of organic and inorganic layers and corresponding multiple quantum wells structures (b) represents the schematic of exciton energy levels in these IO hybrid semiconductors*

5 Inorganic-organic hybrid perovskites single crystal platelets

Fig. 2(a) exhibits optical microscopic images of single crystal platelets of two different IO hybrid perovskites, $(Cl-C_6H_4-C_2H_4NH_3)_2PbI_4$ (CEPI) and $(CH_3-C_6H_4-C_2H_4NH_3)_2PbI_4$ (MPEPI). Bright field (BF) optical images are recorded with the help of a white light source attached with the microscope (Olympus, BX-51). The photoluminescence (PL) images are captured by exciting with 405 nm UV laser excitation. The intense green colour PL image

confirms their highly emitting nature and the presence of room temperature excitons. The room temperature absorption spectra show narrow and strong exciton absorption peak around 495 nm (2.50 eV) with FWHM of $\sim$ 20 nm along with band edge and charge transfer regions. When these perovskites are excited with 405 nm UV laser, they demonstrate strong exciton emission peak around 510 nm (2.43 eV) (Fig. 2(b,c)) [22].

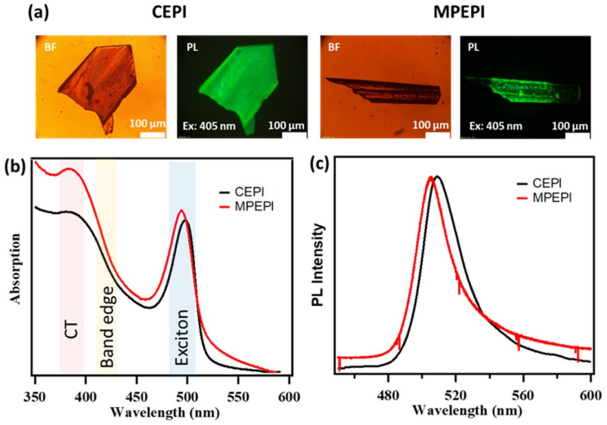

Fig. 2: *(a) Bright field (BF) and photoluminescence (PL) optical images of single crystal platelets of IO hybrid perovskites, CEPI and MPEPI (b,c) Room temperature absorption and photoluminescence spectra of their thin films, Ex: 405 nm laser, Ref [22]*

6 Mixed halide colloidal nanoparticles

To further tune the exciton emission over a broad spectral domain, mixed halide colloidal nanoparticles $CH_3NH_3PbBr_{0.5}I_{0.5}$ (hereafter, $C1PBr_{0.5}I_{0.5}$) are fabricated. When these nanoparticles are exposed under 405 nm UV laser excitations, they exhibit a series of fascinating colours due to the change in their bandgaps through inter-ion migration as shown in Fig. 3(a). The photoluminescence tunability under continuous laser exposure confirms the tunability of excitons over broad spectral domain with the emergence of several metastable states which makes them potential candidate for LEDs and tunable lasers. The stability of these mixed halide colloidal nanoparticles can be enhanced with the help of surface functionalization process where these nanoparticles are capped with long alkylammonium based 2D perovskites as shown in Fig. 3(b-d). For surface passivation, octylamine based 2D perovskites such as $C_8H_{17}NH_3Cl(C8Cl)$, $C_8H_{17}NH_3Br(C8Br)$, $C_8H_{17}NH_3I(C8I)$ are used [23].

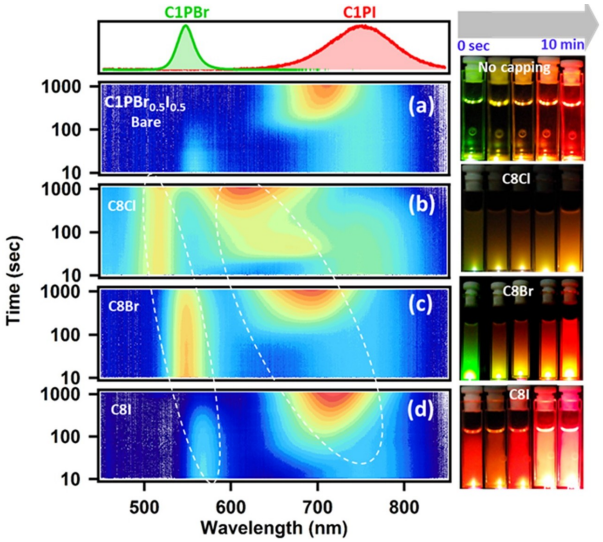

Fig. 3: *(a) Real-time photoluminescence monitoring of mixed halide colloidal nanoparticles C1PBr0.5I0.5 under continuous UV laser exposure. (b-d) when these nanoparticles are functionalized with C8Cl, C8Br and C8I, respectively. Right side images are corresponding PL camera images taken at different exposure times. (For colour PL images, refer to web version of this article.) [23]*

References

[1] H. Lin, M. Yang, X. Ru, et al., Silicon heterojunction solar cells with up to 26.81% efficiency achieved by electrically optimized nanocrystalline-silicon hole contact layers, Nat Energy 8 (2023) 789-799.

[2] P. Tonndorf, R. Schmidt, P. Böttger, X. Zhang, J. Börner, A. Liebig, M. Albrecht, C. Kloc, O. Gordan, D. R. T. Zahn, S. M. de Vasconcellos, R. Bratschitsch, Photoluminescence emission and Raman response of monolayer $MoS_2, MoSe_2, andWSe_2$, Opt. Exp. 21 (2013) 4908-4916.

[3] Z. Peng, X. Chen, Y. Fan, D. J. Srolovitz, D. Lei, Strain engineering of 2D semiconductors and graphene: from strain fields to band-structure tuning and photonic applications, Light Sci. Appl. 9 (2020) 190.

[4] R. Dutta, S. Kakkar, P. Mondal, N. Chauhan, J. K. Basu, Electrical tuning of optical properties of quantum dot-graphene hybrid devices: Interplay of charge and energy transfer, J. Phys. Chem. C. 125 (2021) 8314-8322.

[5] M. Adnan, J. J. Baumberg and G. Vijaya Prakash, Linear and nonlinear optical probing of various excitons in 2D inorganic-organic hybrid structures, Sci. Rep. 10 (2020) 2615.

[6] P. K. Kanaujia, M. Adnan, K. M. Dehury, M. Akram, and G. Vijaya Prakash, Real-Time Monitoring of Progressive Crystal Phase Transformations and Associated Multi-Phase Optical Exciton Dynamics in Mixed (2D/3D) Inorganic-Organic Hybrid Semiconductors, Chem. Mater. 35 (2023) 7984-7994.

[7] N. K. Kumawat, D. Gupta, D. Kabra, Recent advances in metal halide-based perovskite light emitting diodes, Energy Technol. 5 (2017) 1734-1749.

[8] A. Kojima, K. Teshima, Y. Shirai and T. Miyasaka, Organometal halide perovskites as visible-light sensitizers for photovoltaic cells, J. Am. Chem. Soc. 131 (2009) 6050-6051.

[9] X. Zhao, T. Liu, and Y. Loo, Advancing 2D Perovskites for Efficient and Stable Solar Cells: Challenges and Opportunities, Adv. Mater. 34 (2022) 2105849.

[10] E. B. Kim, M. S. Akhtar, H. S. Shin, S. Ameen, and M. K. Nazeeruddin, A review on two-dimensional (2D) and 2D-3D multidimensional perovskite solar cells: Perovskites structures, stability, and photovoltaic performances, J. Photochem. Photobiol. C: Photochem. Rev. 48 (2021) 100405.

[11] J. Wen, Y. Zhao, P. Wu, et al., Heterojunction formed via 3D-to-2D perovskite conversion for photostable wide-bandgap perovskite solar cells, Nat. Commun. 14 (2023) 7118.

[12] T. Ishihara, J. Takahashi, and T. Goto, Optical properties due to electronic transitions in two-dimensional semiconductors $(C_nH_{2n+1}NH_3)_2PbI_4$, Phys. Rev. B: Condens. Matter Mater. Phys. 42 (1990) 11099.

[13] D. B. Mitzi, S. Wang, C. A. Feild, C. A. Chess, A. M. Guloy, Conducting layered organic-inorganic halides containing <110>- oriented perovskite sheets, Science 267 (1995) 1473-1476.

[14] D. B. Mitzi, Organic-inorganic perovskites containing trivalent metal halide layers: the templating influence of the organic cation layer, Inorg. Chem. 39 (2000) 6107.

[15] D. G. Billing and A. Lemmerer, Octakis (3-propylammonium) octadecaiodopentaplumbate (II): a new layered stucture based on layered perovskites, Acta Cryst. 62 (2006) 174-176.

[16] G. C. Papavassiliou, I. B. Koutselas, Structural, optical and related properties of some natural three-and lower-dimensional semiconductor systems. Synth. Met. 71 (1995) 1713-1714.

[17] X. Zhao, T. Liu, and Y. Loo, Advancing 2D Perovskites for Efficient and Stable Solar Cells: Challenges and Opportunities, Adv. Mater. 34 (2022) 2105849.

[18] E. B. Kim, M. S. Akhtar, H. S. Shin, S. Ameen, and M. K. Nazeeruddin, A review on two-dimensional (2D) and 2D-3D multidimensional perovskite solar cells: Perovskites structures, stability, and photovoltaic performances, J. Photochem. Photobiol. C: Photochem. Rev. 48 (2021) 100405.

[19] G. Yansong, L. Zheng, H. Wang, et al, Suppressing wide-angle light loss and non-radiative recombination for efficient perovskite solar cells, Nat. Photon., 2025, 1-8.

[20] S. Ahmad, J. J. Baumberg, G. Vijaya Prakash, Structural tunability and switchable exciton emission in inorganic-organic hybrids with mixed halides, J. Appl. Phys. 114 (2013) 233511.

[21] S. Ahmad, P. K. Kanaujia, W. Niu, J. J. Baumberg, and G. Vijaya Prakash, In Situ Intercalation Dynamics in Inorganic-Organic Layered Perovskite Thin Films, ACS Appl. Mater. Interfaces, 6 (2014) 10238.

[22] M. Adnan, K. N. Rao, J. N. Acharyya, D. Kumar, K. M. Dehury and G. Vijaya Prakash, Synthesis, Structural, Linear, and Nonlinear Optical Studies of Inorganic–Organic Hybrid Semiconductors $(R - C_6H_4CHCH_3NH_3)_2PbI_4, (R = CH_3, Cl)$, ACS Omega, 4 (2019) 19565-19572.

[23] M. Adnan, P. K. Kanaujia and G. Vijaya Prakash, Laser-induced inter-ion migration and the effect of different long alkylammonium halide functionalization on $CH_3NH_3Pb(Br_xI_{1-x})_3$ colloidal nanoparticles, Appl. Surf. Sci., 526 (2020)146789.

From Molecules to Megawatts: Let Us Talk About Green Hydrogen

Adiba and Tufail Ahmad
Department of Physics, Aligarh Muslim University, Aligarh, UP, India-202002

1 Introduction

The quest for clean and sustainable energy has never been more crucial. As the world seeks to combat climate change, pollution, and dwindling fossil fuel reserves, green hydrogen is emerging as a beacon of hope. But what exactly is green hydrogen, and how can it help power a cleaner, more sustainable future? In this article, we will take a detailed yet accessible journey from the basic molecules of hydrogen to the megawatts of energy it can generate, examining how green hydrogen might revolutionize the energy sector.

2 What is Green Hydrogen?

At its core, hydrogen is the most abundant element in the universe, consisting of one proton and one electron. It exists in the form of H_2, a diatomic molecule. Hydrogen is a highly versatile element that can be used as fuel, either in its pure form or by combining it with other elements. However, most of the hydrogen we use today is not environment friendly. It is known as "gray hydrogen," primarily produced from fossil fuels through processes like steam methane reforming, which releases carbon dioxide (CO_2), a potent greenhouse gas[1].

In contrast, *green hydrogen* is produced through electrolysis, where water (H_2O) is split into hydrogen and oxygen using renewable electricity[2]. The key difference is that this process does not emit any greenhouse gases, provided that the electricity used is sourced from wind, solar, or other renewable means. The hydrogen produced in this way is considered clean, making green hydrogen a promising candidate for reducing our dependence on fossil fuels.

3 The Electrolysis Process: Breaking Down Water

Green hydrogen is produced through a process called electrolysis, where an electric current is passed through water to separate it into hydrogen and oxygen. The overall reaction can be represented as:

$$2H_2O(l) \rightarrow 2H_2(g) + O_2(g)$$

Electrolysis occurs in an electrolyzer, which consists of two electrodes (an anode and a cathode) submerged in water[3]. When a direct current (DC) is applied, water molecules dissociate at the electrodes. At the anode, oxygen gas is released, while hydrogen gas is collected at the cathode.

There are different types of electrolyzers, such as:

- **Alkaline Electrolyzers:** The most common type, utilizing an alkaline solution as the electrolyte[3].
- **Proton Exchange Membrane (PEM) Electrolyzers:** These use a solid polymer membrane, offering faster response times and higher efficiencies, making them ideal for renewable energy integration[4].
- **Solid Oxide Electrolyzers:** These operate at high temperatures (up to 800°C) and can achieve high efficiencies but require more complex systems[5].

4 How Green Hydrogen Fits into the Energy Mix?

One of the most compelling reasons for the global interest in green hydrogen is its versatility. Unlike electricity, which must be consumed immediately or stored in batteries, hydrogen can be stored as a gas, liquefied, or chemically bound in molecules like ammonia. This ability to store energy is essential because renewable sources such as wind and solar produce power intermittently. By using excess renewable electricity to produce green hydrogen, we can store that energy and use it later, when needed, either to generate electricity or to fuel other sectors.

Here are some key ways, green hydrogen can con-

tribute to the energy transition:

1. **Electricity Generation:** Hydrogen can be used in fuel cells and devices that convert chemical energy into electricity through a reaction between hydrogen and oxygen[6]. Fuel cells have high efficiencies and emit water vapor only, making them ideal for clean electricity generation. Hydrogen can also be burned in turbines, replacing natural gas in power plants.

2. **Transportation:** One of the most exciting applications of green hydrogen is in transportation, particularly in fuel-cell electric vehicles (FCEVs). Unlike battery-electric vehicles that store electricity in batteries, FCEVs produce electricity on demand by reacting stored hydrogen with oxygen from the air in a fuel cell[7]. This process emits only water, making it zero-emission. Hydrogen vehicles are appropriate for heavy-duty applications like buses, and trucks, because they have a longer range and require less time to refuel than battery-electric vehicles[8].

3. **Industrial Applications:** Many industries rely on hydrogen for chemical processes, such as refining, steelmaking, and ammonia production. Traditionally, this hydrogen has been produced from fossil fuels, but green hydrogen can replace these carbon-intensive processes, reducing emissions from some of the hardest-to-decarbonize sectors.

4. **Heating and Cooling:** Hydrogen can be used in gas grids to replace or supplement natural gas for heating. It can also play a role in central heating systems, where heat is distributed to buildings through a network of pipes. This could dramatically reduce carbon emissions from residential and commercial buildings[9].

5 India and the Green Hydrogen Revolution

India, with its burgeoning energy demand and growing commitment to sustainability, is positioning itself as a major player in the global green hydrogen economy. Recognizing the strategic importance of green hydrogen, the Indian government has launched the **National Green Hydrogen Mission**, with a focus on making the country a global hub for green hydrogen production and export.

1. **Abundant Renewable Energy Potential:** India has vast renewable energy resources, including some of the world's largest solar and wind farms. The government aims to use this renewable capacity to power electrolyzers, making green hydrogen production economically viable. By 2030, India plans to achieve 500 GW of renewable energy capacity, a significant portion of which will contribute to green hydrogen production[10].

2. **Decarbonizing Hard-to-Abate Sectors:** Green hydrogen offers India a unique opportunity to decarbonize its industrial sectors, which account for a significant portion of its greenhouse gas emissions. The steel, cement, and fertilizer industries are prime candidates for green hydrogen adoption, particularly given India's status as one of the largest producers of steel and fertilizers globally[11].

3. **Energy Security and Export Potential:** India imports a large share of its energy in the form of oil and natural gas. Scaling up green hydrogen production could enhance energy security by reducing dependence on fossil fuel imports. Additionally, India is well-positioned to become a major exporter of green hydrogen and its derivatives, such as ammonia, to energy-deficient regions[12].

4. **Policy and Investment Support:** The National Green Hydrogen Mission, backed by an investment of INR 19,744 crore (around $2.4 billion), aims to produce 5 million tons of green hydrogen annually by 2030. This includes subsidies for electrolyzers, R&D initiatives, and the creation of hydrogen hubs. Indian companies like Reliance Industries, Indian Oil Corporation, and Adani Enterprises are investing heavily in green hydrogen projects, signalling strong private sector support[13].

5. **Global Collaborations:** India has been actively collaborating with international partners to boost its green hydrogen capacity. For instance, partnerships with Germany, Australia, and Japan are facilitating technology transfer, knowledge sharing, and investment in hydrogen projects. These collaborations are crucial for overcoming technical and financial barriers.

6 Challenges in Scaling Green Hydrogen in India

While the prospects are promising, India faces challenges similar to those encountered globally, including high costs, infrastructure gaps, and efficiency losses. The initial capital costs for electrolyzers and renewable energy installations remain a barrier. Furthermore, the lack of hydrogen-specific pipelines, storage facilities, and fuelling stations hinders large-scale deployment. Addressing these challenges will require sustained policy support, technological innovation, and public-private partnerships.

7 The Road Ahead: Global and Indian Initiatives

Despite these challenges, governments and industries worldwide are actively promoting green hydrogen as part of their climate action plans. India is emerging as a key player in this movement, leveraging its renewable energy potential, industrial base, and strategic location to become a leader in the green hydrogen economy.

Globally, countries like the European Union, Japan, and the United States have announced ambitious green hydrogen plans, while India is making significant strides through the National Green Hydrogen Mission. The convergence of global and local efforts will play a vital role in scaling up green hydrogen adoption, reducing costs, and addressing infrastructure barriers.

8 Conclusions

Green hydrogen has the potential to play a critical role in the global and Indian energy transition. By producing hydrogen from renewable energy sources, we can reduce greenhouse gas emissions, stabilize the grid, and decarbonize sectors that are difficult to electrify. While challenges remain, the combined efforts of governments, industries, and researchers are paving the way for a cleaner, more sustainable future.

India's proactive approach, coupled with its abundant renewable energy resources, positions it as a major player in the green hydrogen revolution. As we advance from the molecular level to megawatts of clean energy, green hydrogen stands out as a promising solution to some of the most pressing energy and environmental challenges of our time.

References

[1] Boretti, A., and Banik, B.K. (2021). Advances in Hydrogen Production from Natural Gas Reforming. Advanced Energy and Sustainability Research 2, 2100097. https://doi.org/10.1002/AESR.202100097.

[2] Tüysüz, H. (2023). Alkaline Water Electrolysis for Green Hydrogen Production. Acc Chem Res 57. https://doi.org/10.1021/ACS.ACCOUNTS.3C00709.

[3] Ehlers, J.C., Feidenhans'l, A.A., Therkildsen, K.T., and Larrazábal, G.O. (2023). Affordable Green Hydrogen from Alkaline Water Electrolysis: Key Research Needs from an Industrial Perspective. ACS Energy Lett 8, 1502–1509. https://doi.org/10.1021/ACSENERGYLETT.2C02897.

[4] Peng, X., Deng, Z., Zhao, X., Li, G., Song, J., Liang, D., Sun, X., Xu, G., Kang, W., and Liu, M. (2022). Experimental and Analytical Study of a Proton Exchange Membrane Electrolyser Integrated with Thermal Energy Storage for Performance Enhancement. International Journal of Photoenergy 2022, 7543121. https://doi.org/10.1155/2022/7543121.

[5] Gaikwad, P.S., Mondal, K., Shin, Y.K., van Duin, A.C.T., and Pawar, G. (2023). Enhancing the Faradaic efficiency of solid oxide electrolysis cells: progress and perspective. npj Computational Materials 2023 9:1 9, 1–14. https://doi.org/10.1038/s41524-023-01044-1.

[6] Shi, L., Liu, D., Lin, X., Cheng, R., Liu, F., Kim, C., Hu, C., Qiu, J., Amal, R., and Dai, L. (2024). Stable and High-performance Flow H2-O2 Fuel Cells with Coupled Acidic Oxygen Reduction and Alkaline Hydrogen Oxidation Reactions. Advanced Materials 36, 2314077. https://doi.org/10.1002/ADMA.202314077.

[7] Osório, G.J., Gough, M., Lotfi, M., Santos, S.F., Espassandim, H.M.D., Shafie-khah, M., and Catalão, J.P.S. (2021). Rooftop photovoltaic parking lots to support electric vehicles charging: A comprehensive survey. International Journal of Electrical Power & Energy Systems 133, 107274. https://doi.org/10.1016/J.IJEPES.2021.107274.

[8] Hassan, Q., Azzawi, I.D.J., Sameen, A.Z., and Salman, H.M. (2023). Hydrogen Fuel Cell Vehicles: Opportunities and Challenges. Sustainability 2023, Vol. 15, Page 11501 15, 11501. https://doi.org/10.3390/SU151511501.

[9] Renewable Gases – Hydrogen in the Grid – Bioenergy https://www.ieabioenergy.com/blog/publications/renewable-gases-hydrogen-in-the-grid/.

[10] India eyes 500 GW renewable power by 2030 - The Economic Times https://economictimes.indiatimes.com/industry/renewables/india-eyes-500-gw-renewable-power-by-2030/articleshow/114242361.

[11] Green Hydrogen Adoption in Fertilizer Manufacturing: Opportunities and Challenges — WRI INDIA https://wri-india.org/blog/green-hydrogen-adoption-fertilizer-manufacturing-

opportunities-and-challenges.

[12] India's Ambition to be an Export Hub of Green Hydrogen - Current Affairs https://www.nextias.com/ca/current-affairs/22-11-2024/indias-ambition-to-be-an-export-hub-of-green-hydrogen.

[13] https://www.india-briefing.com/news/india-sees-numerous-bids-for-government-incentives-under-us2-billion-green-hydrogen-scheme.

Trace Element Analysis

Lalit Bhardwaj
Department of Physics, Aligarh Muslim University, Aligarh, UP, India-202002

A trace element is a very low concentration chemical element in a given sample. Trace elements concentrations broadly range between 1 to 100 parts per million (ppm). In the IUPAC Compendium of Chemical Terminology, its boundaries are described as "Any element having an average concentration of less than about 100 parts per million atoms or less than 100 μg/g" [1]. Now with the improved analytical detection techniques we can go beyond these boundaries in which concentrations range is below ppm and such a very low concentration element is termed as ultra trace.

Every material has different elemental composition and knowing exactly about this composition can give us information about the origin and quality of material. Study of these trace element is important because even presence of such a very low levels of chemical elements may change the physical, electrical and other characteristics of sample. Like, in material processing various contaminations can be introduced into the sample due to airborne particles (dust, aerosols), humidity (moisture-induced oxidation), impure precursor and due to reaction byproducts.

Managing and comprehending the effects of chemical contamination on advanced materials is very crucial and important, and this can be achieved through Trace Elemental Analysis (TEA). Conducting thorough examinations of raw materials before production and continuous testing during critical stages of manufacturing can assist in recognizing and eradicating sources of undesirable impurities in the final products [2]. TEA helps scientists to determine these trace elements in a sample. It can be used in many fields, like environmental monitoring, toxicology, forensics and food safety etc. [3].

In the past, the detection of trace elements was accomplished using gravimetric methods that involved analysing large sample sizes. For instance, to identify less than 10 ppm of gallium in aluminium, a sample size of 50 g was necessary. Fire assay techniques for noble metals still necessitate samples ranging from 5 to 100 g.

Potentiometric titrations for measuring iodine, silver, and similar elements, as well as the extractive titration of heavy metals by dithizonates into organic solvents for quantification, were occasionally employed in higher levels of trace analysis. However, these methods were often time-intensive, required significant labour, and needed an analyst with considerable expertise [4].

The trace element analysis method can broadly be categorized into two categories

- Destructive Technique and
- Non-Destructive Technique

The Destructive Techniques primarily pertain to optical spectrometry, but also encompass methods like polarography and ion chromatography. Similarly, the Non-destructive Technique can generally be divided into two primary categories: non-nuclear analytical techniques (non-NAT) and nuclear analytical techniques (NAT).

Destructive Techniques mainly focuses on preparing samples in solution, which often results in enhanced homogeneity and reduced matrix interference in many situations. However, the analytical data for Destructive Techniques are usually presented based on solutions, necessitating the consideration of dilution factors to obtain actual performance figures, but the Non-destructive Technique (NDT) does not require the consideration of such factors because it is based on solid samples [4].

Nuclear analytical techniques (NAT) typically offer significant benefits compared to alternative methods. Here, we will focus on two methods: Neutron Activation Analysis (NAA) and Particle-Induced X-ray Emission (PIXE).

1 Neutron Activation Analysis (NAA)

Neutron Activation Analysis (NAA) stands out as precise analytical methods employed for the quantitative analysis of major, minor, and trace elements of interest. This technique was firstly introduced by George de Hevesy and Hilde Levi in 1936. Traditional NAA coupled with Prompt Gamma ray NAA (PGNAA) can analyze up to 70 elements, ranging from Hydrogen to Uranium. This NAA

technique quantifies the total concentration of an element within sample matrices, disregarding its chemical or physical state and requiring no sample pre-treatment. NAA also allows for the examination of non-radioactive tracers that are introduced into biological, chemical, or industrial processes to aid in process identification and optimization [5,6].

In the Neutron Activation Analysis (NAA), a small portion of the material undergoing evaluation is subjected to a stream of thermal neutrons (typical energy is 0.025eV) emitted from a nuclear reactor. When the incoming neutrons interact with the sample nuclei then through the neutron capture (n, γ) reaction, stable element nuclei can be transformed into radioactive ones, which lead to the formation of compound nucleus. The excitation energy of the resulting compound nucleus is determined by the binding energy of thermal neutrons interacting with the nucleus. Many of these resultant radioactive nuclei decay by emitting beta particles followed by emission of gamma radiation, and the emitted gamma rays are specific to the respective decay process. By accurately measuring the energies of the gamma rays produced after the sample is taken out from the reactor and analysed with a detector (typically an HPGe detector is used), one can ascertain the activity or count of gamma rays of particular energy. The total number of counts in the photo peak are directly related to the disintegration rate of the radionuclide, which is itself proportional to the concentration of the parent isotope (target nucleus) present in the sample. Therefore, gamma ray measurements offer an assessment of the overall concentration of the parent element [6,7]. The processes involved in the NAA are shown below in Fig. 1.

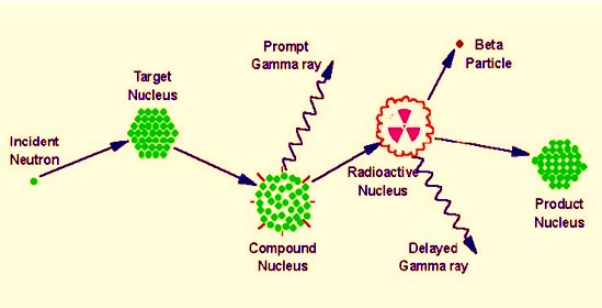

Fig. 1: *Schematic diagram for the Neutron Activation Analysis*

The activity results from neutron capture is given as

$$A' = 0.602 \frac{m}{A} \sigma \Phi (1 - e^{-\lambda t})$$

Here A' is the activity in decays per second, m is the mass of the isotope in gram, A is the mass number of the isotope, Φ is the neutron flux in $neutron/cm^2/s$, σ is the neutrons cross section in barns, λ is decay constant and t is the irradiation time. When all the factors that influence the induced activity are known, the mass of the element (m) can be derived from the observed radioactivity using mentioned equation. The higher the activity, the greater is the detection sensitivity for a specific element.

2 Particle-induced X-ray emission (PIXE)

Particle-induced X-ray emission (PIXE) is also utilized for analysing small quantities of elements. This method was initially introduced in 1970 by Sven Johansson from Lund University in Sweden. In this process, a thin layer of the material is placed in the target region of an accelerator and is bombarded with protons, alpha particles, or even heavy ions. The interaction between the incoming particles and the target can lead to ejection of an inner electron (K-shell or L-shell). After a vacancy is created, it is rapidly filled by the outer electrons in the atom, producing an X-ray in the process.

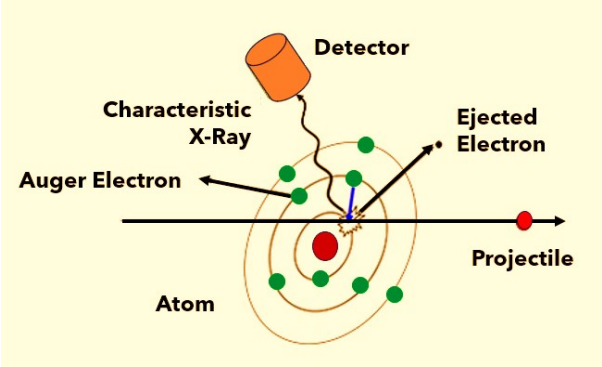

Fig. 2: *Schematic diagram for the PIXE*

The energies of K- and L-shell X-rays vary with the atomic number Z, allowing us to identify the elements present in the sample by analysing the emitted X-rays. Due to the limited range of charged particles within matter and the low energies of emitted X-rays (10-100 keV), it is essential to use thin samples, so that X-rays can penetrate through the sample and thus can reach detector. Recent advancements in PIXE utilizing focused beams (as small as 1 μm) have enabled microscopic analysis. This refined approach, known as microPIXE, allows for the assessment of trace element distribution across a wide variety of samples. Additionally, a related method, particle-induced gamma-ray emission (PIGE), can be employed to identify certain light elements.

The cross sections for ionization of the K-shell in

the PIXE changes gradually, unlike the situation seen with the capture of thermal neutrons in the NAA method. For lighter elements, the cross section is approximately 100 barns, but it drops to less than 1 barn for heavier elements. Consequently, the sensitivity of PIXE diminishes as the atomic number (Z) of the target increases, though achieving quantitative results is still feasible up to higher atomic number element like lead (Pb) [7,8].

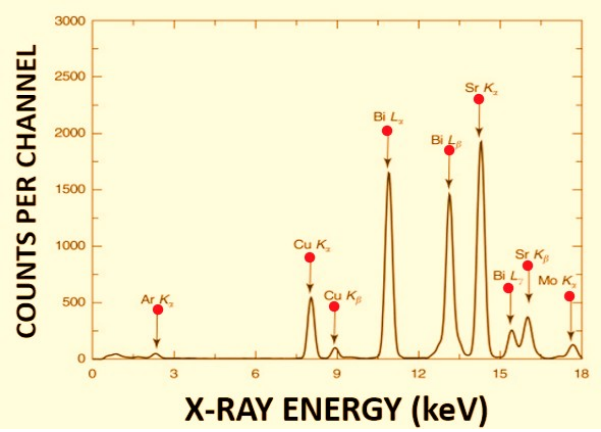

Fig. 3: *A typical spectrum obtained in PIXE experiment*

A standard X-ray spectrum acquired during the PIXE experiments is illustrated in the Fig. 3. This figure demonstrates that different trace elements can be recognized by their distinct characteristic lines. The intensities of these X-ray lines are utilized to calculate the amount of trace elements present in the sample.

This method is similar to NAA regarding sensitivity, and in many cases, it may outperform NAA. Additionally, NAA faces selectivity constraints due to isotopes that may possess low cross sections or no gamma emissions. In contrast, PIXE does not encounter these limitations—virtually all elements can be detected with comparable sensitivity. One drawback in the PIXE is that the X-ray spectrum includes various components of the K and L lines, which can create interference and complicate the analysis if the detector is not able to resolve different peaks [7].

References

[1] https://goldbook.iupac.org/terms/view/T06421

[2] https://www.eag.com/services/materials/trace-elemental-analysis/

[3] https://www.azomining.com/Article.aspx?ArticleID=1511

[4] http://books.rsc.org/books/monograph/chapter-pdf/1728424/bk9781839165726-00001.pdf

[5] https://nrp.ne.ncsu.edu/nuclear-services/neutron-activation-analysis/

[6] https://barc.gov.in/ebooks/9788195473328/paper18.pdf

[7] Krane, K. S. (1988). Introductory nuclear physics (pp. 802–808). Wiley.

[8] https://en.wikipedia.org/wiki/Particle-induced_X-ray_emission

Liquid crystal based thermometers

Shubham Gupta, Arbaz Khan and Shikha Chauhan
Department of Physics, Aligarh Muslim University, Aligarh, UP, India-202002

1 Introduction

The primary distinction between the two prevalent condensed matter phases, crystals and liquids, is that the molecules in a liquid are not arranged in order, but molecules in a crystal are arranged in regular and repeated patterns. Crystals generally exhibit positional and orientational order, which means that the molecules are restricted in their ability to align their molecular axes in certain directions and to occupy certain locations within a lattice. In contrast, molecules in liquid have axes that rotate continuously and molecules move randomly throughout the container. Notably, nature also contains phases that are less ordered than normal crystals but more ordered than liquids, referred to as liquid crystal phase [1]. The term "liquid crystal" (LC) refers to its unique blend of characteristics in between liquids and crystals. The LCs have dielectric, electrical, and optical anisotropy, meaning thereby that their characteristics change with direction, just like crystalline solids. Simultaneously, LCs have characteristics like fluidity and molecular mobility which is common with isotropic liquids [2].

LC was invented by the Austrian botanist Friedrich Reinitzer in the year 1888. He noticed that cholesteryl benzoate exhibited two different melting points upon heating from a crystalline to liquid state. Reinitzer observed that the crystal transforms into a hazy liquid at 145.5°C after raising the temperature of a solid sample. He raised the temperature even more, and the substance transformed at 178.5°C into a translucent and clear liquid as shown in Fig. 1.

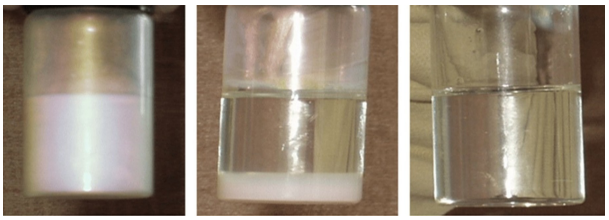

Fig. 1: *Transformation of a LC material occur at specified temperature.*

The entire process was reversible and the turbid liquid's colour varied from red to vivid blue-violet to pale blue. Otto Lehmann, an experienced crystallographer, obtained Reinitzer's samples to validate his findings and improve experimental accuracy. Between 1890 and 1900, Lehmann replicated the phenomena observed by Reinitzer, referring to this new substance with terms such as "flowing crystal" or "viscous LCs" or "crystalline fluid" [3].

2 Classification of LCs

The LCs are classified into several groups and subgroups according to their formation method, molecular configuration and molecular morphology within the materials. The most prevalent type of molecule observed in LC phases is rod-shaped, which means that a molecule's one axis is significantly longer than its other two axes. These materials, known as calamitic LCs.

Disc shaped molecules can also contribute to the formation of LCs, which have one shorter axis than other two. Such molecules are known as discotic LCs, and require stiffness in the core region of molecule. Calamitic and discotic LCs, also known as thermotropic LCs, are stable at specific temperatures.

Thermotropic LCs shows their liquid crystalline phase within a specific temperature array, which is between the melting point and the transition temperature. When temperature varies, these LCs frequently show a range of unique phases. Thermotropic LCs are classified into three types Nematic, Smectic, and Cholesteric LC as shown in Fig. 2.[1]

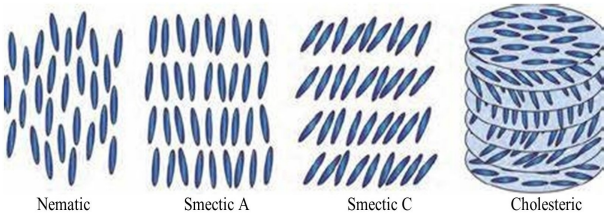

Fig. 2: *The schematic arrangement of molecules in Nematic, Smectic and Cholesteric phases.*

The nematic phase is a single dimensionally organized, adaptable fluid in which molecules have orientational order nevertheless lack long range po-

sitional order. During this phase, the rod shaped molecules are aligned parallel to their long axes and generally oriented in the same direction. The term "nematic LCs" (NLCs) originates after greek word nema, meaning "thread", which denotes thread like texture observed under a polarizing microscope.

In the smectic phase, the molecules are systematically arranged within each layer, forming a spatially periodic structure. The word smectic is taken from greek word 'smegma', which signifies soap. There are many smectic phases but two most common phases are smectic A and smectic C phase. In the smectic A phase, molecules are ordered in layers with their long axes oriented perpendicular to the layer plane. In the smectic C phase, molecules are arranged in distinct layers, with their long axes tilted relative to the layer plane. The tilt angle is defined as angle between long molecular axis and the director perpendicular to the smectic plane [2].

Cholesteric LCs are also coined as chiral NLC, consist of optically active molecules. In this phase, the director adopts a helical structure instead of remaining stationary, which introduce chirality into the structure. One of the most essential aspects of chiral NLCs is pitch, which is the distance required to rotate the director through an angle of 2π. This chiral phase shows different colours when exposed to white light having wavelengths equal to the pitch value of the mesogen. Its twisted helical shape gives it a variety of optical properties that can be used to make temperature sensors, such as clinical thermometers, since even a slight change in temperature can substantially change the colour and pitch value [3]. There is another category of molecules exhibits a LC phase solely when mixed with a solvent, these are referred to as lyotropic LCs. These LCs are especially common in biological systems are industrial products like soap, detergents and lipid bilayers [1].

3 Applications of LCs

Owing to their distinctive properties, LCs are widely used in electro-optical display devices, temperature sensor, biosensors, chemistry, space engineering, biology, food science, and pharmacology. Thermotropic LCs are commonly used in electro-optical display such as flat-panel televisions, laptop screens, telecommunications devices, calculators and wristwatches. Lyotropic LC systems are widely used in the cosmetics sector and are essential for cleaning procedures. The structural arrangement of basic biomolecules such as DNA, proteins, and polysaccharides is reflected in the chiral nematic phase, highlighting the importance of chiral helical structures in sustaining vital biological processes. Fig. 3 shows some of the components, functions, features, and applications of LCs [4].

Thermotropic LCs are widely used in the temperature sensors. One kind of temperature sensor where the colour of LCs varies with temperature is a LC thermometer or plastic strip. Typically, the temperature-sensitive material is a cholesteric LC compound that changes colour when activated by temperature. Upon activation, the temperature-sensitive material emits or reflects visible radiation, indicating the temperature.

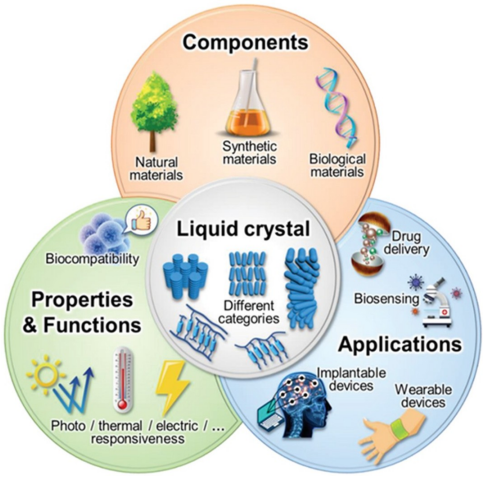

Fig. 3: *Components, properties and applications of LC.*

4 Need of LC based thermometer

Thermometers are essential for scientific research and daily activities, enabling precise temperature measurement. They are available in various types, and are based on distinct principles. Mercury and alcohol thermometers have historically been used to monitor human body temperature. These are operated on the principle of thermal expansion, where changes in temperature lead to the expansion or contraction of the liquid within, which is then indicated on a calibrated scale. Traditional mercury thermometers use a glass tube, which increases the risk of injury from glass fragments if broken and of mercury poisoning. Digital thermometers utilise electronic sensors to detect temperature and present the results on a digital display, allowing for quick and accurate readings. They require batteries to function which may run out at inconvenient times and extreme temperature or humidity can affect their performance or damage the electronics [5]. Infrared thermometers assess the infrared radiation emitted by an object to ascertain its temperature, making them particularly suitable for non-contact measurements. They are not ideal for continuous temperature monitoring over time and dust, steam,

smoke or other airborne particles can interfere with infrared readings [6].

To get rid of the problems from conventional thermometers, we need to utilize alternative thermometer that is simple to use and does not cause damage, such as a LC thermometer. LC thermometers are easy to use without any calibration or comprehensive instructions because they are made from non-toxic, biodegradable materials that provide no risk of environmental pollution or poisoning. LC thermometers are appropriate for applications that need quick detection, while adhesive strips and other flexible formats make them perfect for wearable applications and curved or uneven surfaces and they reduce hazards in places such as homes, laboratories and hospitals because they are difficult to break [7].

5 Cholesteric LC based thermometers

A non superimposable mirror image of an object or molecule is called chiral, a term derived from the greek word for handedness. For instance, while a human hand exemplifies chirality, a coffee cup does not. In the context of chemistry, chirality typically indicates that a molecular structure is asymmetric and possesses handedness. In most cases such chirality is generated by their being four different structural components attached to a tetrahedral, sp^3 carbon atom (often describes as a chiral centre). Four such different units can be arranged in two ways, generating two compounds (enantiomers) that are mirror images of each other. One stereochemical configuration is termed S and the other enantiomer is termed R. For example, 2-octanol is chiral and is commonly used in the synthesis of chiral LCs one isomer is (S)-2-octanol (1a) and the other isomer is (R)-2-octanol (1b) as shown in Fig. 4.

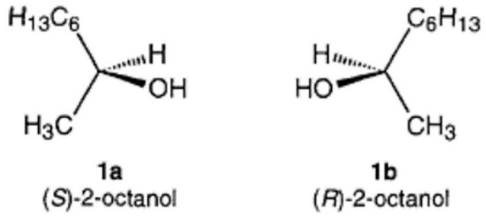

Fig. 4: *Enantiomers of 2-octanol.*

Both enantiomers are identical except for the way in which the structural components are arranged in space. This different arrangement of functional groups in space is responsible for optical activity, i.e., an enantiomer will rotate the plane of plane polarised light, its mirror image will produce the same magnitude of rotation but in the opposite direction. A 1:1 mixture of enantiomers is termed racemic and will not generate a rotation of plane polarised light. Materials composed of chiral molecules are particularly noteworthy, especially those exhibiting organic activity. Additionally, cholesteric molecules that form LC phases are also regarded as exceptional & unique.

In certain fluid environments characterized by well-organized liquid crystalline phases, the chirality of individual molecules leads to the emergence of chirality in the macroscopic arrangement of the LC phase, referred to as form chirality. The cholesteric liquid crystalline molecules arrange themselves into an unsymmetric, cholesteric configuration that resembles a helix. This helical arrangement possesses a distinct handedness; for example, one enantiomer will generate a sinistral helix, whereas the other enantiomer will generate a dextral helix. Shape chirality is a direct consequence of molecular chirality, enabling the precise plan of LC molecules to fulfil specific application requirements. For instance, certain molecules can be tailored to achieve a significantly long helical pitch, while alternative designs may result in a shorter helical pitch. The investigation of chirality within LCs constitutes a broad and captivating area of research that is both intricate and important. In recent years, there has been a notable increase in research dedicated to chirality in LCs, which is essential for various technological innovations.

The cholesteric nematic phase can be induced with introducing a little amount of a cholesteric substance (which does not have to be in liquid crystalline form) into a nematic material. It is considered that the cholesteric dopant establishes a cholesteric environment for the surrounding for molecules which are not cholesteric, resulting in the formation of a helical macrostructure.

6 Working of LC thermometer

The inherent asymmetry of fundamental molecules leads to a gradual and uniform regular change of the director (the average direction of the long axes of all the molecules $\hat{n}$). This ongoing modification of director results in a helical structure with a distinct, temperature reliant pitch. Therefore, the cholesteric nematic phase demonstrates a curl along a singular axis. On higher temperatures, the molecules exhibit amplified internal energy, which causes a greater angle of director alteration and a tighter pitch. In contrast, when the temperature drops, the pitch length grows. On the other hand, there are occasions when the anticipated relationship between pitch variation and temperature does not manifest.

The helical arrangement can selectively reflect light at wavelengths that correspond to the helical pitch length the cholesteric nematic material must be oriented such that the helical axes align with the direction of light travel. When length of pitch grows and becomes closer to the wavelength of visible spectrum, certain colours are reflected. The effect is based on the temperature dependence of the gradual change in director orientation between successive layers, which modifies the pitch length resulting in alteration of wavelength of reflected light according to the temperature. The angle at which the director changes can be made larger, and thus tighten the pitch, by increasing the temperature of the molecules, hence giving them more thermal energy. Similarly, decreasing the temperature of the molecules increases the pitch length of the chiral nematic LC. This principle is fundamental to the effective commercial use of cholesteric nematic (chiral) materials in thermochromic thermometer devices and various products with the aim of altering colour with temperature, including textiles, inks, and paints [1].

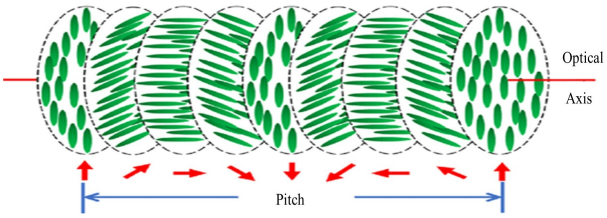

Fig. 5: *Schematic diagram of orientation changes of cholesteric LC with temperature.*

7 LCs thermometer strips

The predominant form factor for LCs thermometers consists of self-adhesive strips that feature a sequence of temperature sensitive components. These components are composed of micro encapsulated thermochromic LCs positioned against a black backdrop. Each LC component is meticulously designed with a specific pitch, often enhanced with additives, enabling successive elements to change to a green hue in response to incremental temperature variations. Consequently, as the temperature increases, these elements illuminate to display the corresponding number that is permanently affixed beneath them. LCs exhibit a black appearance both below and above their specified temperature range while displaying a spectrum of colours resembling a rainbow with green being the midpoint, as the temperature fluctuates within this range. As one segment of the LC transitions to green, the segment above it may take on a subtle tan hue, while the segment below may shift to a faint blue, contingent upon the molecular engineering involved [8].

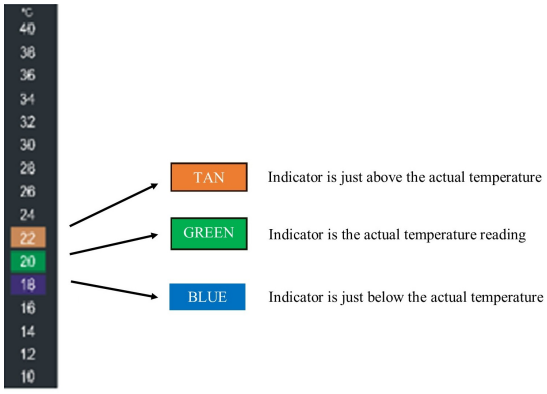

Fig. 6: *LC thermometer strips.*

The illustration below depicts the composition of a standard liquid crystalline strip, highlighting the unlike layers, through LCs situated within the central layer. The white realistic print features designated numbers, while the black backing film is positioned beneath the LCs. It is important to note that the LCs are the sole component of the assembly that alters colour, sequentially illuminating the white numbers above them as the temperature rises.

Fig. 7: *Schematic diagram of thermochromic LC label construction.*

8 Features of LC thermometers

Colour changing LC thermometers show temperature as colours, with each colour corresponding to a specific temperature. The colours change reversibly, so they can respond to both increases and decreases in temperature. Reusable LCs can return to their original state after being exposed to temperature changes, making them reusable and long-lasting. LC thermometers are safer than mercury-in-glass thermometers. LC thermometers are used in a variety of applications, including aquariums, home brewing, and mood rings. LC thermometers can be customized to meet specific requirements, such as size, shape, colour, and temperature range [9].

9 Applications of LC based thermometer

LC based thermometers exploit the thermochromic properties of LC, which exhibit distinct colour

changes at specific temperature ranges. These thermometers are widely used for their ability to provide quick, non-invasive, and visually interpretable temperature readings. In the medical field, they are employed in forehead thermometers and fever strips to monitor body temperature without discomfort, especially useful for infants and during pandemics. In industrial settings, they help monitor surface temperatures of machinery, pipelines, and electronics, ensuring operational safety and efficiency. LC thermometers are also used in consumer products, such as aquarium strips and bath thermometers, for easy monitoring of water temperature. In laboratories and educational contexts, they demonstrate thermotropic behaviour and phase transitions. Additionally, they play a crucial role in cold chain logistics, ensuring temperature-sensitive products like vaccines and perishables remain within safe temperature limits during transportation and storage.

References

[1] P.J. Collings and M. Hird, Introduction to Liquid crystals chemistry and physics, Taylor and Francis, UK (1997).

[2] D. Demus, J.Goodby, G.W. Gray, H.W. Spiess and V. Vill, Handbook of Liquid crystals, Wiley VCH, Weinheim, (1998).

[3] S. Mohanty, Liquid crystals - the 'fourth' phase of matter, Resonance, 8,52, (2003).

[4] S. Singh, Liquid crystals fundamentals, World Scientific, Singapore, (2002).

[5] S.A. Raj, S.Senith and B.K.Sai, Digital Thermometers: Its Types, Utilities and Global Trade Prospects for India, Conference Series,1937, 012016, (2021).

[6] Zhao, Yuanzhe, Bergmann and H. M. Jeroen, Non-Contact Infrared Thermometers and Thermal Scanners for human Body Temperature Monitoring: A Systematic Review, Sensors, 23,7439, (2023).

[7] M. Catherine and Luk, Liquid crystal temperature indicator for measuring human body temperature, U.S. Patent No. 4,302,971, (1981).

[8] A. Seeboth, R. Ruhmann and O. Muhling, Thermotropic and thermochromic polymer-based materials for adaptive solar control, Materials, 3, 5143, (2010).

[9] Miskovic, Vanja, E.Malafronte, C.Minetti, H.Machrafi, C.Varon and C.Saverio, Thermotropic Liquid crystals for temperature mapping, Frontiers in Bioengineering and Biotechnology, 10, 806362, (2022)

Machine Learning in Liquid Crystal Research

Asif Ali Ansari and Jai Prakash
Department of Physics, Aligarh Muslim University, Aligarh, UP, India-202002

Everything we see and use on a daily basis, from the gadget we are using to read to our morning coffee, is made of matter. The three states of matter that we frequently come into contact in everyday life are solid, liquid and gas. Certain environmental conditions, such as temperature and pressure, can change these three states of matter from one form to another. For example, increasing the temperature may change ice, which is a solid, into water, which is a liquid. Phase transitions, which signify modifications in structure and characteristics, are another way to identify the state of matter. The many shapes that matter may take are referred to as its states. One of the phases of matter, solids are defined by high viscosity and strong atomic bonding, which give them a hard shape. A solid has a fixed volume and a stable, definite shape because its particles (ions, atoms, or molecules) are packed closely together and are subject to forces that prevent them from moving freely; it can only change shape when it is broken or cut. A liquid is a nearly incompressible fluid that conforms to the shape of its container but keeps a constant volume regardless of pressure; a solid turns into a liquid when it is heated above its melting point and the pressure surpasses the substance's triple point. The average distance between adjacent molecules is significantly greater than the size of the molecules; a gas has no distinct shape or volume and fills the entire container in which it is found; and the molecules in a gaseous state have enough kinetic energy that the effect of intermolecular forces is minimal or nonexistent [1]. According to the general theory, all matter typically has two points: a melting point, when it becomes liquid, and a boiling point, where it becomes gas. An excellent illustration of this viewpoint is water. At 0°C it melts, and at 100°C it boils and turns into steam, which is water in gaseous form.

1 Liquid Crystals: An Introduction

In the year 1888, Fredrich Reinitzer, An Austrian botanist, was attempting to determine the proper formula and molecular weight of cholesterol by doing experiments on a material based on it. He was surprised to discover that this material appeared to have two melting points when he attempted to accurately measure the melting point, which is a crucial sign of a substance's purity. The solid crystal dissolved at 145.5°C to form a hazy liquid, which persisted until 178.5°C, when it abruptly cleared to reveal a clear, transparent liquid. Reinitzer first believed that this would indicate that the material had contaminants, but additional purification had no effect on this behavior. Fascinating by this abnormal observation, Reinitzer sent the sample to Otto Lehmann who was a famous German crystallographer. By his careful observations of the melting of the substance using his state-of-the-art microscope with a gas heating stage, Lehmann was convinced that the cloudy state is totally a new state of matter that differs from solid, liquid, and gas. Today this cloudy liquid is known as "liquid crystal" [2]. The double melting phenomenon was discovered by Reinitzer in 1888, which is officially recognized as the year of discovery of Liquid crystals [3].

Liquid crystal (LC) is considered as the fourth state of matter that occurs between solid and liquid. LCs are anisotropic fluids that flow like a liquid but maintain some of the ordered structure of crystals [4]. They have become an integral part of our commercial electronics world, and liquid crystal displays (LCDs) are a key part of most mobile, battery-powered electronic devices. A small electric field can change the orientation of molecules in a layer of LCs which affects their optical properties, this process is termed as electro-optical effect, and it forms the basis for LCDs. LC materials that align either parallel or perpendicular to an applied field can be selected to suit particular applications. The small electric voltages required to orient LC molecules have been a major factor in the commercial success of LCDs [5].

LCs come in a range of phases, with some exhibiting more characteristics of a liquid and others exhibiting more characteristics of a solid. There are two types of LCs: thermotropic, which changes phases with temperature, and lyotropic, which changes phases with the concentration of the LC's primary constituent, mesogen, in the solution. Fig. 1 shows the main phases of thermotropic LCs. The molecules in the nematic phase, which resembles a liquid more than anything else, can align unevenly and be affected by external electric fields or external magnetic fields, just like in a liquid, and these may behave as polarizers for light similar to those in a solid crystal. There is no positional ordering in its molecules;

only orientational ordering is present. Nematic liquid crystals are particularly common in devices, like optical displays and sensors because of these characteristics, making them very practical materials. On the mesoscopic level, directors may be used to represent the local orientation of LC molecules, and this idea is used in many LC studies when examining LCs. The smectic phase is characterized by some positional and orientational ordering and is more analogous to a solid than a liquid. Each director points in the same direction about a set of parallel planes, which further explains the positional ordering of smectic LCs. Here, the smectic phases differentiate in the smectic A phase, the smectic directors point perpendicular to the plane, while in the smectic C phase, they point in a different direction.

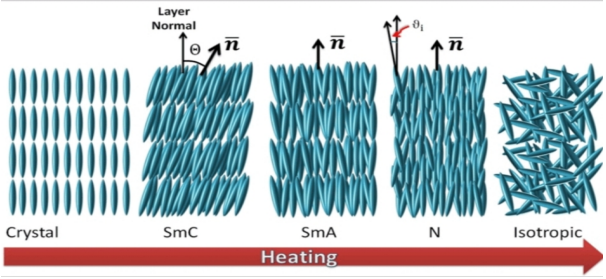

Fig. 1: *Various phases of thermotropic liquid crystals and how they change from solid crystals to isotropic liquids as the temperature rises.*

When heated excessively, the LCs will become conventional liquids, because they lose all of their molecular ordering, and called the isotropic phase characterized by isotropic motion [6]. However, some LCs also show phases with anisotropic ordering.

There is still much to learn about the physics of LC systems, similar to most other forms of soft matter. Other physical phenomena that are extended to LCs provided the basis for the development of the primary theoretical models used to describe LCs. In theoretical LC research, the Onsager model is a useful theoretical model that was first used to describe equilibrium LC systems through dipole-dipole interactions [7]. Another statistical model for LC systems is the XY model, which was created to help understand more complex systems and phase transitions [8]. But as LC technologies advance, more specialized LCs with certain structural and physical properties are to be desired like the method for figuring out the parameter for nematic order. It takes a lot of time to try, optimize and analyze the properties of LCs for these novel technologies using many conventional experimental techniques, and as the time passes on the amount of work spent using these methods to identify LCs with particular optimized properties will only rise. Consequently, machine learning be introduced as a substitute for these time-consuming experimental techniques [9].

2 Overview of Machine Learning (ML)

Machine learning is a branch of Artificial Intelligence (AI) that uses deep learning and neural networks to let a system learn and grow on its own without explicit programming by supplying it with vast volumes of data. As additional "experiences" are gained, ML enables computer systems to continually adapt and improve. Larger and more diverse information to handle can thereby enhance the performance of these systems. Almost every business activity and sector use ML. Manufacturing automates factories, the retail sector manages inventories and personalizes shopping experiences, the logistics sector optimizes shipping and delivery routes, and ML helps safeguard companies worldwide. ML is used to comprehend the request and assist in determining the outcome when a user speaks to their speaker or smartphone. ML has a wide range of applications which are continuously expanding. The process of ML is shown in Fig. 2.

Over the past three decades, ML has advanced quickly and has been applied in numerous scientific fields to assist in the categorization, identification, and analysis of numerous phenomena, particularly in imaging. Since LCs are birefringent and most of their physical characteristics can be determined with the help of an optical microscope, they have been very popular to study with imaging techniques and subjects for imaging research. Furthermore, the introduction of databases like LCs, an online collection of enormous amounts of LC properties, has facilitated ML with LCs by increasing the availability of large datasets [10]. Some important applications of ML in LCs have been highlighted in subsequent sections:

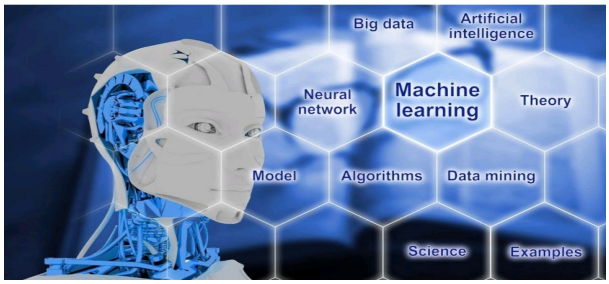

Fig. 2: *Machine Learning Process: From Data Collection to Model Deployment*

3 Classifying Between LCs and Non-LCs

First, a feedforward neural network optimized with 99% accuracy for the training dataset and 83.33% accuracy for the testing dataset, a genetic algorithm

was able to distinguish between LCs and non-LCs using similarly structured organic compounds based on the rigid core and flexible core lengths, molecular diameter, and total weight. To determine if a chemical is an LC or not, machine learning is used to detect connections, mainly by figuring out whether the compounds would demonstrate LC behavior. An algorithm that uses ML was able to differentiate between LCs and non-LCs using a range of molecular descriptors-numbers that could be derived from a mathematical operation from the raw LC structure and the LCs database, with training set accuracy just under 100% and testing set accuracy in the high 80s%. Various ML framework types were tested, including the Support Vector Machine (SVM)[1], k-nearest neighbors (KNN)[2], Random Forest, Adaboost[3], and three Decision Trees with different depths. The Random Forest and SVM models performed better than the others. To determine which set would perform better on the dataset, descriptor sets from the Detector of Recoils and Gammas of Nuclear (DRAGON) and RDKit tools were employed, along with additional molecular fingerprinting inputs [11].

4 Studying Phases of LC and Phase Transitions

Predicting LC phases and phase transitions is a more focused use of ML about LC structure. Another such use has been to differentiate between nematic and smectic-like structures in liquid-crystalline polymers using a model of random forests with order parameters as input features. Sequential Forward Selection, which selects several input characteristics from a collection of the input characteristics that would offer the model the highest accuracy, was used to determine the most practicable order parameters for the examination of prediction across phases [12]. This offers a superior option to manually choose the order parameter or parameters that are most appropriate for categorizing LC system. A ML network made it easier to analyze multistep phase transitions in anisotropic liquid crystal systems by using the machine learning framework developed by Doi et al. [13]. It determine the order parameters required for a complete investigation of the system. By using different combinations of a set of 13 input features that describe the molecular composition and environmental conditions of various liquid crystalline molecules, including temperature, ML models are able to predict the presence of a mesophase for a given material under certain circumstances. The design and investigation of these ferroelectric nematics for potential application for LC systems with extremely high dielectric constants was substantially aided by another study that employed a different dimensionality reduction algorithm with a random forest regression to help correlate structural parameters with the occurrence of a ferroelectric nematic phase [14]. A k-means clustering technique was able to identify the phase of the liquid crystal 12BBAA (4-bromobenzylidene-4'-dodecyloxyaniline) depending on temperature using its infrared spectral data. However, with using a window clustering algorithm, which separates the spectral data into wavenumber ranges (the "windows") and applies k-means clustering analysis to each window to identify the phase in each spectral subset, this research was capable of further investigating the melting of the alkyloxy chains within the compound and extract even more helpful data from the complex infrared spectra.

5 Predicting Structural Dynamics of LCs

Predicting certain structures and dynamics that will emerge in particular circumstances is another use of ML. Considering the quantity of LC systems to which the model may be applied, a study that used genetic algorithms to calculate LC director configurations found which configuration had the least free energy for a range of LC systems, including hybrid cells, 90-degree twist cells, and twisted nematic cells. This method was less time-consuming than the previous manual methods. In a study that used machine learning, similar to Sequential Forward Selection, the pitch and radius of helicoidal trajectories of chiral twist-bend nematic phase LCs were correlated with the pitch and conical angle of the twist-bend nematic phase. This was done using a dimensionality-reducing algorithm and a diffusion map to determine which input features produced the highest accuracy for the model [15].

6 Machine Learning Dynamics of LC Response to External Stimuli

Additionally, machine learning has been utilized to identify certain external stimulants by analyzing the optical response of a liquid crystal to mechanical or chemical stimuli. This directly improves the potential of LCs as mechanical and chemical sensors.

[1]SVM is a supervised machine learning algorithm that is used for both classification and regression tasks. The primary goal of SVM is to find the optimal hyperplane that separates data points of different classes in an N-dimensional space

[2]KNN is a supervised machine learning method employed to tackle classification and regression problems

[3]Adaboost is a framework that uses the accurate portions of generally poorly trained classifiers to theoretically form the ideal classifier through some weight adjustment

Research classified the environment of an LC using an SVM algorithm with 99% accuracy, which is significantly higher than the 60% sensor accuracy attained by conventional methods. To do this feature from the optical image of the LC under the microscope was extracted using Alexnet, and the characteristics were then used as the feature input for the SVM classifier. Building on this work, different research replaced Alexnet with an SVM to forecast utilizing characteristics taken from the more recent pre-trained VGG16 network for image analysis. To achieve the same degree of accuracy as the SVM developed by Cao et al. [16], the classifier needed fewer features, which increased the computing efficiency of this incredibly accurate technique.

7 Future of ML in LC Research

Without any doubt, there is still a tremendous opportunity for new machine learning techniques to be employed in LC research and novel applications of ML to LC research. For example, reinforcement learning, a subset of machine learning in which an agent learns by maximizing its reward given the current condition of the environment. It is utilized in the field of soft matter, such as for the manufacturing of circular-shaped colloidal crystals, demonstrating that reinforcement learning techniques may be beneficial for liquid crystal study as well. Furthermore, reinforcement learning has demonstrated potential in the realm of active nematics using interactions to create desired dynamics in the systems [17]. A Generative Adversarial Network (GAN), which is made up of two networks - a discriminator and a generator - is another kind of algorithm that may be employed in LC Research in the future. The generator is trained to trick the discriminator, while the discriminator is trained to distinguish between actual and AI-generated data. It has already shown promise to use in modeling both passive as well as active liquid crystal structures by simulating particle showers in electromagnetic calorimeters in high-energy physics and creating 3D electrode microstructures [18]. The scientific community's growing interest in GAN and reinforcement learning algorithms opens up a new application of ML in LC research, creating LCs with specific goals in mind. Although Li et al. [14] employed an ML framework to assist in identifying the conditions that would cause a ferroelectric nematic phase to develop but the design of LC was not done using ML. However, it is an appropriate next phase for ML to be broadly used directly in designing LCs and LC mechanisms with desirable characteristics. The growing popularity of GANs and reinforcement learning in the scientific community, including works that utilize ML and GANs to model and produce acceptable properties within a system of materials.

References

[1] Three States of Matter - Solid, Liquid and Gas - Testbook.com

[2] History and Properties of Liquid Crystals https://educationalgames.nobelprize.org/educational/physics/liquid_crystals/history/index.hl

[3] Blinov, L. M.; Chigrinov, V. G.; Patel, J. S. Electro-Optic Effects in Liquid Crystal Materials, 1-46 ; 1995; Vol. 48. doi:10.1063/1.2807983.

[4] Singh, S. Liquid Crystals: Fundamentals.; 2003; Vol. 56, World Scientific.

[5] [P._G._de_Gennes,_J._Prost]_Physics_of_liquid_crys(b-ok.org).pdf.

[6] Huang, CY. (2015). Physics of Liquid Crystals. In: Lee, CC. (eds) The Current Trends of Optics and Photonics. Topics in Applied Physics, 263-271, vol 129. Springer, Dordrecht. https://doi.org/10.1007/978-94-017-9392-6_10

[7] Onsager, L. (1931). Reciprocal relations in irreversible processes. I. Physical Review, 37(4), 405. https://doi.org/10.1103/PhysRev.37.405

[8] Rojas, F., & Rutenberg, A. D. (1999). Dynamical scaling: The two-dimensional XY model following a quench. Physical Review E, 60(1), 212. https://doi.org/10.1103/PhysRevE.60.212

[9] D. Kalinin, J. Abercrombie, The Applications of Machine Learning in the Study of Liquid Crystals: A Review, J. Student Res. 12 (2023) 1–16. https://doi.org/10.47611/jsrhs.v12i1.3983.

[10] Vill, V. (1995). Conception and Realization of a Liquid Crystal Database LIQCRYST. Liquid Crystals Today, 5(3), 6-7. https://doi.org/10.1080/13583149508047608v

[11] Chen, C., Tanaka, K., and Funatsu, K. (2018). Random Forest Model with Combined Features: A practical approach to Predict Liquid-Crystalline Property. Molecular Informatics, 38(4), 1800095. https://doi.org/10.1002/minf.201800095

[12] Mani, K., & Kalpana, P. (2016). An Efficient Feature Selection based on Bayes Theorem, Self Information, and Sequential Forward Selection. International Journal of Information Engineering & Electronic Business, 8(6). https://doi.org/10.5815/ijieeb.2016.06.06

[13] Doi, H., Takahasi, K. Z., Tagashira, K., Fukuda, J., and Aoyagi, T. (2019). Machine learning-

aided analysis for complex local structure of liquid crystal polymers. Scientific Reports, 9(1), 1-12. https://doi.org/10.1038/s41598- 019-51238-1

[14] Li, J., Nishikawa, H., Kougo, J., Zhou, J., Dai, S., Tang, W., ... Aya, S. (2021). Development of ferroelectric nematic fluids with giant ϵ dielectricity and nonlinear optical properties. Science Advances, 7(17), eabf5047. https://doi.org/10.1126/sciadv.abf5047

[15] Coifman, R. R., & Lafon, S. (2006). Diffusion maps. Applied and computational harmonic analysis, 21(1), 5-30. https://doi.org/10.1016/j.acha.2005.07.004

[16] Cao, Y., Yu, H., Abbott, N. L., & Zavala, V. M. (2018). Machine learning algorithms for liquid crystal-based sensors. ACS sensors, 3(11), 2237-2245. https://doi.org/10.1021/acssensors.8b00100

[17] Liu, Y., Zou, Z., Tsang, A. C. H., Pak, O. S., & Young, Y. N. (2021). Mechanical rotation at low Reynolds number via reinforcement learning. Physics of Fluids, 33(6), 062007. https://doi.org/10.1063/5.0053563

[18] Gayon-Lombardo, A., Mosser, L., Brandon, N. P., & Cooper, S. J. (2020). Pores for thought: generative adversarial networks for stochastic reconstruction of 3D multiphase electrode microstructures with periodic boundaries. Computational Materials 6(1), 1-11. https://doi.org/10.1038/s41524-020-0340-7

A Few Popular Software for Tensor Operations

SSZ Ashraf
Department of Physics, Aligarh Muslim University, Aligarh, UP, India-202002

Abstract

Tensors are essential mathematical tools used across disciplines like physics, engineering, and machine learning to represent multi-dimensional data and complex relationships. This brief article explores key software for tensor computations, including Mathematica for symbolic and numerical manipulations, TensorFlow and PyTorch for deep learning, and NumPy and SymPy for efficient numerical and symbolic operations. Each tool's features, applications, and practical examples are discussed, emphasizing their transformative role in modern computation. By leveraging these tools, researchers can tackle complex tensor algebra, data analysis, and optimization challenges effectively, making these skills vital in today's computational landscape.

"A language that doesn't affect the way you think about programming, is not worth knowing."
— Mokokoma Mokhonoana

1 Introduction

Tensors are fundamental mathematical objects that play a critical role in fields ranging from theoretical physics to machine learning and engineering. As generalizations of scalars, vectors, and matrices, tensors enable the representation of multi-dimensional data and complex relationships between different quantities making them indispensable in fields like machine learning, and computer vision. In the modern computational landscape, performing tensor operations is central to tasks such as modeling physical systems, optimizing algorithms, and processing data. The advent of powerful software libraries has made working with tensors more accessible and efficient, whether for symbolic computation, machine learning, or numerical analysis.

Tensors come in different types, such as contravariant, covariant, and mixed tensors, and can be represented in a variety of coordinate systems. The ability to perform tensor operations, such as addition, multiplication, contraction, and transformation, is crucial in many scientific computations. The complexity of tensor operations makes them challenging to handle manually, especially when dealing with large datasets or high-dimensional problems.

With the rise of computational mathematics and data science, many specialized software libraries have emerged to simplify tensor manipulation. These tools not only enable more efficient computation but also make complex tensor calculus and algebraic operations more accessible. This brief article explores a few popular software tools for tensor operations, providing insight into their capabilities, uses, and practical applications.

2 Popular Software for Tensor Operations

In recent years, several software tools and libraries have gained prominence for their ability to perform tensor computations efficiently. These include general-purpose mathematical libraries, specialized deep learning frameworks, and symbolic computation tools. Below, we explore some of the most widely used software for tensor operations.

2.1 Mathematica: Symbolic and Numerical Tensor Manipulation

Mathematica is a computational software system that excels in both symbolic and numerical tensor manipulations. It is widely used in academic research, especially for solving complex problems in physics, engineering, and mathematics.

Key Features:

- **Symbolic and Numeric Tensors**: Mathematica provides tools for both symbolic tensor manipulation (e.g., in general relativity) and numeric tensor operations (e.g., in machine learning).
- **Tensor Operations**: It supports a variety of tensor operations, including contraction, scalar products, covariant differentiation, and tensor decomposition.
- **Visualization**: Mathematica includes powerful visualization tools to graphically represent multi-dimensional tensor data and geometric objects.
- **Symbolic Computation**: Mathematica is ideal

for tasks like deriving tensor equations, performing symbolic differentiation, and computing tensor fields in curved spaces.

1. Simple Example:

```
(* Define a symbolic tensor of the second
rank in three dimensions in array form. *)

T = Array[a, {3, 3}];

(* Express it in matrix form. *)

MatrixForm[T]

(*Find the trace of the tensor.*)

Tr[T]

This will give the result;

(*Output for Tr[T]*)

a[1, 1] + a[2, 2] + a[3, 3]

(* Output for MatrixForm[T] *)

MatrixForm
[{{a[1, 1], a[1, 2], a[1, 3]},
 {a[2, 1], a[2, 2], a[2, 3]},
 {a[3, 1], a[3, 2], a[3, 3]}}]

(* Output for Tr[T] *)

a[1, 1] + a[2, 2] + a[3, 3]
```

2. Example in Physics: Calculating a Ricci Tensor

```
(* Define a metric tensor *)

g = {{1, 0}, {0, -1}};

(* Compute the Christoffel symbols *)

christoffel = ChristoffelSymbols[g];

(* Calculate the Ricci tensor *)

ricci = RicciTensor[christoffel];

(* Output the result *)

(* For the given metric g=diag(1,-1), which
is constant (no dependence on coordinates),
all Christoffel symbols are zero because the
metric tensor does not vary with position.*)

{{{0, 0}, {0, 0}},
 {{0, 0}, {0, 0}}}

Since the metric is constant and does not
depend on coordinates, the Ricci tensor
will be zero for this flat space.

{{0, 0},
 {0, 0}}

This example showcases how Mathematica
can handle symbolic tensor computations
relevant to general relativity.
```

2.2 TensorFlow: Deep Learning and Beyond

TensorFlow is a widely used open-source machine learning library developed by Google. While its primary focus is on training and deploying deep learning models, its core structure is based on tensor computations, making it a powerful tool for general tensor manipulation.

Key Features:

- **Tensor Representation**: Tensors in TensorFlow are the fundamental data structure. They can represent arrays of arbitrary rank and are used throughout the library for computations.
- **Operations**: TensorFlow supports a wide range of tensor operations, including addition, multiplication, reshaping, element-wise operations, and tensor contractions. It also supports broadcasting and higher-order tensor operations.
- **GPU Acceleration**: TensorFlow's native support for GPU acceleration enables the efficient computation of large-scale tensor operations, making it ideal for deep learning and other resource-intensive tasks.
- **Automatic Differentiation**: TensorFlow includes an automatic differentiation engine, which is essential for optimization and training machine learning models using gradient-based methods.

Example:

```
import tensorflow as tf

# Create tensors
A = tf.constant([[1, 2], [3, 4]])
B = tf.constant([[5, 6], [7, 8]])

# Perform tensor operation
C = tf.add(A, B)

# Output result
```

```
print(C)
```

2.3 PyTorch: A Flexible Framework for Tensors

PyTorch, developed by Facebook, is another open-source machine learning library that has become popular due to its dynamic computation graph and ease of use. PyTorch is particularly valued for its flexibility, making it an excellent choice for both academic research and production environments.

Key Features:

- **Tensor Representation**: In PyTorch, tensors are multi-dimensional arrays similar to NumPy arrays but with additional capabilities like support for GPU acceleration and automatic differentiation.
- **Operations**: PyTorch provides a vast array of tensor operations such as matrix multiplication, element-wise operations, tensor slicing, and reshaping. It also supports broadcasting, which allows for operations on tensors of different shapes.
- **Autograd**: PyTorch includes a powerful automatic differentiation library called Autograd, which simplifies the process of computing gradients for optimization problems.
- **GPU Support**: PyTorch seamlessly integrates with CUDA to enable GPU-based tensor computation, making it highly efficient for large-scale computations.

Example:

```
import torch

# Create tensors
A = torch.tensor([[1.0, 2.0], [3.0, 4.0]])
B = torch.tensor([[5.0, 6.0], [7.0, 8.0]])

# Perform tensor operation
C = torch.matmul(A, B)

# Output result
print(C)
```

2.4 NumPy: A Foundation for Numerical Computations

NumPy is one of the most widely used libraries for numerical computations in Python. It provides support for multi-dimensional arrays (which can be viewed as tensors) and offers a range of mathematical functions to operate on them.

Key Features:

- **Array Representation**: NumPy arrays are essentially multi-dimensional tensors. These arrays can represent scalars, vectors, matrices, and higher-dimensional arrays.
- **Operations**: NumPy supports tensor operations such as element-wise addition, matrix multiplication, tensor reshaping, slicing, and transposition.
- **Efficiency**: NumPy is highly optimized for performance and is often used for smaller-scale tensor manipulations in scientific computing.
- **Integration**: Many other scientific Python libraries, such as SciPy, Matplotlib, and Pandas, build on top of NumPy for more advanced functionalities.

Example:

```
import numpy as np

# Create tensors
A = np.array([[1, 2], [3, 4]])
B = np.array([[5, 6], [7, 8]])

# Perform tensor operation
C = np.matmul(A, B)

# Output result
print(C)
```

2.5 SymPy: Symbolic Computation for Tensor Algebra

SymPy is a Python library for symbolic mathematics, offering powerful tools for symbolic tensor algebra. Unlike TensorFlow or PyTorch, which focus on numerical tensor computations, SymPy is designed for symbolic manipulation, making it an ideal tool for tasks like deriving tensor equations, computing Ricci tensors, and performing tensor transformations in physics.

Key Features:

- **Symbolic Tensor Representation**: SymPy allows for the symbolic manipulation of tensors, including operations like contraction, covariant and contravariant transformations, and calculating the Christoffel symbols.
- **Tensor Operations**: It supports basic tensor operations such as addition, multiplication, and contraction, as well as more advanced operations like covariant differentiation.
- **Mathematical Derivations**: SymPy is often

used in theoretical research, particularly in fields like general relativity, where symbolic tensor operations are required.

- **LaTeX Integration**: SymPy can output tensor expressions in LaTeX format for publication-quality documents.

Example:

```
from sympy import symbols
from sympy.tensor.tensor import TensorHead, Idx

# Define symbolic tensors
T = TensorHead('T', 2)
i, j = symbols('i j')

# Create a symbolic tensor expression
expr = T(i, j) + T(j, i)

# Output result
print(expr)
```

3 End Note: The Power of Tensor Software

The rise of powerful software libraries for tensor computation has revolutionized many fields by simplifying complex operations. **Mathematica**, with its combination of symbolic and numeric capabilities, remains a go-to tool for advanced mathematical research. Tools like **TensorFlow** and **PyTorch** have made tensor operations integral to machine learning and artificial intelligence, while libraries such as **NumPy** and **SymPy** provide versatile tools for scientific and symbolic computations.

By leveraging these computational tools, researchers and engineers can tackle the challenges of multi-dimensional data manipulation, complex tensor algebra, and optimization problems more effectively and efficiently. Whether you are working with large datasets, conducting theoretical research, or developing machine learning models, understanding and utilizing these software tools for tensor operations is a key skill in the modern computational landscape.

References

[1] https://en.wikipedia.org/wiki/Tensor_software

[2] https://www.tensorflow.org/

[3] https://numpy.org/

[4] https://pytorch.org/

[5] https://www.sympy.org/en/index.html

Remembering Professor Israr Ahmad: Physicist and Educator

Zafar Ali Khan
Department of Physics, Aligarh Muslim University, Aligarh, UP, India-202002

Abstract

This article is dedicated to bringing the legacy of Prof. Israr Ahmad to the present generation. Despite the challenges he faced, he made remarkable contributions to the field of physics in general and nuclear physics in particular. His life and work show us how dedication, passion, and perseverance can create lasting changes, even when circumstances are tough. Prof. Israr Ahmad was a distinguished theoretical nuclear physicist whose impact on the field of quantum scattering theory and nuclear reaction dynamics continues to resonate. He served at the physics department, Aligarh Muslim University (AMU) for decades, becoming one of the key figures in advancing nuclear physics research in India.

Prof. Israr Ahmad
(December 19, 1940 – April 02, 2010)

Professor Israr Ahmad was born in Mahuwara Kalan, Azamgarh, Uttar Pradesh. Prof. Ahmad's brilliance was evident quite early. After completing his initial education, he attended Pushp Nagar Inter College in Azamgarh district of Uttar Pradesh, for high school. In 1959, he earned his graduation (B.Sc.) from Shibli National College, Azamgarh, U.P., securing first position. He was awarded the Gold Medal by Gorakhpur University in 1959 for securing the top position in the B.Sc. examination. He then moved to Aligarh, where he obtained an M.Sc. in Physics in 1961, earning the F.D. Murad Medal for topping the M.Sc. examination. Soon after, he was appointed as a Lecturer in Physics in the same year, and began his Ph.D. work under Prof. Mohd. Zillur Rahman Khan. Prof. Ahmad joined AMU as a Lecturer in Physics in 1961, even before completing his Ph.D. He submitted his doctoral thesis in 1969 as a teacher candidate. Prof. Ahmad was promoted to Reader on May 20, 1971. Over the years, he rose through the academic ranks, becoming a Professor in 1984 and serving as Chairman of the Department of Physics from 1988 to 1991.

Throughout his career, Prof. Ahmad's research focused on theoretical nuclear physics, particularly nuclear reactions using the Optical and Glauber Models. Prof. Ahmad's pioneering work on the Coulomb-modified Glauber model provided a robust framework for analysing reaction cross-sections and angular distributions in nuclear collisions. His research on hadron-nucleus and nucleus-nucleus elastic and inelastic scattering at intermediate energies offered valuable insights into the behaviour of nuclear matter distribution and the importance of considering the Coulomb interaction in nuclear reactions. His original work on the dispersion relation for the optical-model potential, which revealed surface-peaking in the low-energy imaginary potential, earned him global recognition. He was also the first to introduce the concept of α-clustering in light nuclei, which became a key element in the study of elastic and inelastic proton-nucleus and nucleus-nucleus collisions at intermediate energies.

He authored numerous papers in prestigious international journals.

Prof. Ahmad's revolutionary idea on clustering was first developed during his visit (1971) to the International Centre for Theoretical Physics (ICTP), Trieste, Italy, where he collaborated with luminaries such as Nobel Laureate Prof. Abdus Salam, Prof. Georges Ripka (Saclay, France), Prof. L. Fonda (ICTP), Prof. L. Bertocchi (ICTP), and Prof. G. J. Igo (UCLA, USA). His exceptional grasp of physics earned him global recognition, leading to invitations to collaborate at prestigious institutions like ICTP, Saclay, and UCLA. These visits proved highly productive, contributing to the publication of groundbreaking research in leading scientific journals. During the Saclay visit (1974), Prof. Ahmad studied the elastic and inelastic scattering of 1.0 GeV protons on a large number of target nuclei (Z=6 to Z=82) within the framework of Glauber theory, in which he has involved for the first time the collective excitations to one-phonon levels using the Tassie model under the adiabatic approximation, and the effects of both the couplimg between the elastic and inelastic channels and the two-body correlation in the intrinsic state are considered. The results of such a study attracted global attention and its importance can be assessed from a large number of its citations in the field of nuclear reactions at intermediate energies. Prof. Ahmad's another visit to Saclay in 1979 has added a new dimension in the field of nuclear reactions in the form of proposing a different approach, known as effective profile function approach, for the correlation expansion of the hadron-nucleus amplitude in Glauber theory; effects of both the c.m. and Pauli pair correlations on the elastic scattering differential cross sections are studied, and it has been shown that these correlations are important enough to be included in any detailed analysis of the elastic scattering data. The effective profile function approach has been further extended and widely used by his group and other collaborators to include the analysis of nucleus-nucleus scattering data on elastic angular distribution, and reaction and charge-changing cross sections; the results on nucleus-nucleus collisions have provided valuable information about the proton and neutron radii and their distributions. His academic relations with eminent scientists, Prof. Abdus Salam, Prof. Georges Ripka, Prof. G. J. Igo, also brought them to Aligarh, fostering an environment of intellectual exchange. Apart from collaborating with colleagues in his department, he also worked with leading scientists across India. This included prominent figures such as Prof. P. C. Sood, Prof. Y. R. Waghmare, Prof. Bikash Sinha, Prof. S. K. Khadkikar, Prof. B. M. Udgaonkar, Prof. Y. K. Gambhir, Prof. B. K. Jain, Prof. N. K. Ganguli, Prof. D. K. Srivastava etc. Through his strong connections with scientists at the Bhabha Atomic Research Centre (BARC) and top Indian universities, he helped organize the annual Department of Atomic Energy (DAE) Symposium on Nuclear Physics during December 26-31, 1989 at the AMU, Aligarh. The symposium was an important event that advanced research and encouraged collaboration. I still remember that renowned scientists like Dr. B. K. Jain, who was the convener, and Dr. S. S. Kapoor, who was the chairman of the conference, along with Dr. V. M. Datar, also participated in the symposium, making it even more special.

Prof. Ahmad's dedication to teaching and mentoring shaped the careers of a large number of physicists. He supervised several M.Phil. and Ph.D. students, nurturing a new generation of scholars. On a personal note, In 1971, I joined his lab as a Ph.D. student and had the privilege of working alongside Dr. Farhan Mujib, Prof. Wasi Haider, and Dr. A. N. Saharia, who greatly influenced my research career. My classmate, Dr. Nikhat Bano, also joined the group that year. Later, scholars like Dr. M. A. Alvi, Mr. Sultan Ahmad, Dr. M. A. Suhail, and Prof. A. A. Usmani, now the Chairman of the Department of Physics, AMU, joined his research team. I still remember discussions of Prof. Israr Ahmad, about AMU's global scientific reputation. While some doubted its prominence, Prof. Ahmad's pioneering contributions in theoretical nuclear physics had already placed AMU on the global map.

Prof. Ahmad was deeply committed to modernizing education, not only through teaching and research but also by making significant contributions to educational reform. Prof. Ahmad was also keen on spreading the message of the Islamic reformer Sir Syed Ahmad Khan. A strong supporter of the Aligarh Movement, he revived Sir Syed's mission to promote modern education, especially science, among oriental students and seminaries. One of his key initiatives was the establishment of the Centre for Promotion of Science (CPS) at AMU in 1985. The goal of CPS was to bridge the gap between traditional and modern scientific education, particularly for madrasa students. With support from Prof. Abdus Salam, the CPS became a vibrant hub for educational advancement, fostering a new generation of students in the sciences. Under his leadership, the centre played a crucial role in integrating madrasas with modern education, significantly contributing to societal progress. Prof. Abdus Salam's visit to the CPS in 1989 further underscored the importance of this initiative.

The center played an important part in connecting religious seminaries with modern educational insti-

tutions, organizing refresher courses, seminars, and lectures for madrasa students and teachers. Prof. Ahmad organized a series of conferences on 'Religious Seminaries and Science Education' and conducted introductory science courses for the teachers of Muslim religious seminaries. He established an independent office for CPS next to the Department of Physics and the Faculty of Science Dean's office and served as its director until 1991.

In addition to his educational initiatives, Prof. Ahmad was dedicated to promoting intellectual and scientific discourse. He served as the Editor of Tahzibul Akhlaq from 1986 to 1990, where he revitalized the magazine's legacy and furthered the vision of Sir Syed Ahmad Khan, particularly in advancing modern education among students from religious seminaries. Prof. Ahmad's commitment to global scientific collaboration was reflected in his memberships with several prestigious organizations. He was an associate member of the International Centre for Theoretical Physics (ICTP) from 1982 to 1993. He was also a member of the New York Academy of Sciences, the Indian Physics Association (IPA), and the Indian Association of Physics Teachers (IAPT).

Prof. Israr Ahmad's life and work serve as a profound testament to the power of knowledge, curiosity, and education. His remarkable achievements as a physicist, educator, and mentor continue to inspire and influence countless individuals. Beyond his scientific contributions, his creative works and thought-provoking articles in Urdu, Hindi, and English reflected his versatility and intellectual depth. Prof. Ahmad's legacy as a visionary will undoubtedly guide future generations, leaving an enduring impact on both the scientific community and society at large. His guidance shaped many careers, including my own, and his influence will continue to resonate for years to come.

The Visionary Legacy of Prof. Harnam Singh Hans in Accelerator-Based Nuclear Physics

B. P. Singh
Department of Physics, Aligarh Muslim University, Aligarh, UP, India-202002

Abstract

The Physics Department at Aligarh Muslim University (AMU), Aligarh, has a legacy that spans over a century, distinguished by groundbreaking contributions to various fields, especially nuclear physics. The department, founded in 1908, emerged as a beacon of excellence in teaching and research. The journey that began under Prof. H. B. Duncliff's leadership in the early 20^{th} century, with Dr. Wali Mohammad as the first head, has continued through the years. Several influential figures, contributed immensely to both experimental and theoretical nuclear physics. This article explores the remarkable history of the Physics Department at AMU, the pioneering contributions of its faculty, and its legacy in the field of nuclear physics, which continues to resonate today. Some of the references consulted for this write-up are provided at the end. Additionally, I have sought insights from several senior professors, both from this department and other universities, to enrich the historical narrative of the Physics Department at AMU. Special acknowledgment goes to Prof. H. S. Hans's son, now an accomplished industrialist, whose valuable input added depth to the discussion on Prof. Hans's contributions.

1 Establishment of the Physics Department

AMU's Physics Department traces its roots to 1908 when it was first established as a combined Department of Physics and Chemistry. Dr. Wali Mohammad, a former student of the legendary Sir J. J. Thomson, joined as an Assistant Professor. His contribution, along with Prof. Duncliff, laid the groundwork for an excellent academic and research environment. By 1912, the Physics Department became an independent entity. In the year 1926, AMU awarded its first Ph.D. in Physics, that marked the start of a tradition of pioneering research along with teaching.

Throughout the early 20th century, the department attracted distinguished scientists, including Profs. Rudolf Samuel, Rafi Mohammad Choudhary, P. S. Gill, R. K. Asundi, and P. Venkateshwarlu, among others. These scientists laid the foundation for the department's strength in both teaching and research. By the 1930s, the department had established a spectroscopy lab, and by the 1960s, the first steps towards nuclear physics research were taken with the creation of a Cockcroft-Walton neutron generator.

2 The Pioneering Efforts of Prof. Piara Singh Gill

One of the most significant turning points in AMU's nuclear physics research came in 1949 with the appointment of Prof. Piara Singh Gill as the Head of the Physics Department. Prof. Gill, was a distinguished physicist trained under Nobel laureate Prof. Arthur Holly Compton. He was instrumental in establishing the foundation for nuclear and cosmic ray research at AMU Aligarh. His close association with AMU's Vice-Chancellor Dr. Zakir Hussain and the government of India's scientific advisory board led to the inclusion of nuclear physics in the department's academic pursuits. The leadership of Prof. Gill saw the initiation of various experimental nuclear physics projects. These projects included the study of neutron reactions and the exploration of cosmic rays. His vision and leadership in the early stages of nuclear research at AMU were instrumental in setting up a legacy that would be built upon by future generations.

3 Prof. H. S. Hans and Accelerator-Based Nuclear Physics Research

Prof. Harnam Singh Hans, often referred to as the "Father of Accelerator-Based Nuclear Physics in Indian Universities," played an instrumental role in transforming AMU into a center for experimental nuclear physics. Born in 1922, Prof. Hans completed his graduate studies at Banaras Hindu University (BHU) and joined AMU as a Ph.D. student under Prof. Gill in 1950.

Prof. Harnam Singh Hans

His doctoral work focused on the experimental study of neutron scattering using a 1 MV accelerator. This laid the groundwork for AMU's future in accelerator-based research. During his doctoral research, he conducted experiments on the elastic and inelastic scattering of 3.7 MeV neutrons at Swarthmore, Pennsylvania, United States, using a 1 MV accelerator. In 1958, he was appointed as a Reader at the Physics Department, AMU Aligarh a position he held until 1962. During 1962-1963 he served as an Assistant Professor at Texas A&M University, USA. Prof. Hans was known for his deep passion for accelerator-based nuclear physics research.

In 1958, coming back to AMU Aligarh he began planning to construct of a Cockcroft-Walton accelerator—a type of particle accelerator used to produce neutrons. With the assistance of Dr. D. C. Sarkar and Dr. C. S. Khurana, Prof. Hans led the team that successfully built and installed the first Cockcroft-Walton neutron generator at AMU in 1958. This accelerator was first of its kind in an Indian university.

The construction of the Cockcroft-Walton generator was a great achievement for the Physics Department, AMU Aligarh. It facilitated studies in nuclear reactions and nuclear spectroscopy, marking the department as a center of experimental nuclear science. The accelerator enabled research on neutron induced reactions, including those producing fast neutrons with energies up to 14 MeV. This was important in the study of nuclear reaction mechanisms and applications in nuclear energy development.

4 Building the Legacy and the Role of Prof. Hans in Advancing Nuclear Research

The tenure of Prof. Hans at AMU transformed the department into a hub for experimental nuclear physics. His team's efforts included the development of equipment such as gas flow proportional counters, Geiger Muller counters etc. These all were constructed in the glass-blowing lab of the physics department. The construction of experimental apparatus, in-house, reflected the commitment of prof. Hans, to advancing the field of experimental nuclear physics with limited resources.

One of the enduring contributions of Prof. Hans was his mentorship. His philosophy of "sleeping with the problem," meaning a relentless pursuit of solutions through deep thinking, influenced countless students and researchers. His guidance in nuclear research made a profound impact on AMU. This led to a large number of publications, in reputed journals, on neutron-based reactions and several Ph.D. theses between 1958 and 1986. Prof. R. Prasad, former Physics Department Chairman now in Australia, praise Prof. Hans for his spirit and dedication to research. He highlighted Prof. Hans's fearless approach to exploring new and unknown fields. He noted that, although his own work focused on measuring meson half-life, he initiated the setting up of a Cockcroft-Walton type accelerator at the Physics Department, Aligarh. Prof. Hans also initiated experimental studies of neutron reactions and measured the energy spectrum of protons emitted in (n,p) reactions. For these studies the proportional counters were built in the department glass blowing lab.

Prof. Prasad further shared a personal insight into Prof. Hans's problem-solving approach: "I personally experienced that this is a very correct approach. I remember that the electronic circuits I developed for the measurement of short half-life radioactive nuclei were an outcome of this approach of 'sleeping with the problem'." This method, inspired by Prof. Hans, emphasized persistence and deep contemplation, contributing significantly to Prof. Prasad's own work in nuclear physics. Prof. R. Prasad also appreciated the advocacy of Prof Hans, for publishing research papers in Indian journals. This underscored his commitment to strengthening Indian scientific community. Prof. Hans supervised the construction of a Cockcroft-Walton neutron generator, which became the focus of a Ph.D. thesis in 1960, submitted by Dr. C. S. Khurana. They both jointly published their work in Pramana – Journal of Physics, contributing valuable research to India's

academic literature.

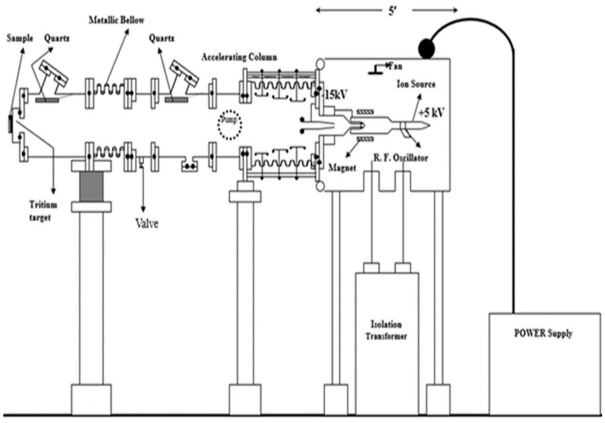

A typical layout of the Cockcroft-Walton Neutron Generator at the Physics Department, AMU, Aligarh

Research using the Cockcroft-Walton Neutron Generator at AMU was dedicated to exploring fast neutron reactions. For these studies, a strong, monoenergetic neutron source was crucial, one that would be free from unwanted radiation such as slow neutrons and gamma rays. The low-energy Cockcroft-Walton accelerator was ideal for producing neutrons through reactions like $D(d,n)^3He$ and $T(d,n)^4He$, which yield neutrons of approximately 2.8 MeV and 14 MeV, respectively. The $T(d,n)^4He$ reaction, with a resonance around 100 keV, was particularly advantageous for generating 14 MeV neutrons in low-energy accelerators.

In experiments, a deuteron beam from the Cockcroft-Walton Accelerator was directed at a thin tritium target to produce fast neutrons via the $T(d,n)^4He$ reaction:

$^3H +^2 D \rightarrow^4 He +^1 n + 17.59MeV$

The neutron, being the lighter reaction product, carried most of the available energy. For deuteron energies around 130 kV, neutrons of about 14.8 MeV were emitted in the forward zero-degree direction relative to the deuteron beam. Activated samples were analysed with either a beta counter or a gamma-ray spectrometer, depending on the type of emitted radiation. A beta counter with a $2.5mg/cm^2$ end window was used when residual nuclei decayed through beta emission, while a NaI(Tl) gamma-ray detector with a 0.08 cm aluminum wall was employed for gamma detection.

After Prof. H. S. Hans left AMU, Prof. Rajeshwari Prasad took on the responsibility of continuing neutron generator experiments. He also not only continued its operation but also looked after its maintenance. In 1963, when the Physics Department relocated to a new building, Prof. Prasad managed the challenging task of moving the accelerator. His leadership ensured that the machine was successfully relocated within a short time. This allowed neutron-based research to continue seamlessly in the present new building for accelerator lab.

In 1964, the reputation of Prof. Hans, as a leading nuclear physicist led him to a pivotal meeting with Prof. S. P. Pandya at the Argonne National Laboratory. There, he was encouraged to pursue the acquisition of a variable-energy cyclotron for India. However, in 1965, Prof. Hans moved to Kurukshetra University, and later to Panjab University, Chandigarh, in 1967, where he continued his pioneering work in nuclear physics.

5 The Cyclotron at Panjab University: Historical Significance and Origin

Presently, the cyclotron housed at the Physics department, Panjab University, Chandigarh, is much more than an old particle accelerator. It is a testament to scientific perseverance, the foresight of nuclear physicist Prof. Harnam Hans, and the commitment of a dedicated team of engineers and technicians. As one of the world's oldest operational particle accelerators. It has been functioning continuously for over more than 50 years. This is a remarkable feat that highlights the importance of Prof. Hans's efforts to establish nuclear research in India, especially in a regional state university.

Let me go back in history. The present cyclotron at the Panjab University was originally built in the 1930s at the University of Rochester, USA. This type of particle accelerator was invented by Ernest O. Lawrence at the University of California, Berkeley in 1929–1930. The cyclotron is designed to accelerate charged particles by applying an alternating electric field while the particles move along a circular path in a magnetic field. Cyclotrons are smaller in scale compared to facilities like Large Hadron Collider at CERN, Geneva. It is crucial in experimental nuclear physics research. The invention of cyclotron was so significant that Ernest O. Lawrence was awarded the Nobel Prize in Physics in 1939.

By the 1960s, particle physics was advancing, and newer, larger accelerators replaced the older ones, pushing the original Rochester cyclotron into obsolescence. Prof. Hans, a young physicist with a vision to bring nuclear physics research to India, learned of

the cyclotron's availability. He discussed with many physicists in India and and organized its shipment to India in 1967. Initially intended for Kurukshetra University, it was redirected to Panjab University when Prof. Hans was appointed to its Department of Physics. His initiative was very much ambitious and unconventional. It may be mentioned that it was neither a government project nor any officially supported US initiative. However, it was rather a personal and determined pursuit to provide India with valuable scientific infrastructure.

6 The Challenge of Rebuilding the Cyclotron in India

Once the cyclotron machine components arrived in Chandigarh, Prof. Hans and his team faced the difficult challenge of reassembling and operating a complex machine that had been disassembled. This task was made even more difficult as most technicians had never seen a functional cyclotron before it arrived there. Despite these hurdles and the limited resources available, the team under the leadership of Prof Hans, succeeded in reconstructing the cyclotron. Their achievement underscores the vision of a teacher like Prof Hans to cultivate a research culture. It was his commitment to establish a center for experimental nuclear physics in northern India. The cyclotron has worked for decades thanks to dedicated technicians, researchers, and students. They maintained it with relentless effort. Their story shows dedication to science. They overcame logistical, technical, and financial challenges to preserve this historic machine.

7 The Role and Contributions of Prof. Harnam Hans

Prof. Hans's decision to bring the cyclotron to India and place it in an academic institution instead of a government facility was a visionary move. When nuclear research in India was mostly done in government institutions like the DAE, Prof. Hans thought universities should also lead scientific research. His vision expanded research opportunities in northern India. It gave young students a chance to work with advanced nuclear physics equipment. This helped bring advance nuclear science research closer to the universities.

8 The Enduring Legacy of Prof. Hans

Prof. Hans's contributions extended beyond mere coordination. As already mentioned, he was instrumental in promoting nuclear research at Panjab University, turning the cyclotron into a tool for basic nuclear research, and student training. Even the students from the Physics Department, AMU Aligarh regularly visited to the Panjab University, Chandigarh for carrying out research using the proton beam from this cyclotron. Under the leadership of Prof. Hans, the cyclotron enabled the publication of numerous research papers. In particular many experiments on Coulomb excitation were performed to study nuclear structures through electromagnetic interactions.

Today, the cyclotron is no longer at the frontier of nuclear research but remains an important asset for academic and training purposes. Presently, it is being used for (i) Material Analysis through techniques such as Proton Induced X-ray Emission Spectroscopy (PIXE) and Proton Induced Gamma-ray Emission (PIGE), the cyclotron is used to analyse materials and identify elements within samples; (ii) Training of Postgraduate Students with cyclotron and is a valuable tool for hands-on training, to students (iii) Educational Outreach where the facility also offers science demonstrations for young students. These activities highlight the cyclotron's adaptability and continued relevance, reflecting the broader vision Prof. Hans had for a research culture accessible to students and researchers.

Prof. Hans's impact on nuclear physics in India is immeasurable. His efforts at AMU and Panjab University set the stage for numerous advancements in experimental nuclear physics and helped establish India's presence in the global scientific community. His work on the Cockcroft-Walton accelerator and the cyclotron laid the foundation for future generations of researchers in the field. As a visionary scientist and dedicated teacher, Prof. Hans was instrumental in transforming AMU into a leading center for nuclear research. His legacy continues to inspire and shape the future of nuclear physics in India.

9 Film Documentation and Recognition of the Cyclotron's Legacy

Science historian Dr. Jahnavi Phalkey, director of Science Gallery Bengaluru, explored the Chandigarh cyclotron's story in her doctoral research. Later she created a documentary titled "Cyclotron". The film, which highlights the history of this machine and the efforts of the people who kept it operational, serves as a tribute to Prof. Hans and his team's enduring impact on Indian nuclear research. According to Dr. Phalkey, the story of the cyclotron exempli-

fies the audacity of a young physicist who wanted to bring experimental nuclear physics to an Indian university. The film brings this story to a broader audience, ensuring that Prof. Hans's contributions to Indian science are not forgotten.

Dr. Phalkey's research into the cyclotron also draws attention to the challenges faced by Indian universities in maintaining research facilities and conducting world-class science. According to her, institutions across India are often under-resourced, which affects their ability to foster a thriving research culture. The cyclotron's story reveals both the potential of academic institutions to support groundbreaking research and the constraints that limit their reach. To elevate Indian research to global standards, it is crucial to invest in academic research facilities and foster collaborations between universities and national research bodies.

The cyclotron at Panjab University is a powerful symbol of the visionary leadership and dedication of Prof. Harnam Singh. His work in building research infrastructure and promoting nuclear physics, first at Aligarh Muslim University and later at Panjab University, has inspired generations of students and researchers. This has left a lasting impact on the scientific community in India. The continued operation of the cyclotron, thanks to the dedication of its caretakers, serves as a reminder of the importance of passion in science. Profs. Hans and Prof Gill's legacy lives on through the students who train on these machines. Researchers continue to use them for important research work. The broader community benefits from their scientific and educational value. Their contributions will shape Indian science for years to come.

References

[1] The Hindu; Online edition of India's National Newspaper; Thursday, Feb 27, 2003.(https://web.archive.org/web/20110402113201/http://www.hinduonnet.com/thehindu/seta/2003/02/27/stories/2003022700170300.htm)

[2] "150 kV Cockroft-Walton Type Particle Accelerator", C. S. Khurana and H. S. Hans, Indian Journal of Physics, 10, 468, (1958).

[3] Construction of 150 kV Cockroft-Walton Particle Accelerator and Study of Fast Neutron Reactions" Ph.D. thesis; C. S. Khurana, A.M.U., Aligarh, (1960).

[4] Prof. H. S. Hans: https://hshans.com/index.php

[5] Video on Cyclotron by Jahnavi Phalkey and Shiraz Minwalla: https://youtu.be/7peBN_WiZwk

[6] Inter University Accelerator Centre (IUAC), New Delhi, India: https://iuac.res.in/

[7] "Decennium Report", Department of Physics, A.M.U., Aligarh, (2022).

[8] "S.S. Bhatnagar, C.V. Raman, Homi Bhabha and Research in Physics at Lahore and Chandigarh" presentation by Arun Kumar Grover, Department of Physics, Panjab University, Chandigarh 160014; IPA D.A.E.–C V Raman Lecture, 2013-14 at P.U. Campus, Chandigarh, August 7, 2013.

Superannuated Faculty Roll of Honour (1912–2024)

Department of Physics, Aligarh Muslim University, Aligarh, UP, India-202002

The storied halls of the Department of Physics at Aligarh Muslim University, Aligarh, stand as a testament to over a century of academic excellence, having been established in 1912 after separating from the combined Department of Physics and Chemistry, which had been founded in 1908. Over the decades, this department has been graced by the presence of over hundred distinguished educators who have enriched its legacy before embarking on their well-earned retirement or joining other institutions.

In an earnest effort to preserve a definitive record of those who have shaped the intellectual contours of this institution, we have prepared a curated chronicle of our esteemed faculty, marked by their dates of joining and culmination of service, whether through departure or superannuation. Fortunately, this task was significantly aided by prior efforts made during the centenary celebrations of the Faculty of Science. The data for this roll was drawn from the compendium titled *"100 Years of the Faculty of Science, Aligarh Muslim University (1920–2020)"*, published in 2020 to commemorate the Faculty's centenary. The team that undertook this herculean task comprised Prof. Qazi Mazhar Ali, Ex-Dean, Faculty of Science, as the Chief Editor and Prof. Sajjad Athar, Ex-Chairman, Department of Physics, as the Joint Editor.

We extend our heartfelt gratitude to this team for their meticulous efforts in compiling this invaluable resource, which ensures the preservation of the Department's rich history for future generations. We also thank Prof. B. P. Singh, Ex-Chairman, Department of Physics, AMU, for his active interest and support in the preparation of this article.

We sincerely regret any missing tenure details or inadvertent omissions in this record, despite our best efforts to ensure accuracy. To further commemorate this illustrious heritage, this record is being published in the Physics Bulletin-2025 to ensure it reaches a wider audience.

Presented below is a comprehensive roll of honour of 103 members, enumerating these luminaries alongside their dates of affiliation and retirement - a lasting tribute to their enduring contributions to the tapestry of knowledge and mentorship woven within these hallowed walls:

(Note: WC refers to Women's College, NA-means Not Applicable)

S. No.	Name	Tenure	Headship	Deanship
1	Prof. Choudhary Wali Mohammad	(1908-1922)	(1912-1922)	NA
2	Prof. F. D. Murad	(19xx -19xx)	(1922-1930)	NA
3	Prof. Rudolf Samuel	(1930-1938)	(1930-1936)	NA
4	Prof. Mohammad Ishaque	(19xx -19xx)	(1936-1938)	NA
5	Prof. Rango Krishna Asundi	(1931-1938)	NA	NA
6	Prof. Rafi Mohammad Chaudhary	(1938-1948)	(1938-1948)	NA
7	Dr. S. Nawazish Ali	(19xx -19xx)	(1948-1949)	NA
8	Prof. Piara Singh Gill	(1949-1963)	(1949-1963)	(1950-1953) (1955-1957)
9	Mr. Ehsanul Haq	(19xx -19xx)	NA	NA
10	Mr. S. A. Jalil	(19xx -19xx)	NA	NA
11	Dr. D. N. Mallik	(19xx -19xx)	NA	NA
12	Mr. K.A. Murad	(19xx -19xx)	NA	NA
13	Dr. S. Mujtaba Karim	(19xx -19xx)	NA	NA
14	Mr. Sibghatullah Khan	(19xx -19xx)	NA	NA

15	Mr. Ziauddin	(19xx -19xx)	NA	NA
16	Dr. Janak Devi Dheer	(19xx -19xx)	NA	NA
17	Dr. Ashfaq Ali Khan	(19xx -19xx)	NA	NA
18	Dr. Ms. Nasreen Ateqad (WC)	(19xx -19xx)	NA	NA
19	Dr. Mahendra Kumar Sharma	(19xx -19xx)	NA	NA
20	Dr. K. Rama Reddy	(19xx -19xx)	NA	NA
21	Mr. D. S. Parmar	(19xx -19xx)	NA	NA
22	Dr. M. Zubair Ahsan	(19xx -19xx)	NA	NA
23	Dr. P. L. Kapoor	(19xx -19xx)	NA	NA
24	Dr. Y.P. Kulshreshta	(19xx -19xx)	NA	NA
25	Mr. M. P. Singh	(19xx -19xx)	NA	NA
26	Dr. Charanjit Singh	(19xx -19xx)	NA	NA
27	Prof. G. S. Sanyal	(19xx -19xx)	NA	NA
28	Dr. M. Y. Ansari	(19xx -19xx)	NA	NA
29	Mr. A. A. Khan	(19xx -19xx)	NA	NA
30	Dr. S.F. Mohd	(19xx -19xx)	NA	NA
31	Mr. M. A. B. Khan	(19xx -19xx)	NA	NA
32	Mr. J.P. Gupta	(19xx -19xx)	NA	NA
33	Dr. Yogendra Kumar	(19xx -19xx)	NA	NA
34	Dr. A.K. Ansari	(19xx -19xx)	NA	NA
35	Dr. Raziuddin Siddiqui	(19xx -19xx)	NA	NA
36	Dr. Sisir Gupta	(1950-1954)	NA	NA
37	Dr. Rohtash Kunwar Tyagi	(1954-1956)	NA	NA
38	Dr. Asoke Nath Mitra	(1955-1960)	NA	NA
39	Prof. Putcha Venkateswarlu	(1954-1961)	NA	NA
40	Dr. Harnam Singh Hans	(1958-1963)	NA	NA
41	Dr. G. N. Rao	(1963-1965)	NA	NA
42	Dr. Ayodhya Prasad Sharma	(1958-1966)	NA	NA
43	Dr. M. Yasin	(1964-1967)	NA	NA
44	Prof. Mohammad Shafi	(19xx-1991)	(1985-1988)	(1967-1970)
45	Prof. Rais Ahmad	(1964-1974)	(1964-1974)	(1972-1974)
46	Dr. Zahid Hussain Zaidi	(1968-1971)	NA	NA
47	Dr. D.C. Sarkar	(1951-1971)	NA	NA
48	Dr. PucadyilIttoop John	(1969-1972)	NA	NA
49	Dr. S.G. Ganguli	(1964-1974)	NA	NA
50	Dr. A. K. Jalaluddin	(1968-1977)	NA	NA
51	Dr. S. Fazal Mohammad	(1950-1983)	NA	NA
52	Prof. M. L. Sehgal	(1963-1985)	(1984-1985)	NA
53	Prof. S. M. Razaullah Ansari	(1969-1993)	NA	NA
54	Prof. A.V. Jafri	(1959-1993)	NA	NA
55	Prof. R.S. Yadav	(1960-1993)	NA	NA
56	Prof. B.N. Khanna	(1964-1993)	(1991-1993)	NA
57	Dr. M. Z. Ahsan	(1965-1993)	NA	NA
58	Dr. M.K. Sharma	(1961-1994)	NA	NA
59	Prof. M. Zillur Rahman Khan	(1954-1995)	(1974-1984)	(1977-979)
60	Prof. M. S. Swami	(1969-1984)	(1984-1984)	(1979-1981)

61	Prof. Mirza Sayeed uz Zafar Chaghtai	(1969-1997)	(1993-1996)	(1996-1997)
62	Prof. Rana Janardan Singh	(1968-1997)	NA	NA
63	Prof. Israr Ahmad	(1961-1998)	(1988-1991)	NA
64	Dr. M. Akhtar Alvi	(1991-2000)	NA	NA
65	Prof. Jawad Hasan Naqvi	(1963-2001)	(1996-1997)	(1999-2001)
66	Prof. Raghubar Dayal	(1968-2001)	NA	NA
67	Dr. Arshad Ahmad	(1966-2002)	NA	NA
68	Prof. Ashok Kumar Chaubey	(1965-2004)	(2003-2004)	NA
69	Prof. Syed Mohammad Abul Hashim Rizvi	(1965-2004)	NA	NA
70	Dr. P. K. Verma	(1966-2004)	NA	NA
71	Prof. Yogendra Kumar	(1970-2004)	NA	NA
72	Dr. Farhan Mujeeb	(1971-2004)	NA	NA
73	Dr. T.S. Gill	(1973-2005)	NA	NA
74	Dr. Habibul Haq Ansari	(1998-2005)	NA	NA
75	Prof. Rajeshwari Prasad	(1969-2006)	(1997-1999) (2002-2003)	(2005-2006)
76	Prof. Jagdish Prasad Srivastava	(1973-2006)	NA	NA
77	Prof. Mohammed Irfan	(1976-2010)	(2004-2007)	NA
78	Dr. Abu Shaz	(20xx -20xx)	NA	NA
79	Prof. Mohammad Zafar	(1970-2011)	(2007-2010)	NA
80	Dr. Q. N. Usmani	(19xx -19xx)	NA	NA
81	Prof. K. A. Mohammed	(1977-2011)	NA	NA
82	Prof. Sri Krishna Singh	(1979-2011)	(1999-2002)	(2003-2005)
83	Dr. Ms. Fauzia Mujeeb (WC)	(1971-2012)	NA	NA
84	Mr. Badre Alam	(1978-2012)	NA	NA
85	Prof. M. Shafikuddin Mollah	(1999-2012)	NA	NA
86	Mr. Subodh Kumar Gupta	(1972-2013)	NA	NA
87	Dr. Ms. Sabra Khatoon (WC)	(1987-2013)	NA	NA
88	Dr. Sanjeev Kumar Verma	(20xx -20xx)	NA	NA
89	Dr. Rashid Hasan	(1975-2014)	NA	NA
90	Prof. Zafar Ali Khan	(1975-2014)	NA	NA
91	Dr. Mushtaq Ahmed	(1982-2014)	NA	NA
92	Prof. Wasi Haider	(1970-2014)	(2010-2013)	NA
93	Mrs. Nikhat Bano (WC)	(1977-2015)	NA	NA
94	Prof. Rahimullah Khan	(1977-2015)	(2013-2015)	(2015-2015)
95	Prof. Abdul Qayum	(1978-2015)	NA	NA
96	Dr. Abdur Rahim Khan	(1979-2015)	NA	NA
97	Prof. Shafiq Ahmad	(1983-2016)	NA	NA
98	Dr. Syed Rafi Ahmad	(2014-2016)	NA	NA
99	Prof. Mohammad Shoeb	(1984-2017)	NA	NA
100	Prof. Mohammad Afzal Ansari	(1984-2017)	(2015-2017)	NA
101	Dr. Iqbal Ahmad Ansari	(1991-2019)	NA	NA
102	Prof. Tauheed Ahmad	(1995-2019)	(2017-2019)	NA
103	Prof. Badruddin	(1995-2019)	NA	NA

Statistical Summary (2012–2024)
During this period, a total of one hundred and three teachers retired/quitted from the department. Among them, twenty five had the privilege of serving as Chairman of the department, while ten held the esteemed position of Dean, Faculty of Science.

Reference
100 years of the Faculty of Science. Aligarh Muslim University (1920-2020) published by AMU, Aligarh, 2021.

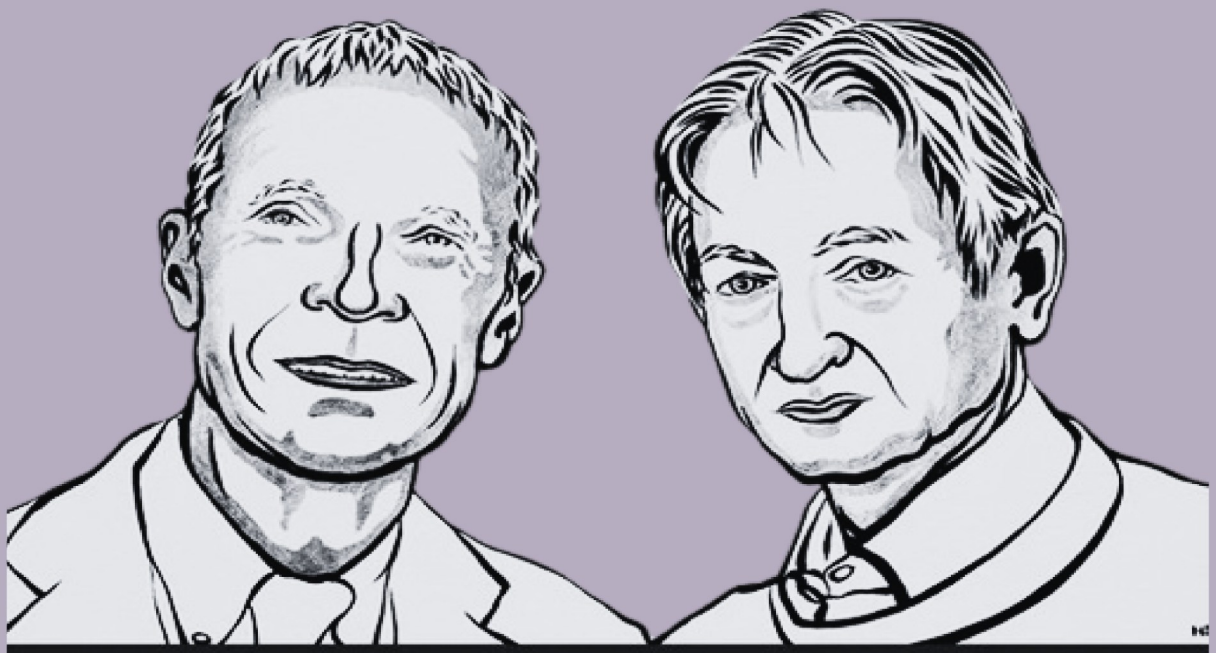
John J. Hopfield
Geoffrey E. Hinton
"for foundational discoveries and inventions
that enable machine learning
with artificial neural networks"